UNIVERSITY OF CALIFORNIA, SAN DIEGO

Finite Length and Trapped-Particle Diocotron Modes

A dissertation submitted in partial satisfaction of the

requirements for the degree Doctor of Philosophy

in Physics

by

Terance Joseph Hilsabeck

Committee in charge:

Thomas M. O'Neil, Chairman
Daniel H. E. Dubin
C. Fred Driscoll
Kevin Quest
William R. Young

2003

The dissertation of Terance Joseph Hilsabeck is approved, and it is acceptable in quality and form for publication on microfilm:

Chairman

University of California, San Diego

2003

Table of Contents

List of Figures

Acknowledgements

I would like to thank my adviser Professor Tom O'Neil for teaching me theoretical plasma physics and providing many hours of stimulating discussions regarding my research. I have learned a great deal from Professor O'Neil, but perhaps the most important lesson is the importance of stripping away unnecessary complexity and searching out the underlying processes that govern the dynamics of a physical system. I am also grateful to Professors Fred Driscoll and Dan Dubin for their poignant insight concerning the results of my research and helpful suggestions for further investigations. Of course, I am grateful to all the members of my committee for their participation.

Much of the work contained in this thesis is an attempt to provide a theoretical understanding of phenomena observed in experiments on confined nonneutral plasmas conducted at UCSD. I have appreciated greatly my collaboration with Dr. Andrey Kabantsev and the wealth of results and discoveries that he has produced in the laboratory. I am also grateful to Dr. David Schecter, Dr. Eric Hollmann, Dr. Francois Anderegg, Dr. Dezhe Jin, Dr. Jason Kriesel, Dr. James Danielson, Jonathan Yu, Nobuyashi Shiga, Stanislas Kuzmin, Kevin Rigg, Shane Walker and Eric Bass for stimulating discussions. Jo Ann Christina has been very helpful in the preparation of technical manuscripts.

I am deeply indebted to my parents Dan and Michelle for developing my interest in learning from an early age and encouraging my curiosity about the world

I live in. I am also grateful to my wife Tracy who has provided many years of love and support throughout my graduate studies.

Chapter 2 of this thesis has been published in Physics of Plasmas: ”Finite Length Diocotron Modes”, T. J. Hilsabeck and T. M. O’Neil, **8**, 407-422 (2001). Chapter 3 has been submitted to Physics of Plasmas: ”Trapped-Particle Diocotron Modes”, T. J. Hilsabeck and T. M. O’Neil. T. J. Hilsabeck was the primary investigator and author of these papers.

This research was supported financially by the National Science Foundation (PHY-9876999), the Office of Naval Research (N00014-96-1-0239) and the ARCS Foundation.

Vita, Publications and Fields of Study

Vita

08 December 1970	Born, Iowa Falls, Iowa
1993	B.A., University of California, Berkeley
1997	M.S., San Diego State University, San Diego
2003	Ph.D., University of California, San Diego

Publications

1. T. J. Hilsabeck and T. M. O'Neil, "Finite Length Diocotron Modes," *Physics of Plasmas* **8**, 407 (2001)

2. A.A. Kabantsev, C.F. Driscoll, T.J. Hilsabeck, T.M. O'Neil, and J.H. Yu, "Trapped-Particle Asymmetry Modes in Single-Species Plasmas," Phys. Rev. Lett. 87, 225002 (2001).

Fields of Study

Major Field: Physics

Studies in Plasma Physics
Professor Vitali Shapiro

Studies in Mechanics
Professor Benjamin Grinstein

Studies in Electromagnetism
Professor Aneesh Manohar

Studies in Quantum Mechanics
Professors George Fuller and Benjamin Grinstein

Studies in Statistical Mechanics
Professor Daniel Dubin

Studies in Group Theory
Professor Aneesh Manohar

Studies in Mathematical Physics
Professor Aneesh Manohar

Abstract of the Dissertation

Finite Length and Trapped-Particle Diocotron Modes

by

Terance Joseph Hilsabeck
Doctor of Philosophy in Physics
University of California, San Diego, 2003
Professor Thomas M. O'Neil, Chairman

Diocotron modes are discussed for a finite length nonneutral plasma column under the assumption of bounce averaged $\mathbf{E} \times \mathbf{B}$ drift dynamics and small Debye length. In this regime, Debye shielding forces the mode potential to be constant along field lines within the plasma. One can think of the plasma as a collection of magnetic field aligned rods that undergo $\mathbf{E} \times \mathbf{B}$ drift across the field and adjust their length so as to maintain the condition $\partial\delta\phi/\partial z = 0$ inside the plasma. Using a Green function to relate the perturbed charge density and the perturbed potential, imposing the constraint $\partial\delta\phi/\partial z = 0$, and discretizing yields a matrix eigenvalue problem. The solutions include the full continuum and discrete stable and unstable diocotron modes. Finite column length introduces a new set of discrete diocotron-like modes. Also, finite column length makes possible the exponential growth of $\ell = 1$ diocotron modes, long observed in experiments. The model is extended to include the dependence of a particle's bounce averaged rotation frequency on its axial energy. For certain distributions of axial energies, this dependence can substantially affect the instability.

Recent experiments have characterized trapped-particle modes on a nonneutral plasma column[17]. Theoretical predictions for the mode frequency, damping rate, and eigenmode structure are developed here. The modes are excited on a nonneutral plasma column in which classes of trapped and passing particles have been created by the application of a potential barrier. The barrier is created by applying a voltage to an azimuthally symmetric section of the wall near the axial mid-point of the column. Low energy particles near the edge of the column are trapped in one end or the other, while high energy particles near the center of the column transit the entire length. The modes have azimuthal variation $\ell = 1, 2, ...$ and odd z-symmetry. The trapped particles on either side of the barrier execute $\mathbf{E} \times \mathbf{B}$ drift oscillations producing density perturbations that are 180° out of phase with each other, while passing particles run back and forth along the field lines attempting to Debye shield the perturbed charge density. The mode is damped by collisional scattering across the separatrix between trapped and passing particles. The damping rate is calculated using a boundary layer analysis of the Fokker-Planck equation. It is also shown that the damping is associated with radial transport of plasma particles.

Chapter 1

Introduction

1.1 Background

Surprisingly, the story of diocotron modes begins in the 19^{th} century with the work of early fluid dynamicists. In 2-dimensions (2D), the equations describing the evolution of $\mathbf{E} \times \mathbf{B}$ drift oscillations on a low density nonneutral plasma column are isomorphic to the Euler equations that govern the dynamics of inviscid, incompressible fluids[21]. In 1868, H. L. F. von Helmholtz observed that flow past a sharp geometrical edge produces a disturbance in a fluid. More generally, an instability develops at the interface between two stratified fluid layers that are in relative motion along the direction of the interface. A formal solution to this problem for the case of incompressible, inviscid fluids was constructed by Lord Kelvin in 1871 and the phenomenon is now called the Kelvin-Helmholtz instability.

In 1880, the motion of a fluid with a shear velocity profile was analyzed by Lord Rayleigh [29]. In his solution, Rayleigh approximated the velocity profile by piecewise linear segments and obtained an inflection-point stability theorem. Lord Kelvin noted that for smoothly varying velocity profiles, Rayleigh's equation was infinite near a wave-fluid resonance. By examining velocity streamlines, Kelvin noticed that fluid elements are trapped in "cat's eye" patterns near the resonance[19]. In 1960, K. M. Case discovered that the complete set of normal modes for this system includes a continuous spectrum of modes[2].

During the 1940's, the development of RADAR technology required sources of high power microwave radiation. Crossed-field tubes in which electron beams are propagated through mutually perpendicular DC electric and magnetic fields were designed to satisfy this need. In one such device, known as the electron wave magnetron, a "slipping stream" of electrons was found to develop a growing wave due to space-charge forces[23]. "Slipping stream" refers to the sheared $\mathbf{E} \times \mathbf{B}$ drift velocity profile of the electron beam. This phenomenon was later labeled the "Diocotron Effect" by French researchers[11]. The word "diocotron" is derived from the Greek verb "$\delta\iota\omega\kappa\omega$" which means "I chase," and was chosen as a reminder of the existence of layers in which electrons run next to each other at different velocities. In 1955, H. F. Webster conducted an experiment in which he observed an annular ring of electrons break up into a discrete number of vortex-like current bundles[37]. In some devices, it was concluded that these growing space-charge waves were responsible for the generation of deleterious effects such as spurious signals and noise[10].

In 1965, R. H. Levy made the connection between the fluid dynamics and electron beam physics explicit when he published stability conditions on a uniform density annular electron beam in the low density limit[21]. Levy obtained an exact analogy between the plasma and fluid problems in 2D. In the analogy, the electron density, drift velocity and potential correspond to the fluid vorticity, velocity, and the stream function, respectively. Several years later he found that for the special case of azimuthal wavenumber $\ell = 1$, there exists a universal stable mode with azimuthal phase velocity equal to the $\mathbf{E} \times \mathbf{B}$ drift frequency at the wall[22]. The mode is universal in the sense that its potential perturbation and phase velocity are independent of the equilibrium density profile. Briggs, Daugherty and Levy recognized an analogy between the resonant interaction of a diocotron mode with the background plasma rotation and the Landau damping of plasma waves[1]. Their analysis included a dispersion relation for diocotron modes on a uniform density column, resistive wall destabilization of the negative energy waves and spatial Landau damping.

The term "diocotron mode" now generally refers to an essentially 2D $\mathbf{E}\times\mathbf{B}$ drift oscillation of a magnetically confined nonneutral plasma column. Diocotron modes are useful in non-destructive diagnostic measurements. Experimentalists launch and detect diocotron modes in order to obtain information about the number and distribution of charges in the trap. 2D theory is useful for determining this type of information. However, there are additional phenomena connected with diocotron modes caused by axial structure in the system. Two such phenomena are discussed here.

1.2 Finite Length Diocotron Modes

According to standard 2D linear analysis, diocotron modes are stable for azimuthal mode number $\ell = 1$. However, C. F. Driscoll observed exponentially growing $\ell = 1$ modes on a hollow columns confined in a Malmberg-Penning trap[5]. The unstable mode exits simultaneously with the stable mode correctly predicted by theory. Driscoll found that the instability produces substantial cross-field transport and ultimately leads to a stable profile. In 1990, R. A. Smith and M. N. Rosenbluth discovered by initial-value treatment that algebraically growing $\ell = 1$ perturbations appear whenever the equilibrium rotation frequency profile is nonmonotonic[35].

Smith later found that axial variations in the radial electric field introduce a quadratic term into the expression for the rotation frequency, and this can lead to exponential instability[34]. In fact, adding any extra terms (e.g., terms due to finite gyroradius or viscosity) to the continuity equation destroys the special properties of the fundamental ($\ell = 1$) mode and can lead to exponentially growing modes. However, the growth rates predicted by such terms are too small to explain the experimental results. In 1999 Finn, del-Castillo-Negrete and Barnes introduced a model that included a quadratic radial dependence of the column length and argued that radial excursions of line charge during the perturbed drift motion creates a compressional effect[8]. This model also predicted exponential instability for $\ell = 1$ and the computed growth rates were nearer those measured in the experiments.

In Chapter 2, a model is developed to describe linear diocotron modes on a finite length column. In this model, it is assumed that the Debye length is negligibly small and that the axial bounce frequency of particles is sufficiently high that the plasma may be considered as a collection of magnetic field aligned charged rods. Therefore, a reduced description characterizes the plasma column using two axially independent functions: the z-integrated density $N(r, \theta, t)$ and the column length $L(r, \theta, t)$. The equilibrium length of the column is obtained by recognizing that Debye shielding forces the axial electric field at the plasma boundary to vanish. Linear eigenmodes are found by solving the drift-Poisson system of equations subject to the constraint that the axial electric field due to the perturbation must also vanish at the plasma boundary. This constraint determines the amount by which the charged rods change in length as they $\mathbf{E} \times \mathbf{B}$ drift radially in the perturbed potential.

Because the theory presented here admits a plasma of arbitrary shape, it is possible to obtain the mode frequencies for small spheroidal plamsas. The calculated frequencies are in excellent agreement with the corresponding cold fluid mode frequencies given by the analytic dispersion relation of Dubin[6]. Additionally, the finite length theory predicts that a number of new modes exist for plasmas with very low shear in the rotation profile. These modes were predicted by Finn et. al. and are analogous to Rossby waves in geophysical fluid dynamics. The finite length description also predicts exponentially growing modes on hollow columns. In general, the growth rates for the $\ell = 1$ modes are in agreement with the results of Finn et. al. However, the calculated growth rates are generally several times less than measurements and close quantitative agreement requires additional considerations.

To investigate one such consideration, the model is extended to include a kinetic correction due to the dependence of the bounce averaged rotation frequency on the axial particle energy. Although this correction is usually small compared to the rotation frequency, it can become important near the wave-fluid resonance. In a finite temperature plasma, there is a range of axial particle velocities on each field. Therefore, the wave-fluid resonance associated with the unstable mode has a finite radial width. This feature causes the growth rates to depend on the distribution of particle velocities. In the experiments, hollow columns are created from monotonic columns by lowering the confining potential and allowing high axial energy particles to escape. The growth rates calculated for the resulting non-Maxwellian distribution of particle velocities is higher than for the Maxwellian case. This increase in the growth rate improves the correspondence between calculation and measurement. Subsequently, this conclusion was confirmed by particle-in-cell simulations[24].

1.3 Trapped-Particle Diocotron Modes

Recent experiments have discovered of a new type of diocotron mode[17]. This mode was observed on columns that are partially divided by the application of an axisymmetric ”squeeze” voltage to a short cylinder near the axial midpoint of the trap. The resulting potential barrier inside the plasma traps particles with low axial energy in the column ends, whereas high energy particles travel the entire length of the column. From the experimental results, the new oscillation was best described as two diocotron-like modes, being 180° out of phase on either side of the squeeze barrier. The experiments further revealed that the mode is damped under all conditions of its observation.

In Chapter 3, a theoretical model for this ”trapped-particle” diocotron mode is presented. Since the mode potential has an odd z-symmetry, the bounce-averaged mode potential vanishes for untrapped orbits, so the passing particles do not experience a perturbation in their $\mathbf{E} \times \mathbf{B}$ drift motion. Therefore, the passing particles remain on their original field lines, but move axially in adiabatic response to the mode potential. However, the trapped particles are unaware of the mode potential opposite the squeeze region (except through the coupling provided by the passing particles), so they develop $\mathbf{E} \times \mathbf{B}$ drift perturbations. A simple theory encompassing these dynamics yields a mode frequency that varies from the rotation frequency at the column edge to the usual diocotron frequency, as the squeeze voltage is varied from zero to the plasma potential. This behavior closely matches the experimental observations.

The trapped-particle diocotron mode is a directly analogous to drift waves in neutral plasmas. The basic requirement for the existence of the mode is the presence of two particle classes: slow moving particles that are isolated from the global mode structure, and fast particles that average over the global structure. In drift wave oscillations, this distinction is provided by the much larger inertia of the ions. The electric field in a drift wave has a small component along the magnetic field line. This parallel electric field is large enough to move electrons, but ions are limited to cross-field drift motion by their large mass.

In another type of neutral drift wave called trapped-ion and trapped-electron modes, magnetic trapping creates the two separate classes of particles. In toroidal magnetic confinement devices, the non-uniform magnetic field produces a mirror effect and prevents particles with low axial velocity from making complete toroidal orbits. If the effective collision time for trapped particles is longer than their orbital period, the trapping effect is important and new modes are introduced into the system. These trapped-particle modes have been studied at great length and are of concern in high temperature devices[36].

The theoretical model used to describe the trapped-particle diocotron mode reduces much of the complexity of the 3D system. The modes are treated with an essentially 2D analysis that excludes the axial variations of potential and density near the ends of the column and in the squeeze region. However, the model correctly treats the dynamics of trapped and passing particles, which is the essential effect in the oscillation. The axisymmetric equilibrium density and potential are obtained through a combination of experimental measurements and a solution of the Poisson-Boltzmann equation. The solution provides the local density profile and radially dependent trapping fraction that are needed to solve the linear eigenmode equation.

The damping mechanism for the trapped-particle diocotron mode is also analyzed. The mode is damped by collisions between the particles near the phase-space separatrix. Although the collision frequency is small compared to the other dynamical frequencies in the experiment, velocity space diffusion is significant near the separatrix between trapped and passing particles. If the plasma were entirely collisionless, the perturbed distribution of guiding centers would be discontinuous at the separatrix velocity. Under such circumstances, even weak collisions are highly effective in smoothing out the discontinuity; and thus the collisions create an appreciable particle flux through the separatrix. This scattering process causes the wave to be damped and particles to be transported radially. The calculation of the damping rate presented in Chapter 3 employs a boundary layer analysis similar to that previously used by Rosenbluth, Ross and Kostamarov to investigate dissipative trapped-ion instabilities[31].

Resonant Landau damping may also occur in these modes, but it appears to be weak compared to collisional damping in the regimes considered here. Because the trapped-particle diocotron mode has odd symmetry across the squeeze region, there is an axial electric field present there. As particles enter the squeeze region, the wave influences their parallel motion and the opportunity for resonant exchange of energy exists. In the high bounce frequency limit, however, this effect is much weaker than collisional scattering. Resonant particles are deeply trapped and do not penetrate a significant distance into the squeeze and end regions where the axial electric field is appreciable. Particles very near to the separatrix can also bounce resonantly with the wave. However, these particles are so near to the separatrix that collisions scatter the particles out of resonance before energy can be exchanged. Therefore, the collisional damping mechanism dominates in the high bounce frequency regime. However, Landau damping may become important for plasmas in which the bounce and rotation frequencies are comparable.

The theory predicts the existence of additional trapped-particle diocotron modes that have not yet been observed in the experiments. The new modes have azimuthal phase velocities above the peak rotation frequency in the column. These high frequency modes are "self-shielded", i.e. only weak mode potentials exist in the vacuum region outside the plasma column. The modes are indexed by a radial wavenumber, n_r, and the mode frequencies asymptote to the peak rotation frequency as n_r increases. These high frequency modes have positive energy, and their damping due to velocity diffusion is associated with a net radial transport inward.

The damping of the trapped-particle diocotron mode and the associated radial transport mechanism appears to have strong implications for asymmetry-induced transport in nonneutral plasmas. Due to construction errors, Malmberg-Penning traps always have weak electric or magnetic asymmetries. Therefore, stray potentials exist that cause particle trapping and perturbed drift orbits throughout the device. Velocity space diffusion across the trapping separatrices provides a pervasive mechanism whereby external field asymmetries can couple into the plasma and produce radial transport. Experiments have shown that the radial transport due to applied, static field asymmetries is directly proportional to the damping rate of the trapped-particle diocotron mode[15]. This result is in agreement with a simple theoretical picture of the process. However, the observed experimental scaling with plasma parameters does not agree with the theory. This discrepancy is the subject of ongoing research and discussion.

Chapter 2

Finite Length Diocotron Modes

2.1 Abstract

Diocotron modes are discussed for a finite length nonneutral plasma column under the assumption of bounce averaged $\mathbf{E} \times \mathbf{B}$ drift dynamics and small Debye length. In this regime, which is common to experiments, Debye shielding forces the mode potential to be constant along field lines within the plasma (*i.e.*, $\partial\delta\phi/\partial z = 0$). One can think of the plasma as a collection of magnetic field aligned rods that undergo $\mathbf{E} \times \mathbf{B}$ drift across the field and adjust their length so as to maintain the condition $\partial\delta\phi/\partial z = 0$ inside the plasma. Using the Green function (for a region bounded by a conducting cylinder) to relate the perturbed charge density and the perturbed potential, imposing the constraint $\partial\delta\phi/\partial z = 0$, and discretizing yields a matrix eigenvalue problem. The mode eigenvector $\delta N_{\ell,\omega}(r_j) \equiv \int dz\, \delta n_{\ell,\omega}(r_j, z)$ is the ℓ^{th} azimuthal Fourier component of the z-integrated density perturbation, and the frequency ω is the eigenvalue. The solutions include the full continuum and discrete stable and unstable diocotron modes. Finite column length introduces a new set of discrete diocotron-like modes. Also, finite column length makes possible the exponential growth of $\ell = 1$ diocotron modes, long observed in experiments. The paper focuses on these two problems. To approach quantitative agreement

with experiment for the $\ell = 1$ instabilities, the model is extended to include the dependence of a particle's bounce averaged rotation frequency on its axial energy. For certain distributions of axial energies, this dependence can substantially affect the instability.

2.2 Introduction

This paper provides a description of diocotron and continuum modes for a finite length nonneutral plasma column[3]. The plasma is confined in a Malmberg-Penning trap with the configuration shown in Fig. 2.1. The wall is a conducting cylinder of radius R that is divided axially into three sections, with the central section grounded and the two end sections held at a positive potential V (to confine a plasma of positive charges). The central section has an axial length of $2Z$ and the end sections extend to infinity. The plasma resides in the region of the central grounded section, with axial confinement provided by electrostatic fields and radial confinement by a uniform axial magnetic field.

Because the plasma is nonneutral, there is a substantial radial electric field, and the plasma experiences an $\mathbf{E} \times \mathbf{B}$ drift rotation, $\omega_E = -(c/Br)(\partial\phi_0/\partial r)$. Here, $\phi_0\,(z,r)$ is the equilibrium plasma potential, $\mathbf{B} = -\hat{\mathbf{z}}B$ is the magnetic field, and (z,θ,r) is a cylindrical coordinate system with the z-axis coincident with the axis of the trap. For a plasma of positive charges, it is convenient to choose the magnetic field in the $-\hat{\mathbf{z}}$ direction; this makes the rotation frequency (and the mode frequencies) positive. The frequencies are the same for a plasma of negative charges if the sign of the confinement fields is reversed (*i.e.*, $\mathbf{B} \to -\mathbf{B}$ and $V \to -V$).

The modes of interest are characterized by frequencies that are comparable to the rotation frequency (*i.e.*, $\omega \sim \omega_E$). The other important dynamical frequencies are the cyclotron frequency, Ω_c, and the characteristic axial bounce frequency for a particle, ω_b. In accord with experiment[5, 18], we assume that the frequencies are ordered as $\Omega_c \gg \omega_b \gg \omega_E \sim \omega$. The mode evolution can then be treated with bounce average $\mathbf{E} \times \mathbf{B}$ drift dynamics.

Also in accord with experiment, we assume that the Debye length is small compared to the plasma dimensions (*i.e.*, $\lambda_D \ll r_p, l_p$). At first glance, the two inequalities $\omega_b \gg \omega_E$ and $\lambda_D \ll l_p$ look contradictory, but they both can be satisfied provided $\omega_p/\Omega_c \ll \lambda_D/l_p$, where ω_p is the plasma frequency. Here, we have used $\omega_b \sim \bar{v}/l_p$, $\omega_E \sim \omega_p^2/\Omega_c$, and $\lambda_D = \bar{v}/\omega_p$, where $\bar{v}$ is the thermal velocity. The frequency ordering and the smallness of the Debye length justify a reduced description of the plasma. In this Zero Debye Length Reduced Description, the plasma cannot tolerate (shields out) any electric field ($\partial\phi/\partial z$) along the magnetic field. The plasma density, $n\,(z, \theta, r, t)$, is constant along z within the plasma and drops abruptly to zero at the plasma ends (on the scale $\lambda_D \to 0$). Along each field line, the plasma is characterized by a well-defined length $2L\,(\theta, r, t)$. For convenience, we use $L\,(\theta, r, t)$ for the half-length.

The plasma can be thought of as a collection of magnetic field aligned rods that move across the field through $\mathbf{E} \times \mathbf{B}$ drift motion and adjust their length so that $\partial\phi/\partial z$ vanishes everywhere inside the plasma. We will see that this constraint is satisfied if $\partial\phi/\partial z$ vanishes on the plasma surface [*i.e.*, for $|z| = L\,(\theta, r, t)$].

With $L\,(\theta, r, t)$ determined in this way, the plasma state is specified by the two-dimensional z-integrated density distribution

$$N(\theta, r, t) = \int_{-\infty}^{+\infty} dz\, n\,(z, \theta, r, t) = 2\, n\,(\theta, r, t)\, L\,(\theta, r, t)\,, \tag{2.1}$$

where $n\,(\theta, r, t)$ is the particle density inside the plasma. The electric potential $\phi\,(z, \theta, r, t)$ is expressed as a functional of $N\,(\theta, r, t)$ and $L\,(\theta, r, t)$ through an integral over a Green function for the trap geometry. The advantage of the reduced description is that it captures the three-dimensional nature of modes on a finite length plasma, while using a 2-D distribution to describe the plasma state.

To discuss the modes, this distribution is written as $N(\theta, r, t) = N_0(r) + \delta N_{\ell,\omega}(r)\exp(i\ell\theta - i\omega t)$, where the first term describes the equilibrium and the second describes a mode. Likewise, $L(\theta, r, t)$ is written as the sum $L_0(r) + \delta L_{\ell,\omega}(r)\exp(i\ell\theta - i\omega t)$, and the equations are linearized in $\delta N_{\ell,\omega}$ and $\delta L_{\ell,\omega}$. The analysis is implemented numerically, with functions evaluated at a set of discrete radial points $\{r_j\}$. The mode eigenvector $\{\delta N_{\ell,\omega}(r_j)\}$ is determined as the solution to a matrix eigenvalue problem, where the frequency ω is the eigenvalue. In the usual manner, eigenvectors for different eigenvalues are orthogonal, and a general linear solution can be written as a superposition of modes.

The set of modes includes what in an analytic theory would be called continuum modes as well as discrete modes. In this sense, the work extends recent work on 2-D modes for an infinitely long column[33].

We focus on two aspects of the modes that are due to finite column length. The first is the existence of a new set of discrete diocotron-like modes that appear in plasmas with very low shear in the rotational flow. The prototype of such a plasma is the uniform density plasma, for which the flow is a shear-free rigid rotation. It is well known that an infinitely long column of uniform density supports only one discrete diocotron-like mode for each azimuthal wave number[3]. In contrast, a uniform density column of finite length supports many additional discrete diocotron-like modes, with azimuthal phase velocities that are shifted from the rotation frequency by a small amount that depends on the plasma end shape. The shift tends to zero as the number of nodes in the radial eigenmode, $\delta N_{\ell,\omega}$, becomes large. A density variation in the equilibrium introduces shear in the rotational flow, and the new modes are absorbed into the continuum, as they become resonant with the fluid at some critical radius.

These new modes were predicted by Finn *et al.*[8], who drew an analogy between the modes and Rossby waves in the quasigeostrophic β-plane approximation [32]. For analytic convenience, these authors approximated the plasma length by a quadratic function, $L_0(r) \simeq L_0(1 - \kappa r^2)$, where κ is a measure of the end shape curvature at $r = 0$. Neglecting any perturbation in the plasma length, they then obtained a simple dispersion relation for the modes that predicts a κ dependent shift in the azimuthal phase velocity (relative to the plasma rotation). The predicted frequencies are in qualitative agreement with our numerical results when the end shape is well-approximated by a quadratic function, but can differ significantly in other cases.

For example, the end shape can increase with radius on-axis (corresponding to negative curvature) and decrease with radius off-axis (corresponding to positive curvature). In this case, we find some modes that have a positive phase velocity shift and others that have a negative shift, whereas the dispersion relation predicts a single sign for the shift. The modes with negative shift "live" in a radial region where the equilibrium length is a decreasing function of radius, and the modes with positive shift "live" in the region where the length is increasing. The significance of the modes with positive shift is that they are more able to withstand small shear in the rotational flow. They rotate faster that the plasma.

Next we focus on a particular instability that exists because of finite column length. In general, a necessary condition for diocotron-like instabilities in an infinitely long column is that the column density, $n_0(r)$, be non-monotonic in r[3]. For example, a hollow column satisfies this criterion. Likewise, a necessary condition for such instabilities in a finite length column is that $N_0(r)$ be non-monotonic[8, 27]. Detailed stability analyses for an infinitely long, hollow column have been carried out previously[1, 3]. The modes for azimuthal mode number $\ell = 1$ are special in that analytic solutions are possible for any density profile $n_0(r)$. Surprisingly, the analysis predicts that the $\ell = 1$ modes are neutrally stable, that is, the imaginary part of the mode frequency ω is zero even for hollow columns[22, 4]. An initial value solution of the infinite length, $\ell = 1$ diocotron instability yields algebraic growth[35]. However, exponential growth of $\ell = 1$ modes is observed experimentally for hollow columns of finite length.

Smith[34] predicted exponential growth when the plasma rotation frequency differs from that given by Gauss' law for an infinite column. He included a small shift in the rotation frequency arguing heuristically that it was due to the end confinement fields. Finn *et al.*[8] also considered this problem and obtained exponential growth. Again their analysis approximated the plasma length by a quadratic function. A mode induced perturbation in the plasma length was included for this analysis, but was implemented by a clever technique chosen for analytic convenience rather than experimental fidelity.

In contrast, our model accepts an arbitrary plasma shape and our axial boundary conditions are realistic. Also, our model incorporates the perturbation of the plasma length self-consistently using a Green function. Nevertheless, the two models find similar growth rates for plasmas with significant curvature.

Although consideration of finite length effects predicts the existence of an $\ell = 1$ instability, good quantitative agreement with experiments has not been achieved. In general, the growth rates due to finite length effects alone are several times smaller than the experiments measure. Also, the calculated real frequencies are very near the maximum rotation frequency of the plasma, while the experiment may observe a frequency 25% lower.

In Sec. 2.8, we shall see that the incorporation of kinetic effects and the details of how the hollow columns are prepared have a significant impact on the instability. The important kinetic effect is the dependence of a particle's bounce averaged rotation frequency on its axial energy. The faster a particle strikes the end of the column, the larger radial electric force it experiences. Thus, a spread in axial particle energies produces a broadening of the unstable mode's resonance with the plasma rotation. In order to create the hollow profile columns, the axial confining potential is lowered and the highest energy particles escape. This process essentially cools the column near the trap axis and can significantly change the growth rate and frequency of the instability.

2.3 Basic Equations

Because the cyclotron frequency is large and the cyclotron radius is small, the guiding center drift approximation can be used to follow the particle dynamics. Since the magnetic field is uniform, the guiding center drift Hamiltonian can be written as

$$H = \frac{p_z^2}{2m} + e\phi\left(z, \theta, p_\theta, t\right) \tag{2.2}$$

where the ordered pairs $(z, p_z = m\dot{z})$ and $(\theta, p_\theta = -eBr^2/2c)$ are canonically conjugate coordinates and momenta and ϕ is the electric potential.

Let $f = f\left(z, p_z, \theta, p_\theta, t\right)$ be the distribution of guiding centers. For convenience, we normalize f so that the total number of particles is given by

$$N = \frac{c}{eB}\int f dp_z dz d\theta dp_\theta = \int f dp_z d^3\mathbf{r}, \tag{2.3}$$

where $d^3\mathbf{r} = dz d\theta r dr$ is the configuration space volume element. The plasma density is then given by

$$n\left(z, \theta, r, t\right) = \int\limits_{-\infty}^{+\infty} dp_z f. \tag{2.4}$$

Also for convenience, we will denote the radial dependence of various quantities interchangeably as $g\left(r\right)$ and $g\left(p_\theta\right)$, although different functional dependencies are implied for g in the two cases.

On the time scale of the modes, f evolves according to the collisionless drift kinetic equation

$$\frac{\partial f}{\partial t}+\left[f,H\right]=0, \tag{2.5}$$

where $\left[f,H\right]$ is a Poisson bracket

$$\left[f,H\right]\equiv\sum_i\frac{\partial f}{\partial q_i}\frac{\partial H}{\partial p_i}-\frac{\partial f}{\partial p_i}\frac{\partial H}{\partial q_i}.$$

The electric potential, ϕ, must be determined self-consistently from the Poisson equation and the boundary conditions specified for ϕ on the conducting wall of the trap. The solution can be written formally as

$$\phi\left(z,\theta,r,t\right)=\phi_T\left(z,r\right)+e\int\limits_{-\infty}^{+\infty}dz'\int\limits_0^{2\pi}d\theta'\int\limits_0^R r'dr'G\left(z,\theta,r|z',\theta',r'\right)n\left(z',\theta',r',t\right), \tag{2.6}$$

where $\phi_T\left(z,r\right)$ is the trap potential and $G\left(z,\theta,r|z',\theta',r'\right)$ is a Green function that vanishes on the wall. Here, $\phi_T\left(z,r\right)$ satisfies the Laplace equation and matches the boundary conditions specified for ϕ on the wall. The second term (Green function term) satisfies the Poisson equation and vanishes on the wall, so the sum of the two provides the correct solution.

The Green function for the interior of an infinitely long, grounded, conducting cylinder, of radius R, is well known[14]

$$G\left(z,\theta,r|z',\theta',r'\right)=\frac{2}{R}\sum_{\ell=-\infty}^{+\infty}\sum_{n=1}^{\infty}\frac{e^{i\ell(\theta-\theta')}J_\ell\left(\frac{\chi_{\ell n}r}{R}\right)J_\ell\left(\frac{\chi_{\ell n}r'}{R}\right)}{\chi_{\ell n}J_{\ell+1}^2\left(\chi_{\ell n}\right)}e^{-\frac{\chi_{\ell n}}{R}(z_>-z_<)} \tag{2.7}$$

or equivalently

$$G = \frac{2}{\pi} \sum_{\ell=-\infty}^{+\infty} \int_0^{\infty} dk e^{i\ell(\theta-\theta')} cos\left[k\left(z-z'\right)\right] \times$$

$$\times \frac{I_\ell\left(kr_<\right)}{I_\ell\left(kR\right)}\left[I_\ell\left(kr_>\right)K_\ell\left(kR\right) - K_\ell\left(kr_>\right)I_\ell\left(kR\right)\right] \tag{2.8}$$

where $\chi_{\ell n}$ is the n^{th} zero of J_ℓ. Here $z_>$ $(z_<)$ is the greater (lesser) of z and z', and the same is true for the radial coordinate. In using the boundary condition for an infinitely long, grounded, conducting cylinder, we are assuming that the gaps in the electrodes are negligibly small. Furthermore, we assume the plasma column is always contained within the central conducting cylinder and that the length of the end cylinders is greater than their diameter. These conditions are experimentally typical. The sum over n in form (2.7) converges rapidly when $|z-z'|$ is large, and the k-integral in form (2.8) when $|r-r'|$ is large. For future reference, we note that G depends on (θ, θ') and (z, z') only through the combinations $\theta - \theta'$ and $z - z'$. This is a consequence of the rotational and translational invariance of the boundary conditions. In the following analysis, we will need the quantity

$$G_\ell\left(z, r|z', r'\right) = \int_0^{2\pi} \frac{d(\theta-\theta')}{2\pi} e^{-i\ell(\theta-\theta')} G. \tag{2.9}$$

Also, an expression for $\phi_T\left(z, r\right)$ is given by

$$\phi_T\left(z, r\right) = 2V \sum_{n=1}^{\infty} \frac{J_0\left(\frac{\chi_{0n} r}{R}\right)}{\chi_{0n} J_1\left(\chi_{0n}\right)} \cosh\left(\frac{\chi_{0n} z}{R}\right) e^{-\frac{\chi_{0n} Z}{R}}, \tag{2.10}$$

where V is the voltage on the end caps, R is the cylinder radius and Z is the central cylinder half-length. This expression is valid in the region $|z| < Z$.

2.4 Equilibria

We look for cylindrically symmetric equilibria setting $\phi = \phi_0\left(z, p_\theta\right)$ and correspondingly

$$H = H_0 = \frac{p_z^2}{2m} + e\phi_0\left(z, p_\theta\right). \tag{2.11}$$

Here, $\phi_0\left(z, p_\theta\right)$ is given by the sum of $\phi_T\left(z, r\right)$ and a cylindrically symmetrical space charge potential due to the Green function term in Eq. (2.6). Since $\left[p_\theta, H_0\right]$ vanishes, any distribution of the form $f = f_0\left(p_\theta, H_0\right)$ is an equilibrium.

To further specify the equilibrium, considerations beyond the collisionless drift kinetic equation must be taken into account. In the experiments of interest, modes are launched on both stable and unstable plasmas, and the preparation of the equilibrium is different in the two cases. For the stable case, the plasma is injected, held until collisions have established a local thermal equilibrium along each field line (a few collision times), and then modes are launched. The equilibrium for the stable modes is then the Boltzmann distribution

$$f_0\left(p_\theta, H_0\right) = \frac{N_0\left(p_\theta\right)\exp\left[-H_0/T\left(p_\theta\right)\right]}{\int\limits_{-\infty}^{+\infty} dz \int\limits_{-\infty}^{+\infty} dp_z \exp\left[-H_0\left(z, p_z, p_\theta\right)/T\left(p_\theta\right)\right]}, \tag{2.12}$$

where $T\left(p_\theta\right)$ is the local temperature along a field line at p_θ and $N_0\left(p_\theta\right) = \int_{-\infty}^{+\infty} dz\, n_0\left(z, p_\theta\right)$ is the z-integrated density along this field line. For given functions $N_0\left(p_\theta\right)$ and $T\left(p_\theta\right)$, Eq. (2.6) is an integral equation for the self-consistent potential, $\phi_0\left(z, r\right)$. A numerical solution for $\phi_0\left(z, r\right)$ can be obtained by iteration of Eq. (2.6), or of the Poisson equation itself. In turn, the solution for $\phi_0\left(z, r\right)$ completes the specification of the distribution $f_0\left(p_z, z, r\right)$ and the density $n_0\left(z, r\right)$.

In the limit where the Debye length is small, the solutions have a simple universal character. The charge density is arranged so that the component of the electric field along the magnetic field (*i.e.*, $-\partial\phi_0/\partial z$) is Debye shielded out in the interior of the plasma. The potential is nearly constant along z and then rises abruptly at the plasma ends over a length scale of a few Debye lengths. As implied by Eq. (2.12), the density $n_0\left(z,r\right)$ is nearly constant along z and then falls off sharply near the ends.

As a specific example for numerical solution, we choose the z-integrated density $N_0\left(r\right)$ shown in Fig. 2.2, the radially independent temperature $T = 1.0$ eV, the voltage on the end cylinders $V = 60$ Volts (the central cylinder is grounded), and the trap aspect ratio $R/Z = 5.086$. Figs. 2.3(a) and 2.3(b) show contour plots for $\phi_0\left(z,r\right)$ and $n_0\left(z,r\right)$, and the behavior described in the previous paragraph is clearly visible. Away from the plasma ends the contours run parallel to the magnetic field (parallel to the z-axis), but near the ends the contours cut across the field and are tightly bunched indicating a steep gradient. The gradient extends over a few Debye lengths.

For the case of unstable modes, the equilibrium is not of the Boltzmann form. In Sec. 2.8, we will discuss the preparation of the equilibrium for unstable modes in detail. Here, we need only the fact that the equilibrium distribution satisfies the inequality $\partial f_0/\partial H_0 \leq 0$. This is the feature that is required for Debye shielding.

Incidentally, if $f_0\left(p_\theta, H_0\right)$ were not monotonically decreasing in H_0, the plasma would be subject to velocity space instabilities that would develop much more rapidly than the modes of interest here. Thus, basing a theory of low frequency modes on the assumption $\partial f_0/\partial H_0 \leq 0$ is not really a loss of generality.

To understand the connection of this assumption to shielding, first define the density

$$n_0\left[p_\theta, e\phi_0\left(z,p_\theta\right)\right] = \int_{-\infty}^{+\infty} dp_z f_0\left[p_\theta, p_z^2/2m + e\phi_0\left(z,p_\theta\right)\right], \tag{2.13}$$

and note that $\partial n_0/\partial e\phi_0 = \int_{-\infty}^{+\infty} dp_z \partial f_0/\partial H_0$ is negative. The potential can be written as

$$\phi_0\left(z,r\right) = \phi_0\left(r\right) + \Delta\phi_0\left(z,r\right), \tag{2.14}$$

where the z-dependent part of $\Delta\phi_0\left(z,r\right)$ is presumed small in the plasma interior. This must be verified *a posteriori*. Taylor expanding the density with respect to $\Delta\phi_0$ and substituting into the Poisson equation yields the result

$$\left\{\frac{1}{r}\frac{\partial}{\partial r}r\frac{\partial\phi_0}{\partial r} + 4\pi e n_0\left[r,\phi_0\left(r\right)\right]\right\} + \left\{\nabla^2\Delta\phi_0 - \frac{1}{\lambda_D^2\left(r\right)}\Delta\phi_0\right\} = 0 \tag{2.15}$$

where we have defined the effective Debye length,

$$\frac{1}{\lambda_D^2\left(r\right)} \equiv \frac{4\pi e^2 n_0\left[r,\phi_0\left(r\right)\right]}{T\left(r\right)}, \tag{2.16}$$

in terms of the effective temperature

$$\frac{1}{T\left(r\right)} \equiv -\frac{1}{n_0}\frac{\partial n_0}{\partial e\phi_0}. \tag{2.17}$$

In writing $\lambda_D^2\left(r\right)$ as a positive quantity use has been made of the fact that $\partial n_0/\partial e\phi_0$ is negative.

We choose $\phi_0\left(r\right)$ so that the first bracket in Eq. (2.15) vanishes. The second bracket is then zero, so $\Delta\phi_0\left(z,r\right)$ satisfies the equation for Debye shielding. In the limit where the Debye shielding is small compared to the plasma dimensions, numerical solutions [28] show that $e\Delta\phi_0\left(z,r\right)/T$ is exponentially small in the plasma interior and grows exponentially as the plasma surface is approached, reaching the value $e\Delta\phi_0/T \sim 1$ at the surface. Near the surface an analytic solution is possible. $\Delta\phi_0\left(z,r\right)$ depends primarily on the coordinate ξ, measured along the local normal to the surface, so Eq. (2.15) reduces to the form

$$\frac{d^2}{d\xi^2}\Delta\phi_0 - \frac{1}{\lambda_D^2}\Delta\phi_0 = 0, \tag{2.18}$$

for which the solution is exponential growth on the spatial scale λ_D. When $e\Delta\phi_0/T$ reaches unity, the density drops (and the simple linearization procedure used here breaks down).

In the experiments of interest [5, 18], the Debye length is small compared to the plasma dimensions, so we develop a reduced description in which the Debye length is taken to the limit $\lambda_D \to 0$. The plasma then has a well-defined length along each field line $2L_0(r)$ and the density is given by

$$n_0(z,r) = \frac{N_0(r)}{2L_0(r)} U\left[L_0(r) - |z|\right], \tag{2.19}$$

where $U(x)$ is a step function. In this Zero Debye Length Reduced Description, the equilibrium is specified by the single function $N_0(r)$. The function $L_0(r)$ is determined by the requirement that $\partial\phi_0/\partial z = 0$ everywhere on the plasma surface, that is, for $|z| = L_0(r)$. The fact that $\partial\phi_0/\partial z$ vanishes on the surface implies that it vanishes throughout the plasma volume.

To prove this statement, note that the Poisson equation plus the z-independence of $n_0(z,r)$ inside the plasma implies the equation

$$\nabla^2 \frac{\partial\phi_0}{\partial z} = -4\pi e \frac{\partial n_0}{\partial z} = 0. \tag{2.20}$$

Since $\partial\phi_0/\partial z$ satisfies the Laplace equation throughout the plasma volume and vanishes on the plasma surface, it must vanish throughout the volume.

The method of obtaining $L_0(r)$ begins by recognizing that at each point along the the correct equilibrium length function, the axial electric fields generated by the trap and the plasma exactly cancel. Should this condition not be satisfied, the plasma would expand or contract axially, until force balance is achieved. This heuristic dynamical description demonstrates the basic principle used to find the equilibrium length $L_0(r)$. Initially, $L_0(r)$ is approximated by some arbitrary, smooth curve $L_0^{(0)}(r)$ (usually a sphere). Next, the axial electric field is computed along this curve. The curve is then adjusted using the normalized electric force at the surface,

$$L_0^{(i+1)}(r) = L_0^{(i)}(r)\left[1+\epsilon\frac{E_z^p\left[L_0^{(i)}(r),r\right]+E_z^t\left[L_0^{(i)}(r),r\right]}{E_z^p\left[L_0^{(i)}(r),r\right]}\right], \tag{2.21}$$

where E_z^t is the trap field, E_z^p is the plasma field, and ϵ is a small parameter chosen for convergence (usually one tenth). Here, the total electric field is normalized by the field due to the plasma in order to speed up convergence in region where the field is small (*e.g.* near the wall). This procedure is iterated until $L_0(r)$ is found [*i.e.*, $L_0^{(n+1)}(r) = L_0^{(n)}(r)$].

The axial electric field component generated by the trap is obtained by differentiating the analytic expression for the potential in Eq. (2.10). The potential created by the plasma is given by the Green function from definition (2.7). The equilibrium plasma density is axisymmetric and uniform along the field lines. The potential produced by such a plasma inside a conducting cylinder is

$$\phi_p(z,r) = e\int_0^R 2\pi r'dr'\int_{-L_0(r')}^{L_0(r')} dz'\frac{N_0(r')}{2L_0(r')}G_0(z,r|z',r'), \tag{2.22}$$

where G_0 is defined in Eq. (2.9). The axial electric field is obtained by differentiating Eq. (2.22) with respect to z, and using the translational invariance of the Green function ($\partial/\partial z = -\partial/\partial z'$)

$$-\frac{\partial\phi_p}{\partial z} = e\int_0^R 2\pi r'dr'\frac{N_0(r')}{2L_0(r')}\{G_0[z,r|L_0(r'),r'] - G_0[z,r|-L_0(r'),r']\}. \tag{2.23}$$

In Fig. 2.4, the zero temperature solution $|z| = L_0(r)$ obtained in this way is compared to a succession of Poisson-Boltzmann solutions in which the temperature is varied. For each finite temperature solution, we define a half-density surface, $|z| = L_{\frac{1}{2}}(r)$, where

$$n\left[z = L_{\frac{1}{2}}(r),r\right] = \frac{1}{2}n(0,r) \tag{2.24}$$

The dashed curves in Fig. 2.4 are these surfaces for the sequence of temperatures ($T = 1.0, 0.1, .01\ eV$). The solid curve is the $T = 0$ or Zero Debye Length Reduced Description solution. This comparison indicates that our equilibrium length function is a reasonable zero Debye length approximation to the plasma density for sufficiently low temperature. In the experiments of interest, the plasma temperature is typically $0.5\ eV$. In regions where the plasma density becomes small, the Debye length is large and our reduced description fails. However, we suppose that these low density regions have a small effect on the overall plasma dynamics.

2.5 Modes

The unperturbed Hamiltonian $H_0 = H_0\left(z, p_z, p_\theta\right)$ is integrable, so we can obtain a canonical transformation to action-angle variables. The first step is to define the bounce action as

$$I = \frac{1}{2\pi} \oint dz' p_z\left[z', H_0, p_\theta\right], \tag{2.25}$$

where $p_z\left[z, H_0, p_\theta\right]$ is obtained by solving Eq. (2.11) for p_z. Both H_0 and p_θ are held constant while carrying out the integral. A generating function for a canonical transformation from $(z, p_z, \theta, p_\theta)$ to $(\psi, I, \Theta, P_\Theta)$ is given by

$$W = \int_0^z dz' p_z\left[z', H_0\left(I, P_\Theta\right), P_\Theta\right] + \theta P_\Theta. \tag{2.26}$$

Taking partial derivatives in the prescribed manner [9] yields the transformation

$$\psi = \frac{\partial W}{\partial I} = \int_0^z \frac{dz'}{v_z\left[z', H_0, P_\Theta\right]} \frac{\partial H_0}{\partial I} \tag{2.27}$$

$$p_\theta = \frac{\partial W}{\partial \theta} = P_\Theta \tag{2.28}$$

$$\Theta = \frac{\partial W}{\partial P_\Theta} = \theta + \int_0^z \frac{dz'}{v_z\left[z', H_0, P_\Theta\right]} \left[\frac{\partial H_0\left(I, P_\Theta\right)}{\partial P_\Theta} - e\frac{\partial \phi_0\left(z, P_\Theta\right)}{\partial P_\Theta}\right]. \tag{2.29}$$

Here, use has been made of the relation $\partial p_z / \partial H_0 = 1/v_z$.

In Eq. (2.29), the bracket

$$\left[\frac{\partial H_0\left(I, P_\Theta\right)}{\partial P_\Theta} - e\frac{\partial \phi_0\left(z, P_\Theta\right)}{P_\Theta}\right] \equiv \delta\omega_E \tag{2.30}$$

is the difference between the bounce averaged rotation frequency and the instantaneous rotation frequency. The second term on the right in Eq. (2.29) is no larger than $\delta\omega_E/\omega_b$, which is small according to our assumed ordering ($\omega_b \gg \omega_E$). Thus, we drop the second term and set $\Theta \simeq \theta$. For convenience, we continue to use the old variables p_θ and θ.

Since the transformation is canonical, the drift kinetic equation is still given by Eq. (2.5), but the Poisson bracket must be evaluated for the variables $(\psi, I, \theta, p_\theta)$.

We assume that there is a small amplitude mode characterized by the potential $\delta\phi\left(z, \theta, p_\theta, t\right)$. The Hamiltonian is then given by

$$H = H_0\left(I, p_\theta\right) + \delta H\left(\psi, I, \theta, p_\theta, t\right), \tag{2.31}$$

where $\delta H = e\delta\phi$. The perturbation in the Hamiltonian gives rise to a perturbation in the distribution $\delta f\left(\psi, I, \theta, p_\theta, t\right)$. Linearizing the drift kinetic equation in the smallness of the perturbation yields

$$\frac{\partial \delta f}{\partial t} + \left[\delta f, H_0\right] + \left[f_0, \delta H\right] = 0. \tag{2.32}$$

By taking into account the functional dependence $H_0 = H_0\left(I, p_\theta\right)$ and $f_0 = f_0\left(I, p_\theta\right)$, the equation can be rewritten as

$$\left[\frac{\partial}{\partial t} + \frac{\partial H_0}{\partial I}\frac{\partial}{\partial \psi} + \frac{\partial H_0}{\partial p_\theta}\frac{\partial}{\partial \theta}\right]\delta f - \frac{\partial \delta H}{\partial \psi}\frac{\partial f_0}{\partial I} - \frac{\partial \delta H}{\partial \theta}\frac{\partial f_0}{\partial p_\theta} = 0. \tag{2.33}$$

Finally, by using $\partial f_0/\partial I = (\partial H_0/\partial I)(\partial f_0/\partial H_0)$ we obtain the result

$$\frac{\partial H_0}{\partial I}\frac{\partial}{\partial \psi}\left(\delta f - \delta H\frac{\partial f_0}{\partial H_0}\right) + \left(\frac{\partial}{\partial t} + \frac{\partial H_0}{\partial p_\theta}\frac{\partial}{\partial \theta}\right)\delta f - \frac{\partial \delta H}{\partial \theta}\frac{\partial f_0}{\partial p_\theta} = 0. \tag{2.34}$$

We solve this equation through an expansion in the small parameter $\omega_E/\omega_b \sim \omega/\omega_b \ll 1$, where $\omega_b = \partial H_0/\partial I$ is the axial bounce frequency, $\omega_E = \partial H_0/\partial p_\theta$ is the rotation frequency and $\partial/\partial t \sim \omega$ is the characteristic frequency of the modes. In zero order, the equation reduces to the form

$$\frac{\partial H_0}{\partial I}\frac{\partial}{\partial \psi}\left(\delta f - \delta H\frac{\partial f_0}{\partial H_0}\right) = 0, \tag{2.35}$$

which has the solution

$$\delta f - \delta H\frac{\partial f_0}{\partial H_0} = \langle \delta f - \delta H\frac{\partial f_0}{\partial H_0}\rangle_\psi, \tag{2.36}$$

or equivalently,

$$\delta f = \langle \delta f\rangle_\psi + \left(\delta H - \langle \delta H\rangle_\psi\right)\frac{\partial f_0}{\partial H_0}. \tag{2.37}$$

Here, the bracket $\langle g\rangle_\psi (I,\theta,p_\theta,t)$ is the ψ-average $(1/2\pi)\int_0^{2\pi} d\psi\, g\,(\psi,I,\theta,p_\theta,t)$, where (I,θ,p_θ,t) are held constant in evaluating the integral. For each (I,θ,p_θ,t), solution (2.37) determines the ψ-dependence of $\delta f\,(\psi,I,\theta,p_\theta,t)$ relative to the ψ-average $\langle \delta f\rangle_\psi (I,\theta,p_\theta,t)$. To obtain an equation for $\langle \delta f\rangle_\psi$, we integrate Eq. (2.34) over ψ, projecting out the large first term. The result is

$$\left(\frac{\partial}{\partial t} + \frac{\partial H_0}{\partial p_\theta}\frac{\partial}{\partial \theta}\right)\langle \delta f\rangle_\psi = \frac{\partial \langle \delta H\rangle_\psi}{\partial \theta}\frac{\partial f_0}{\partial p_\theta}. \tag{2.38}$$

In the Zero Debye Length Reduced Description for the equilibrium, the transformation $(\psi,I,\theta,p_\theta) \to (z,p_z,\theta,p_\theta)$ is such that z-dependence for a function enters only through ψ-dependence. Thus, Eq. (2.37) implies that all z-dependence in the perturbation δf is included in the term

$$e\left(\delta\phi - \langle \delta\phi\rangle_\psi\right)\frac{\partial f_0}{\partial H_0} = e\delta\phi'\frac{\partial f_0}{\partial H_0}, \tag{2.39}$$

where $\delta\phi' \equiv (\delta\phi - \langle\delta\phi\rangle_\psi)$ is the z-dependent part of the perturbed potential. In turn the z-dependent portion of the perturbed density, $\delta n = \int dp_z \delta f$, is given by

$$e\delta\phi'\frac{\partial n_0}{\partial e\phi_0} = -\frac{e\delta\phi'}{T\,(r)}n_0, \tag{2.40}$$

where $T(r)$ is the effective temperature defined in Eq. (2.17). Substituting this density perturbation into the Poisson equation shows that $\delta\phi'$ satisfies the equation for Debye shielding [see Eq. (2.18)]. Thus, we conclude that the mode perturbation exhibits such shielding (*i.e.*, $\partial\delta\phi/\partial z \to 0$) in the plasma interior. Eq. (2.37) then implies that δf and $\delta n = \int dp_z \delta f$ are independent of z (or ψ) in the plasma interior. Within a few Debye lengths of the end, $|\partial\delta\phi/\partial z|$ can become large, either adding to or subtracting from $\partial\phi_0/\partial z$ and, thereby, increasing or decreasing the plasma length locally.

These are the conclusions that are necessary to extend the Zero Debye Length Reduced Description to include modes. We allow for an increment to the plasma half-length, $L(\theta, r, t) = L_0(r) + \delta L(\theta, r, t)$, and for an increment to the z-integrated density, $N(\theta, r, t) = N_0(r) + \delta N(\theta, r, t)$. Substituting these expressions into Eq. (2.19) and linearizing yields the density increment

$$\delta n(z, \theta, r, t) = \left[\frac{\delta N(\theta, r, t)}{2L_0(r)} - \frac{N_0(r)}{2L_0(r)}\frac{\delta L(\theta, r, t)}{L_0(r)}\right] U\left[L_0(r) - |z|\right] + \frac{N_0(r)\,\delta L(\theta, r, t)}{2L_0(r)}\delta\left[L_0(r) - |z|\right], \qquad (2.41)$$

where the delta function in the second term enters through the Taylor expansion for the step function. This term represents a surface shell of density increment associated with the length increment.

From Eq. (2.6), we obtain the relation,

$$\delta\phi(z, \theta, r, t) = e\int_{-\infty}^{+\infty} dz' \int_0^{2\pi} d\theta' \int_0^R r'dr' G(z, \theta, r|z', \theta', r')\,\delta n(z', \theta', r', t). \qquad (2.42)$$

Substituting for $\delta n(z', \theta', r', t)$ from Eq. (2.41) then provides an expression for $\delta\phi(z, \theta, r, t)$ as a linear functional of $\delta N(\theta, r, t)$ and $\delta L(\theta, r, t)$.

The length increment, $\delta L(\theta, r, t)$, is determined as a linear functional of $\delta N(\theta, r, t)$ by the requirement that $\partial\delta\phi/\partial z = 0$ at $|z| = L_0(r)-$. Here, the minus sign indicates that the constraint $\partial\delta\phi/\partial z = 0$ is to be imposed just inside the shell of surface charge [see second term in Eq. (2.41)]. Of course, the normal component of the electric field is discontinuous across a sheet of surface charge. One can show that this constraint implies that $\partial\delta\phi/\partial z$ vanishes throughout the plasma interior.

To include the effect of the modified length [*i.e.*, $L_0(p_\theta) \rightarrow L_0(p_\theta) + \delta L(\theta, p_\theta, t) = L(\theta, p_\theta, t)$] in the Hamiltonian, we must use the modified length in the definition of the action, $I = (1/2\pi)\oint dz p_z = |p_z| 2L(\theta, p_\theta, t)/\pi$. The Hamiltonian is then given by

$$H = \frac{I^2\pi^2}{8mL^2\left(\theta, p_\theta, t\right)} + e\phi\left(\theta, p_\theta, t\right), \tag{2.43}$$

where $\phi(\theta, p_\theta, t)$ is the z-independent potential inside the plasma. This Hamiltonian describes the bounce averaged transverse motion and assumes the ordering $\omega_b \gg \omega_E \sim \omega$. The ratio of the first term to the second is $T/e\phi_0 \sim (\lambda_D/r_p)^2$, so in the limit of zero Debye length we drop the first term and set $H \simeq e\phi(\theta, p_\theta, t)$. We will discuss the effect of the first term in Section 2.8.

Just as the equilibrium is specified by the single function $N_0\left(r\right)$, the modes are specified by the single function $\delta N\left(\theta, r, t\right)$. The reduced description is completed by an equation for the evolution of $\delta N\left(\theta, r, t\right)$, which we obtain from Eq. (2.38). In this equation, we set $\omega_E = \partial H_0/\partial p_\theta = \partial e\phi_0/\partial p_\theta$ and $\langle\delta H\rangle = e\delta\phi(\theta, p_\theta, t)$, where $\phi_0(p_\theta)$ and $\delta\phi(\theta, p_\theta, t)$ are the z-independent equilibrium and mode potentials, respectively. Integrating Eq. (2.38) over $2\pi dI$ then yields

$$\left[\frac{\partial}{\partial t} + \omega_E\left(r\right)\frac{\partial}{\partial\theta}\right]\delta N\left(\theta, r, t\right) = -\frac{c}{Br}\frac{\partial\delta\phi}{\partial\theta}\frac{\partial N_0}{\partial r}\left(r\right), \tag{2.44}$$

where $\delta N = 2\pi\int_0^\infty dI\langle\delta f\rangle_\psi$ and $N_0 = 2\pi\int_0^\infty dI f_0$.

To examine a single mode, we let perturbed quantities vary as $\exp\left(i\ell\theta - i\omega t\right)$, so that Eqs. (2.41), (2.42) and (2.44) take the form

$$\delta n_{\ell,\omega}(z,r) = \left[\frac{\delta N_{\ell,\omega}(r)}{2L_0(r)} - \frac{N_0(r)}{2L_0(r)}\frac{\delta L_{\ell,\omega}(r)}{L_0(r)}\right] \times$$

$$\times\, U\left[L_0(r) - |z|\right] + \frac{N_0(r)\,\delta L_{\ell,\omega}(r)}{2L_0(r)}\delta\left[L_0(r) - |z|\right] \tag{2.45}$$

$$\delta\phi_{\ell,\omega}(z,r) = e\int\limits_{-\infty}^{+\infty} dz' \int\limits_0^R r'dr' G_\ell(z,r|z',r')\,\delta n_{\ell,\omega}(z',r',t)\,. \tag{2.46}$$

$$[\omega - \ell\omega_E(r)]\delta N_{\ell,\omega}(r) = \frac{c\ell}{Br}\frac{\partial N_0}{\partial r}\delta\phi_{\ell,\omega}(r)\,, \tag{2.47}$$

where use has been made of definition (2.9). Finally, the length increment $\delta L_{\ell,\omega}(r)$ is determined as a functional of $\delta N_{\ell,\omega}(r)$ through the constraint

$$0 = \frac{\partial\delta\phi_{\ell,\omega}}{\partial z}|_{z=L_0(r)-} = e\int\limits_0^R r'dr'\left[\frac{\delta N_{\ell,\omega}(r')}{2L_0(r')} - \frac{N_0(r')\,\delta L_{\ell,\omega}(r')}{2L_0^2(r')}\right] \times$$

$$\times \left\{G_\ell\left[L_0(r)-,r|-L_0(r'),r'\right] - G_\ell\left[L_0(r)-,r|L_0(r'),r'\right]\right\}$$

$$+\, e\int\limits_0^R r'dr'\frac{N_0(r')\,\delta L_{\ell,\omega}(r')}{2L_0(r')} \times$$

$$\times \left\{\frac{\partial G_\ell}{\partial z}\left[L_0(r)-,r|-L_0(r'),r'\right] + \frac{\partial G_\ell}{\partial z}\left[L_0(r)-,r|L_0(r'),r'\right]\right\}, \tag{2.48}$$

where use has been made of the fact that G_ℓ depends on z and z' only through the combination $z - z'$.

Before turning to the numerical implementation of these equations, we develop an orthogonality relation for the eigenmodes $\{\delta N_{\ell,\omega}(r)\}$ and discuss the representation of a general perturbation as a sum over the eigenmodes. We also obtain a necessary condition for instability [*i.e.*, $Im(\omega) = \gamma > 0$]. These results are generalizations of similar results obtained earlier for the case of an infinitely long column[3, 33].

To start, we multiply Eq. (2.47) by $\delta n_{\ell,\omega'}(z,r)\, r/N_0'$ and integrate over $rdrdz$, to obtain the relation

$$\omega \int_0^R r dr \delta N_{\ell,\omega'}(r)\, \delta N_{\ell,\omega}(r) \left[\frac{1}{r}\frac{\partial N_0}{\partial r}\right]^{-1}$$

$$- \ell \int_0^R r dr \omega_E(r)\, \delta N_{\ell,\omega'}(r)\, \delta N_{\ell,\omega}(r) \left[\frac{1}{r}\frac{\partial N_0}{\partial r}\right]^{-1}$$

$$= \frac{c\ell}{B} \int_{-\infty}^{+\infty} dz \int_0^R r dr \delta\phi_{\ell,\omega}(r)\, \delta n_{\ell,\omega'}(z,r), \tag{2.49}$$

where use has been made of the definition $\int_{-\infty}^{+\infty} dz\, \delta n_{\ell,\omega'}(z,r) = \delta N_{\ell,\omega'}(r)$ on the left hand side. The function $\delta\phi_{\ell,\omega}(z,r)$ is equal to $\delta\phi_{\ell,\omega}(r)$ in the plasma interior, but can differ by order T in the end sheath. In our reduced description, where terms of order $T \to 0$ are neglected, $\delta\phi_{\ell,\omega}(r)$ can be replaced by $\delta\phi_{\ell,\omega}(z,r)$ in the integrand on the right hand side of Eq. (2.49). By using the Green function relation (2.46), the right hand side can be rewritten in a symmetric form

$$\omega \int_0^R r dr \delta N_{\ell,\omega'}(r)\, \delta N_{\ell,\omega}(r) \left[\frac{1}{r}\frac{\partial N_0}{\partial r}\right]^{-1}$$

$$- \ell \int_0^R r dr \omega_E(r)\, \delta N_{\ell,\omega'}(r)\, \delta N_{\ell,\omega}(r) \left[\frac{1}{r}\frac{\partial N_0}{\partial r}\right]^{-1}$$

$$= \frac{ec}{\ell B} \int_{-\infty}^{+\infty} dz \int_0^R r dr \int_{-\infty}^{+\infty} dz' \int_0^R r' dr' \delta G_\ell(z,r|z',r')\, \delta n_{\ell,\omega}(z',r')\, \delta n_{\ell,\omega'}(z',r'). \tag{2.50}$$

A similar equation is obtained by interchanging ω and ω'. Subtracting the two equations yields the relation

$$0 = (\omega - \omega') \int_0^R r dr \delta N_{\ell,\omega'}(r)\, \delta N_{\ell,\omega}(r) \left[\frac{1}{r}\frac{\partial N_0}{\partial r}\right]^{-1}. \tag{2.51}$$

Thus, the eigenfunctions $\delta N_{\ell,\omega}(r)$ and $\delta N_{\ell,\omega'}(r)$ for which $\omega \neq \omega'$ satisfy the orthogonality condition

$$0 = \int_0^R r dr \delta N_{\ell,\omega'}(r)\, \delta N_{\ell,\omega}(r) \left[\frac{1}{r}\frac{\partial N_0}{\partial r}\right]^{-1}. \tag{2.52}$$

One might worry that the integrand diverges at a point where $[(1/r)(\partial N_0/\partial r)]$ passes through zero, but this is not the case. Eq. (2.46) implies that $\delta N_{\ell,\omega}(r)$ and $\delta N_{\ell,\omega'}(r)$ are both proportional to $[(1/r)(\partial N_0/\partial r)]$, so in fact the integrand vanishes at a point where $[(1/r)(\partial N_0/\partial r)]$ passes through zero.

In the usual manner, a general perturbation can be expressed as a sum over the eigenmodes

$$\delta N(\theta, r, t) = \sum_{\ell,\omega} a_{\ell,\omega} \delta N_{\ell,\omega}(r) \exp[i\ell\theta - i\omega t], \tag{2.53}$$

where the orthogonality conditions (in r and θ) allow us to determine the coefficients $a_{\ell,\omega}$ in terms of the initial conditions

$$a_{\ell,\omega} = \frac{\int_0^R r dr \left[(1/r)(\partial N_0/\partial r)\right]^{-1} \delta N_{\ell,\omega}(r) \int_0^{2\pi} \frac{d\theta}{2\pi} e^{-i\ell\theta} \delta N(\theta, r, t=0)}{\int_0^R r dr \left[(1/r)(\partial N_0/\partial r)\right]^{-1} \delta N_{\ell,\omega}^2(r)}. \tag{2.54}$$

In Eq. (2.53), the sum over ω typically contains a continuum portion.

One caveat concerns the completeness of the set $\{\delta N_{\ell,\omega}(r)\}$ in the special case where $[(1/r)(\partial N_0/\partial r)]$ vanishes over a finite interval. Over this interval all of the $\{\delta N_{\ell,\omega}\}$ vanish, so sum (2.53) can represent only initial perturbations that vanish on the interval. Physically, this is not a problem, since all perturbations that arise through $\mathbf{E} \times \mathbf{B}$ drift dynamics [*i.e.*, through Eq. (2.46)] satisfy this condition.

An easily obtained variant of Eq. (2.51) is the relation

$$0 = (\omega - \omega'^{*}) \int_0^R r dr \delta N_{\ell,\omega'}^{*}(r)\, \delta N_{\ell,\omega}(r) \left[\frac{1}{r}\frac{\partial N_0}{\partial r}\right]^{-1}. \tag{2.55}$$

Setting $\omega = \omega' = \omega_r + i\gamma$ and using Eq. (2.46) yields the result

$$0 = \int_0^R r dr \frac{\left|\ell \delta\phi_\ell (r)\right|^2 \gamma}{\left[\omega_r - \omega_E (r)\right]^2 + \gamma^2} \frac{1}{r} \frac{\partial N_0}{\partial r}. \tag{2.56}$$

Thus, instability ($\gamma > 0$) is possible only if $\partial N_0 / \partial r$ changes sign over the interval $[0, R]$. For a confined column, $\partial N_0 / \partial r$ must be negative at large r, so instability requires that there be a region where $\partial N_0 / \partial r > 0$. This modified Rayleigh criterion has been found before[8, 27] and has an analogy in the infinite length theory[1, 3], in which the z-integrated density is replaced by local density.

We emphasize that the condition $\partial N_0 / \partial r > 0$ is necessary, but not sufficient, for an instability. For example, a plasma with a length function that increases with radius near $r = 0$ can have uniform local density, $n_0(r) = n_0$, and still have $\partial N_0 / \partial r > 0$ near the axis. Such a plasma is a shear-free global thermal equilibrium[3, 7], which is known to be stable.

2.6 Numerical Implementation

The equations are discretized at radial points $\{r_i : i = 1 \ldots N\}$. The plasma state is completely determined by the vector $\{\delta N_{\ell,\omega} (r_i)\}$. The vector $\{\delta L_{\ell,\omega} (r_i)\}$ is determined by the discretized form of Eq. (2.48),

$$\sum_i A_{ji} \delta L_{\ell,\omega} (r_i) = \sum_i B_{ji} \delta N_{\ell,\omega} (r_i) \tag{2.57}$$

which can be inverted to obtain

$$\delta L_{\ell,\omega} (r_k) = \sum_{i,j} A_{kj}^{-1} B_{ji} \delta N_{\ell,\omega} (r_i)$$

Substituting this into Eq. (2.46) then yields an expression for the potential inside the plasma

$$\delta\phi_{\ell,\omega} (r_j) = \sum_i C_{ji} \delta N_{\ell,\omega} (r_i) \tag{2.58}$$

We can now form an eigenvalue equation using Eq. (2.47)

$$\omega \delta N_{\ell,\omega}\left(r_j\right) = \ell \omega_E\left(r_j\right) \delta N_{\ell,\omega}\left(r_j\right) + \frac{c\ell}{Br_j}\frac{\partial N_0}{\partial r_j}\sum_i C_{ji}\delta N_{\ell,\omega}\left(r_i\right). \qquad (2.59)$$

This matrix can be diagonalized using standard techniques.

The difficulties encountered in the numerical implementation primarily concern the convergence of the Green function [see Eqs. (2.7) and (2.8)] and its axial derivative. The convergence of these expressions is provided by the spatial separation of the source and observation points. In form (2.7), the exponential ensures convergence when its argument becomes large compared with unity. For $n \gg 1$, $\chi_{\ell n} \sim n\pi$ and the number of terms required in the matrix element summation is roughly $R/|z-z'|$. This result illustrates the two main reasons for incurring additional computational costs. First, as the number of radial points is increased, the space between nearest neighbors is reduced and more terms will contribute in the summation. Therefore, increasing the spatial resolution to obtain greater accuracy will not only result in larger matrices, but the summation required to compute neighboring matrix elements converges more slowly as well. Second, as the size of the plasma is reduced with respect to the cylindrical wall, the spacing of grid points will also decrease. This implies that for a given number of discretization points, the eigenmode solution of smaller plasma requires more computation time. An example will illustrate this point. In Sec. 2.7.1 below, we compare our results to an analytic solution obtained by Dubin. Dubin's theory assumes a quadratic trap potential and neglects the image charges induced in the conducting wall. To satisfy these requirements in our system, we choose a small plasma whose radius is one tenth of the wall radius. The solution for such a plasma requires three times more cpu runtime than a similar plasma whose radius is one half of the wall radius, while 200 radial grid points are used in each case. The solution of the latter requires four minutes on a 300 MHz Pentium II.

We are not always guaranteed that summation in form (2.7) will converge for arbitrarily many terms. For example, non-monotonic length functions may have $L_0(r_1) = L_0(r_2)$ for $r_1 \neq r_2$. In this situation, the argument of the exponential vanishes and it becomes advantages to use the integral expression for the Green function in form (2.8). This integral converges due to the asymptotic behavior of the modified Bessel functions. For values of $k \gg 1$, the integrand varies as $k^{-1} \exp\left[-k\left(r_> - r_<\right)\right]$, which becomes small when $k > |r - r'|$. Therefore, the integral form of the Green function can be used to calculate matrix elements for which the summation in (2.7) fails or converges too slowly.

The discretized surface charge perturbation $\{\delta L(r_i)\}$ represents a series of ring charges located at $[r_i, L_0(r_i)]$. These coordinates are also the positions at which $\partial\delta\phi/\partial z$ is evaluated in constraint (2.48). When the charged ring source and the observation point are collocated, which is the case for the diagonal elements of A_{ji}, the electric field diverges. To avoid this situation, we note that in this instance the contribution from the image charge induced in the conducting wall is negligible. Therefore, this region of the plasma is well-approximated by the surface charge in free space which is produced upon rotating the line segment connecting neighboring grid points about the z-axis. The field evaluation point is on the interior side of this surface and can be taken arbitrarily close. The axial electric field is dominated by the local surface charge and we may assume this field is adequately described as $\delta E_z = \hat{z} \cdot 2\pi\sigma\hat{n}$, where $\hat{n}$ is the inward normal to the surface.

In general, the accuracy of a numerical solution to a discretized equation is determined by the total number of evaluation points. Higher accuracy can be obtained at the cost of larger memory requirements and longer cpu run-times. For this calculation, finer grids also increase the difficulty of performing the summations.

As the grid spacing is decreased, more and more terms in the sums are needed for accurate evaluation of the matrix elements. In the solutions presented below no more than one million terms were kept in the summations. This was sufficient to compute matrices of order 400, and achieve convergence in the solutions. As is customary in the numerical solution of equations, convergence is assumed when a large increase in spatial resolution produces little or no change in the results.

2.7 Results

2.7.1 Comparison to Dubin Modes

Although our model is analytically intractable for the general case, there is a special case for which we can compare our numerical results to the predictions of an analytic theory. A small uniform density plasma that is confined in the central region of a trap, where the trap potential is nearly quadratic, has the shape of a spheroid. Using spheroidal coordinates and cold fluid theory, Dubin[6] obtained the complete spectrum of electrostatic modes. For a special class of these modes, the mode potential does not vary axially inside the plasma (*i.e.*, $\partial\delta\phi/\partial z = 0$), so our numerical solutions should include these modes. Figure 2.5 compares our numerical solutions for the frequencies of these modes to the predictions of Dubin. The frequencies are plotted as a function of plasma aspect ratio (l_p/r_p), and results for the first five azimuthal mode numbers ($\ell = 1, \ldots, 5$) are shown. The results of our calculations are in excellent agreement with Dubin's predictions.

An important distinction between Dubin's analysis and ours is that he uses cold fluid theory and we use bounce averaged dynamics. Both of these approximations are useful, but they apply to different classes of experiments. Cold fluid theory requires the axial bounce frequency to be small (*i.e.*, $\omega, \omega_E \gg \omega_b \to 0$), and bounce averaged dynamics requires it to be large (*i.e.*, $\omega_b \gg \omega, \omega_E$). Note that both Dubin's analysis and ours assume that the Debye length is small. As mentioned earlier, it may seem that large bounce frequency and small Debye length are not compatible, but the two inequalities $\omega_b \gg \omega, \omega_E$ and $\lambda_D \ll l_p$ can both be satisfied provided that $\omega_p/\Omega_c \ll \lambda_D/l_p$. In cold fluid theory, the potential for a typical mode admits z-variation inside the plasma, whereas, such variation is prohibited (Debye shielded out) in our analysis. The fact that Dubin's analysis leads to a class of modes with no z-variation is presumably an accident of the spheroidal geometry.

A further check on the validity of our solutions concerns the Debye shielding condition. In our development, we assumed that the mode potentials are independent of axial position inside the plasma. This constraint is imposed by setting the z-electric field equal to zero just inside the surface. After solving for the modes, we can check to see that this was sufficient to guarantee z-independence throughout the plasma interior. Fig. 2.6 plots the mode potentials due to the z-integrated density perturbation, the length perturbation, and their sum vs. axial position along an arbitrary field line ($r = r_p/6$). The z-electric fields from the two perturbations cancel everywhere inside as expected. This consistency check has been verified for other modes and along other field lines as well.

2.7.2 New Modes

One effect of finite column length is to introduce a new class of discrete diocotron-like modes for the case of plasmas with low shear in the rotational flow. The modes take their simplest form for a uniform density plasma, which is shear-free. An infinitely long column of uniform density supports only a single discrete diocotron-like mode for each azimuthal mode number[4]. In contrast, a finite length column of uniform density supports many additional discrete diocotron-like modes.

These modes were predicted by Finn *et al.*[8], who drew an analogy between the new modes and Rossby waves in the quasigeostrophic β-plane approximation[32]. To obtain a simple equation for the modes, these authors set the perturbation in plasma length equal to zero (*i.e.*, $\delta L_{\ell,\omega} = 0$). Although this approximation is not rigorously correct and we cannot expect quantitative agreement with the numerical results, the analysis captures the essence of the new modes and has the great advantage of simplicity.

Setting $\delta L_{\ell,\omega} = 0$ and using Eqs. (2.45) and (2.47) yields

$$4\pi e \delta n_{\ell,\omega}(r) = \frac{4\ell\omega_E}{\ell\omega_E - \omega}\kappa(r)\delta\phi_{\ell,\omega}(r), \tag{2.60}$$

where

$$\kappa(r) \equiv -\frac{1}{2rL_0(r)}\frac{\partial L_0}{\partial r}. \tag{2.61}$$

Inside the plasma, $\delta\phi_{\ell,\omega}(r)$ then satisfies the 2-D Poisson equation

$$\frac{1}{r}\frac{d}{dr}r\frac{d\delta\phi_{\ell,\omega}}{dr} - \frac{\ell^2}{r^2}\delta\phi_{\ell,\omega}(r) + \frac{4\ell\omega_E}{\ell\omega_E - \omega}\kappa(r)\delta\phi_{\ell,\omega}(r) = 0. \tag{2.62}$$

As a further simplification, Finn *et al.* assume that $\kappa(r)$ is constant out to the wall at $r = R$. The solution is then given by a Bessel function.

$$\delta\phi_{\ell,\omega}(r) = A J_\ell\left[\sqrt{\frac{4\ell\omega_E\kappa}{\ell\omega_E - \omega}}r\right], \tag{2.63}$$

and the boundary condition $\delta\phi_{\ell,\omega}(R) = 0$ then yields the dispersion relation

$$\omega - \ell\omega_E = -\frac{4\ell\omega_E\kappa R^2}{\chi_{\ell n}^2}, \tag{2.64}$$

where $\chi_{\ell n}$ is the n^{th} zero of J_ℓ. For κ positive corresponding to negative $L_0'(r)$, the modes are down shifted in azimuthal phase velocity from the plasma rotation frequency by a small amount that tends to zero as the number of radial nodes in the eigenfunction increases.

For a more realistic case where the plasma does not extend to the wall but κ is positive, Eq. (2.62) again describes a sequence of modes with phase velocities down shifted from the rotation frequency by a small amount tending to zero as the number of nodes increases. Of course, κ need not be positive everywhere. We will consider an example where κ is negative for small r and positive for large r. In this case, Eq. (2.62) implies two sets of new modes: a set with down shifted phase velocity that lives in the region of positive κ and a set with up shifted phase velocity that lives in the region of negative κ. The sign of the shift follows from the requirement that $\kappa/(\ell\omega_E - \omega)$ be positive for oscillatory solutions of Eq. (2.62). We find that these predictions are born out at least qualitatively by our numerical solutions of the full equations.

As a first example, we consider the $\ell = 1$ modes of a uniform density column in a trap characterized by $R = Z = 3.5$ cm and $V = 27$ Volts. Inside this trap we have a nonneutral plasma whose radius is 1.75 cm and whose uniform local density is $n_0 = 10^7$ cm^{-3}. The equilibrium length $L_0(r)$ is obtained using a slightly modified algorithm which maintains a constant local density as opposed to a constant z-integrated density and is shown in Fig. 2.7. Note that $L_0'(r)$ is negative corresponding to positive κ. As expected this plasma supports many new discrete eigenmodes in addition to the usual diocotron mode. Fig. 2.8 shows the lowest ten eigenfrequencies (normalized to the plasma rotation frequency). The lowest frequency mode is the usual diocotron mode. Its eigenfunction is $\partial N_0/\partial r$ and its motion is a displacement of the column off-axis and the subsequent rotation of the entire column about the trap axis. Fig. 2.9 gives the z-integrated density perturbations for the first three eigenmodes. The modes are indexed by a radial wave number n_r which indicates the number of radial nodes in the eigenfunction. As the radial index increases, the mode frequencies approach the rotation frequency.

These modes are all discrete modes as opposed to continuum modes which exist for columns with shear in the rotational flow. Note that all the frequencies are lower than the rotation frequency of the column. This is a consequence of the monotonically decreasing length function (*i.e.*, $\kappa > 0$).

There are equilibria whose length functions do not decrease monotonically with radius. Such equilibria can exist in standard Malmberg-Penning traps when the plasma radius is close to that of the trap. However, to better illustrate the effect of hollow end shape, we will consider a modified Malmberg-Penning trap in which two small ($r = R/50$) conducting rings are placed just outside the plasma ends and coaxial with the trap. To obtain significantly hollow end shapes, we bias the rings to an appropriate positive potential. In principle, we should also modify our Green function to account for the image charges induced on these rings by the mode perturbations. However, if the rings are sufficiently small we can safely ignore these images. Fig. 2.10(a) shows a hollow end shape equilibrium. Here the uniform local plasma density is $n_0 = 10^7$ cm^{-3}, $R = Z = 3.5$ cm, $V = 21$ Volts and the additional conductors are located at $z = \pm 2.625$ cm. Fig. 2.10(b) shows the eigenmode frequencies of the system. In addition to the slow modes discussed earlier, there are modes which rotate faster than the column. The presence of both slow and fast modes on the same column is a result of the length function having a radial derivative which changes sign. As expected, the density perturbations associated with the fast (slow) modes are localized where the length function is increasing (decreasing) with radius.

2.7.3 Shear Profiles

The discrete modes of a rigid rotor plasma can be destroyed by the introduction of shear into the $\mathbf{E} \times \mathbf{B}$ flow. For an infinite length column, the $\ell > 1$

diocotron modes are absorbed into the continuum[2] when they become resonant with the plasma rotation frequency.

Finite length columns also exhibit this phenomenon. As the local density profile is smoothed, the high n_r modes are absorbed into the continuum as they become resonant with the fluid. The z-integrated density eigenfunctions of these modes are no longer smooth functions indexed by a radial wave number, but become discontinuous at the resonant radius. For $\ell = 1$, a plasma with significant shear and a monotonically decreasing length function retains only its center of mass discrete mode. All other eigenmodes are part of the continuum. Experimentally prepared profiles typically contain shear and this may explain why the higher order modes have not been observed.

For monotonically decreasing $n_0(r)$, only modes which rotate slower than the central rotation frequency will become resonant with the plasma rotation and are absorbed into the continuum. However, hollow end shape plasmas support modes with azimuthal phase velocities above the highest rotation frequency. These modes remain discrete in the presence of shear and may be observable experimentally. Fig. 2.11(a) shows a local density profile which is constant throughout the column and falls smoothly to zero near the edge. Fig. 2.11(b) is the equilibrium length function for this density profile and is a non-monotonic function of radius. In Fig. 2.12(a), we plot the spectrum of eigenmodes for this system. Except for the lowest frequency center of mass mode, all of the discrete modes with frequencies lower than the central rotation frequency have become part of the continuum. The addition of more grid points will fill in the continuum with more modes. On the contrary, the modes which rotate faster than the plasma are discrete and remain separated from each other by fixed frequency intervals as the spatial resolution is increased. The z-integrated density perturbations for the fastest mode and one of the discrete modes are shown in Fig. 2.12(b). The solid curve represents the fast, discrete eigenmode. The perturbation is most prominent for small radii where the length function is increasing with radius and is smallest at larger radii where the length function is decreasing. The dashed curve is a continuum eigenmode and exhibits the characteristic discontinuity at the resonant radius.

2.7.4 Diocotron Instability for Azimuthal Mode Number $\ell = 1$

Another problem where finite column length plays an important role is the $\ell = 1$ diocotron instability. As mentioned earlier, a necessary condition for diocotron instabilities is that $N_0(r)$ be non-monotonic. For an infinitely long column, a normal mode analysis[22] predicts neutral stability [*i.e.*, $\mathrm{Im}(\omega) = 0$] for all $\ell = 1$ modes, and an initial value analysis predicts the possibility of algebraic growth (*i.e.*, $\delta n \propto \sqrt{t}$). However, experiments[5, 18] clearly exhibit exponential growth for $\ell = 1$ modes.

Smith[34] and Finn *et al.*[8] have argued theoretically that the exponential growth is due to finite column length. Likewise, our numerical solutions find the possibility of exponential growth for $\ell = 1$ modes. However, we will find that quantitative agreement with the measured growth rates and frequencies requires the inclusion of a kinetic effect (see Sec. 2.8).

First we examine the results from the zero Debye length theory (no kinetic effect). Consider the z-integrated density profile in Fig. 2.13(a). Fig. 2.13(b) shows the equilibrium length function calculated for $R = 3.5$ cm, $Z = 10.4$ cm and $V = 60$ Volts. The spectrum of eigenmode frequencies for this system is given in Fig. 2.14(a). We can clearly see the continuum, the discrete stable mode frequency and the two complex conjugate frequencies of the unstable mode. The eigenfunctions of the discrete stable mode and the unstable mode are shown in Fig. 2.14(b). The eigenfunction of the stable mode is $\partial N_0/\partial r$ and represents the usual center of mass mode. The unstable mode eigenfunction has a global character and vanishes at the radius where the z-integrated density is largest. The z-integrated density profile in Fig. 2.13(a) is a smooth fit to an experimental profile. The experiment measured a growth rate of .045 and a frequency of .99 (normalized to $\omega_E(0) = 2\pi e n_0(0)c/B$). These values are quite different than the computed values of .013 and 1.17. These discrepancies are common to other density profiles and length functions. We will return to this subject in Sec. 2.8.

Finn *et al.*[8] cite two finite length effects which contribute to the $\ell = 1$ instability: curvature in the end shape and variation in the plasma length due to the presence of the mode. Their growth rates due to curvature effects are compared with our results in Fig. (2.15) for two different hollow density profiles. The curvature κ [defined in Eq. (2.61)] is obtained by fitting the equilibrium length function to a quadratic near $r = 0$. For large values of κ this is a reasonable approximation and the two theories obtain similar growth rates. As the end cap voltages are increased, the curvature near the trap axis tends to zero and the results differ greatly. Finn *et al.*[8] also find that the perturbation of the plasma length is a source of instability and obtain finite growth rates for plasmas with zero curvature near $r = 0$. However, the length perturbation is included by using a boundary condition that is chosen for analytical convenience rather that fidelity to the experimental geometry. Our method requires numerical implementation, but more accurately reflects the experimental geometry. This distinction makes comparison of growth rates due to length perturbations not possible.

Although the finite length theory calculations predict the existence of exponential instabilities in hollow columns, the quantitative agreement with the experiments is poor. The calculations consistently find growth rates 4 to 5 times smaller and real frequencies 20-30% larger than the values measured in the experiments. However, these discrepancies may be the result of kinetic effects and the specific manner in which the hollow density profiles are created.

2.8 Kinetic Corrections

In this section, we include a kinetic correction that can be important even though it is of order λ_D^2. Linearizing the Hamiltonian (2.43) with respect to $\delta\phi$ and δL yields $H = H_0 + \delta H$, where

$$H_0 = \frac{I^2\pi^2}{8mL_0^2(p_\theta)} + e\phi_0(p_\theta) \tag{2.65}$$

and

$$\delta H = e\delta\phi(\theta, p_\theta, t) - \frac{I^2\pi^2}{4mL_0^3(p_\theta)}\delta L(\theta, p_\theta, t). \tag{2.66}$$

Substituting into the kinetic equation (2.38) and decomposing into Fourier components in t and θ yields the result

$$\begin{aligned}&\left[\omega_r + i\gamma - \ell\omega_E + \frac{\ell I^2\pi^2}{4mL_0^3(p_\theta)}\frac{\partial L_0}{\partial p_\theta}\right]\langle\delta f_{\ell,\omega}\rangle_\psi(p_\theta, I)\\ &= -\,\ell\left[e\delta\phi_{\ell,\omega}(p_\theta) - \frac{I^2\pi^2}{4mL_0^3(p_\theta)}\delta L_{\ell,\omega}\right]\frac{\partial f_0}{\partial p_\theta}(p_\theta, I).\end{aligned} \tag{2.67}$$

Since the mode of interest here is unstable, the mode frequency is expressed as a complex quantity explicitly ($\omega \to \omega_r + i\gamma$).

The term involving $\delta L_{\ell,\omega}$ is order $(\lambda_D/\Delta)^2$ smaller than the $\delta\phi_{\ell,\omega}$ term and can be ignored (Δ is the scale length on which the potential varies and is on the order of the plasma radius). However, the I-dependent term on the left hand side must be kept since near the resonance $\omega_r - \omega_E$ vanishes and the growth rate γ is assumed to be small. Thus, we obtain

$$\langle \delta f_{\ell,\omega} \rangle_\psi = \frac{-\ell e \delta\phi_{\ell,\omega} \frac{\partial f_0}{\partial p_\theta}}{\omega + i\gamma - \ell\omega_E + \frac{\ell I^2 \pi^2}{4mL_0^3(p_\theta)} \frac{\partial L_0}{\partial p_\theta}}. \tag{2.68}$$

Integrating over I and multiplying by $\omega_r + i\gamma - \ell\omega_E$ produces the kinetic eigenvalue equation

$$(\omega_r + i\gamma - \ell\omega_E)\delta N_{\ell,\omega} = -\ell e \delta\phi_{\ell,\omega}(\omega_r + i\gamma - \ell\omega_E) \int_0^\infty \frac{2\pi dI \frac{\partial f_0}{\partial p_\theta}}{\omega_r + i\gamma - \ell\omega_E + \frac{\ell I^2 \pi^2}{4mL_0^3(p_\theta)} \frac{\partial L_0}{\partial p_\theta}}. \tag{2.69}$$

Setting the term involving I in the denominator to zero results in the non-kinetic eigenvalue equation (2.47). The kinetic correction represents the dependence of the bounce averaged rotation frequency on the axial particle energy. In order to turn around at the ends, the fast particles must receive a larger impulse. Since the electric force providing this change in momentum is aligned normal to the surface of the plasma, there is both an impulse in z and in r provided the ends are not flat (note the dependence on the radial derivative of L_0). Therefore, particles with different axial energies have different bounce averaged rotation frequencies and plasma particles at several different radii can be in resonance with the unstable mode. We will show later that the new I-dependent term substantially affects the behavior of the unstable mode and is sensitive to the details of the particle distribution function.

The inclusion of the kinetic correction to the rotation frequency in our eigenvalue equation produces a matrix operator which depends functionally on the frequency of the eigenmode. Since the mode frequency is not known *a priori*, the discretized operator cannot be diagonalized directly. However, we are only considering one particular mode in the eigenspectrum and the kinetic correction to the eigenvalue of this mode is obtained using the following iterative technique. First, the non-kinetic unstable mode frequency, $\omega^{(0)} + i\gamma^{(0)}$ is substituted into the right hand side of Eq. (2.69). Next, the integral over I is performed. The result is a standard eigenvalue problem. After diagonalizing the resulting system of discretized equations, the adjusted unstable mode frequency, $\omega^{(1)} + i\gamma^{(1)}$, is identified. The new frequency is then substituted back into Eq. (2.69) and this procedure is repeated until the mode frequency converges to a stationary value. This method is successful provided the temperature is increased slowly. Also, this method will work for an arbitrary distribution function, since the integral over I may be performed numerically.

The distribution of axial particle velocities can be greatly affected by the experimental method used to create the hollow z-integrated density profiles. Initially, a monotonic column is created and held in the trap until local thermal equilibrium is established along the field lines. Therefore, the initial distribution of axial particle velocities is a Maxwellian and the temperature is typically uniform in radius. Using action-angle variables, the initial distribution takes the form

$$f_0^i\left(p_\theta, I\right) = \frac{N_0^i}{\sqrt{2\pi^3 \bar{I}^2}} \exp\left(-\frac{I^2}{2\bar{I}^2}\right), \tag{2.70}$$

where $\bar{I} = (2L_0^i/\pi)(mT)^{1/2}$ and the superscript i stands for initial. The axial confining potential at one end is then lowered and the more energetic particles escape from the trap. Since the plasma potential is highest (and the trap potential is lowest) on-axis, more particles are lost near the center and the resulting z-integrated density profile is hollow. In previous experiments, the confining potentials have been changed on a time scale comparable to a bounce period and the resulting distribution function of the hollowed column is not readily found.

In order to illustrate the effect the hollowing process can have on the instability, we will consider an experimental situation for which the distribution function is known. Specifically, the confining potential can be lowered and raised slowly with respect to a bounce period. Under such circumstances, the bounce action of the remaining particles is invariant. Therefore, the number of particles along a given field line with action $I \leq \hat{I}(p_\theta)$ remains fixed,

$$f_0^f(p_\theta, I) = \begin{pmatrix} f_0^i(p_\theta, I) & I \leq \hat{I} \\ 0 & I > \hat{I} \end{pmatrix} \tag{2.71}$$

and the superscript f indicates final. The final distribution function is a truncated Maxwellian. In truth, the bounce action of particles near the separatrix is not conserved. Presumably, these non-adiabatic particles will smooth out the distribution function near the truncation point. However, results obtained for artificially smoothed distribution functions are not substantially different. Because the instability growth rate is larger than the collision frequency, the velocity distribution does not have a chance to relax back to a Maxwellian. The maximum action allowed on a field line, $\hat{I}(p_\theta)$, is determined from the initial and final z-integrated density profiles and the initial temperature.

$$N_0^f(p_\theta) = \int\limits_0^\infty 2\pi dI f_0^f(p_\theta, I) = \int\limits_0^{\hat{I}(p_\theta)} 2\pi dI f_0^i(p_\theta, I) = N_0^i(p_\theta)\mathrm{erf}\left[\frac{\hat{I}(p_\theta)}{\sqrt{2}\bar{I}(p_\theta)}\right] \tag{2.72}$$

The temperature and z-integrated density profiles can be measured experimentally and thus $\hat{I}(p_\theta)$ is known. Fig. 2.16 shows two z-integrated density profiles. The solid curve represents a likely initial profile before the ejection process (the actual initial profile for this experiment was not measured). The dashed curve represents the final, hollow profile which supports the diocotron instability.

Fig. 2.17 shows the corrections to the real frequency and the growth rate as the temperature increases. The solid lines represent the kinetic corrections for a plasma whose axial velocity distribution is a Maxwellian. In this case, the kinetic effects are insignificant. The dashed curves depict the corrections for a plasma with the truncated distribution defined by the profiles of Fig. 2.16. Here, the growth of the instability is greatly enhanced and the frequency is shifted down. In each case, the kinetic effects produced by the truncated distribution are substantially different than the non-kinetic results and the kinetic effects due to a Maxwellian distribution. This suggests that the instability cannot be completely understood in terms of density profiles alone.

Exact comparisons between the theory and experiments have not yet been made. The available experimental data on $\ell = 1$ diocotron instabilities does not include the initial z-integrated density profiles before hollowing. Furthermore, the hollowing processes have not been adiabatic and the final distribution of axial energies is not known. However, corrections have been calculated for various probable initial profiles and different distribution functions. The results indicate the hollowing process can substantially affect the instability.

2.9 Conclusion

We have developed a Zero Debye Length Reduced Description for a nonneutral plasma column confined in a Malmberg-Penning trap. The critical assumption of this model is that the rapid bounce motion along field lines produces axial Debye shielding for the equilibrium and the low frequency diocotron modes. Using this model, an eigenvalue equation for linear diocotron modes was obtained for a finite length plasma column. A Green function formulation was used and the eigenmodes were obtained from a matrix diagonalization of the discretized system of equations.

The solutions revealed the existence of many discrete modes in rigid rotor plasmas not found in the infinite length theory. It was also shown that these are absorbed into the continuum when shear in the plasma rotation velocity produces resonances with the modes. Discrete modes rotating faster than the plasma were observed in hollow end shape plasmas. It was further demonstrated that these modes are not destroyed by a small amount of shear and might be observable experimentally.

We have also found instabilities for hollow density profile columns and verified that finite length columns are exponentially unstable even for $\ell = 1$. Furthermore, we have shown that, in some cases, kinetic effects and the details of the axial velocity distribution function can have important consequences on the growth rate and real frequency of the unstable diocotron modes.

This chapter has been published in Physics of Plasmas **11**, T. J. Hilsabeck and T. M. O'Neil, 407-422 (2001). T. J. Hilsabeck was the primary investigator and author of this paper.

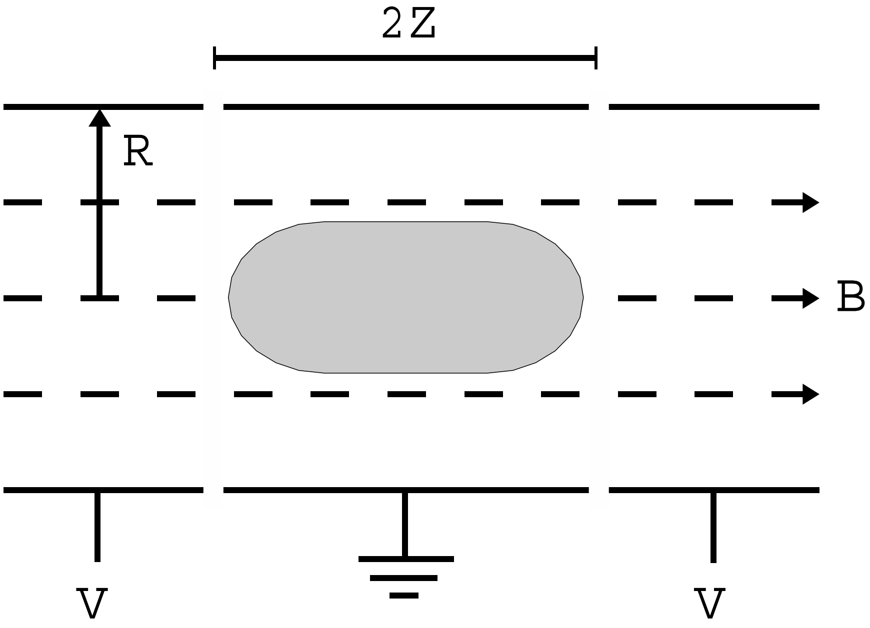

Figure 2.1: Malmberg-Penning confinement geometry. The end cylinders extend out to infinity.

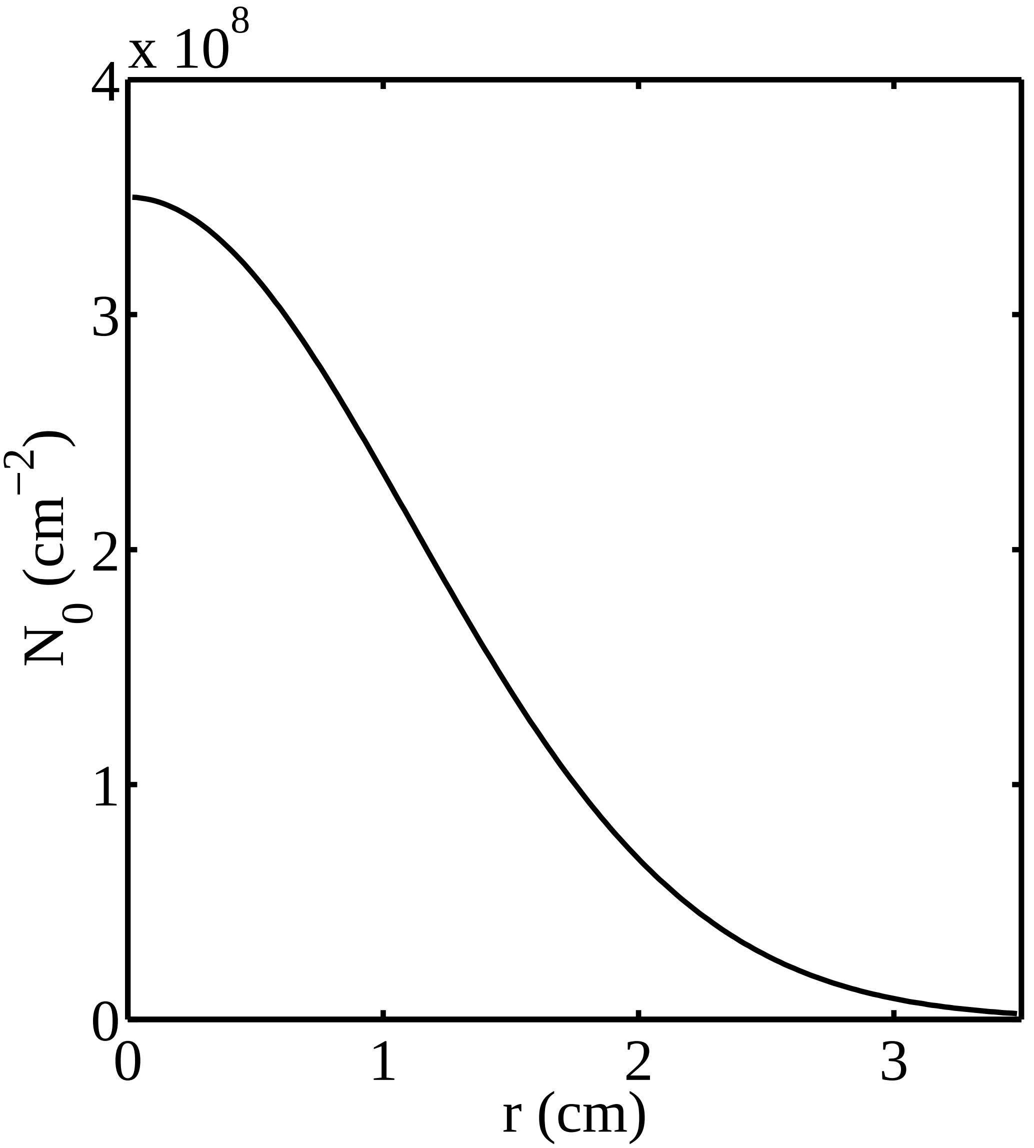

Figure 2.2: Gaussian z-integrated density profile.

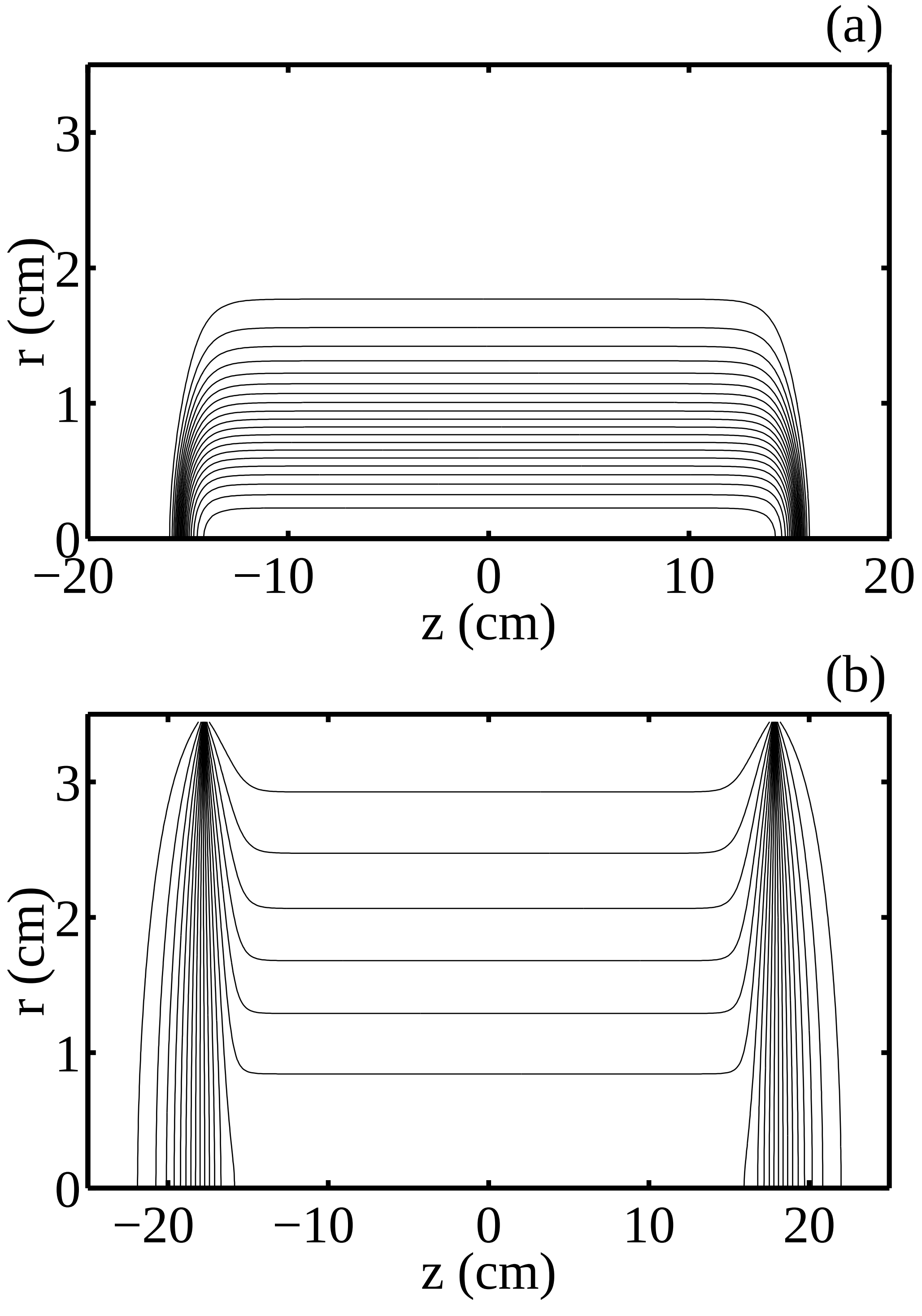

Figure 2.3: Poisson-Boltzmann solution for constant density (a) and potential (b) contours (R = 3.5 cm, Z = 17.3 cm, T = 1 eV).

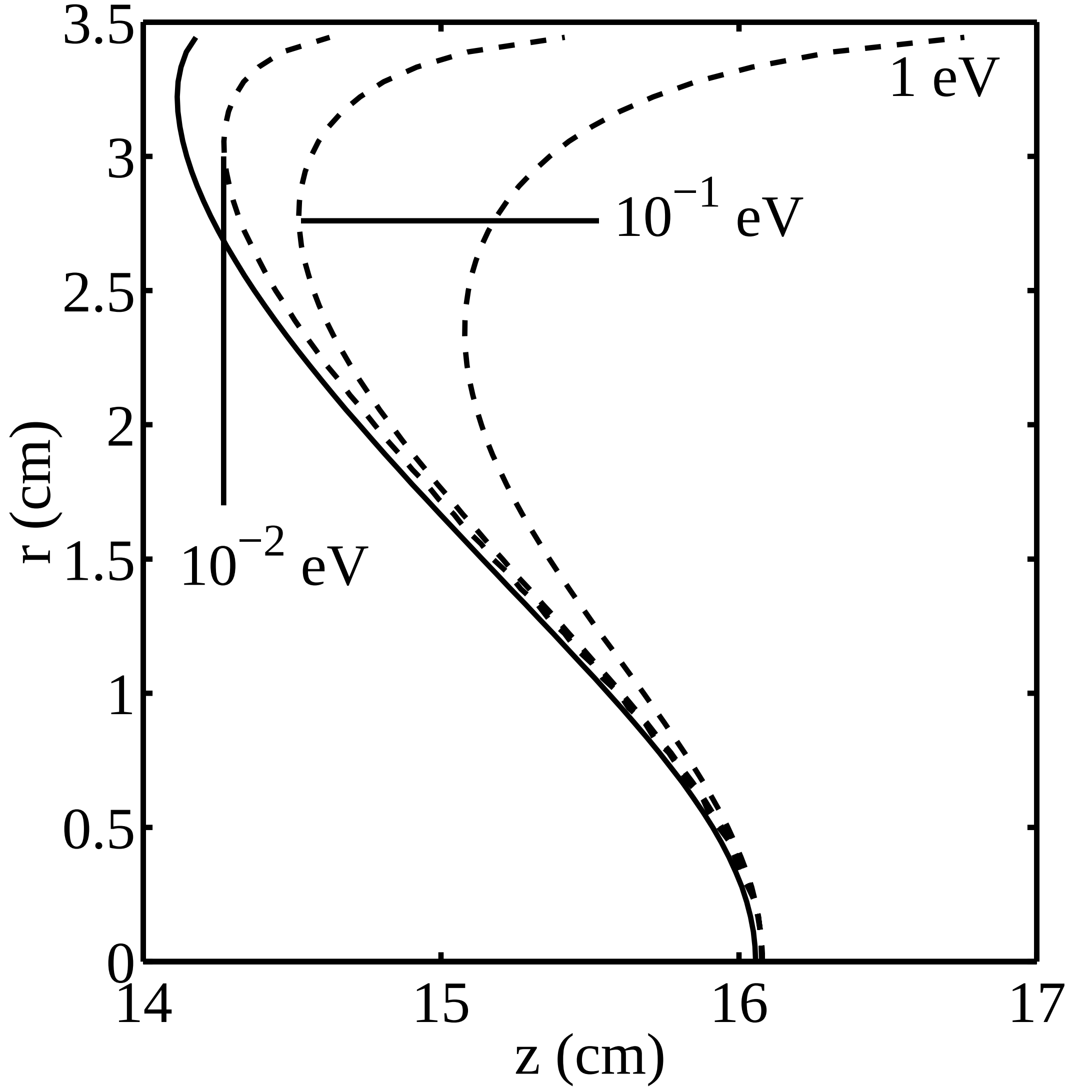

Figure 2.4: Equilibrium plasma lengths for Poisson-Boltzmann solutions (dashed). Equilibrium plasma length for the Zero Debye Length Reduced Description (solid).

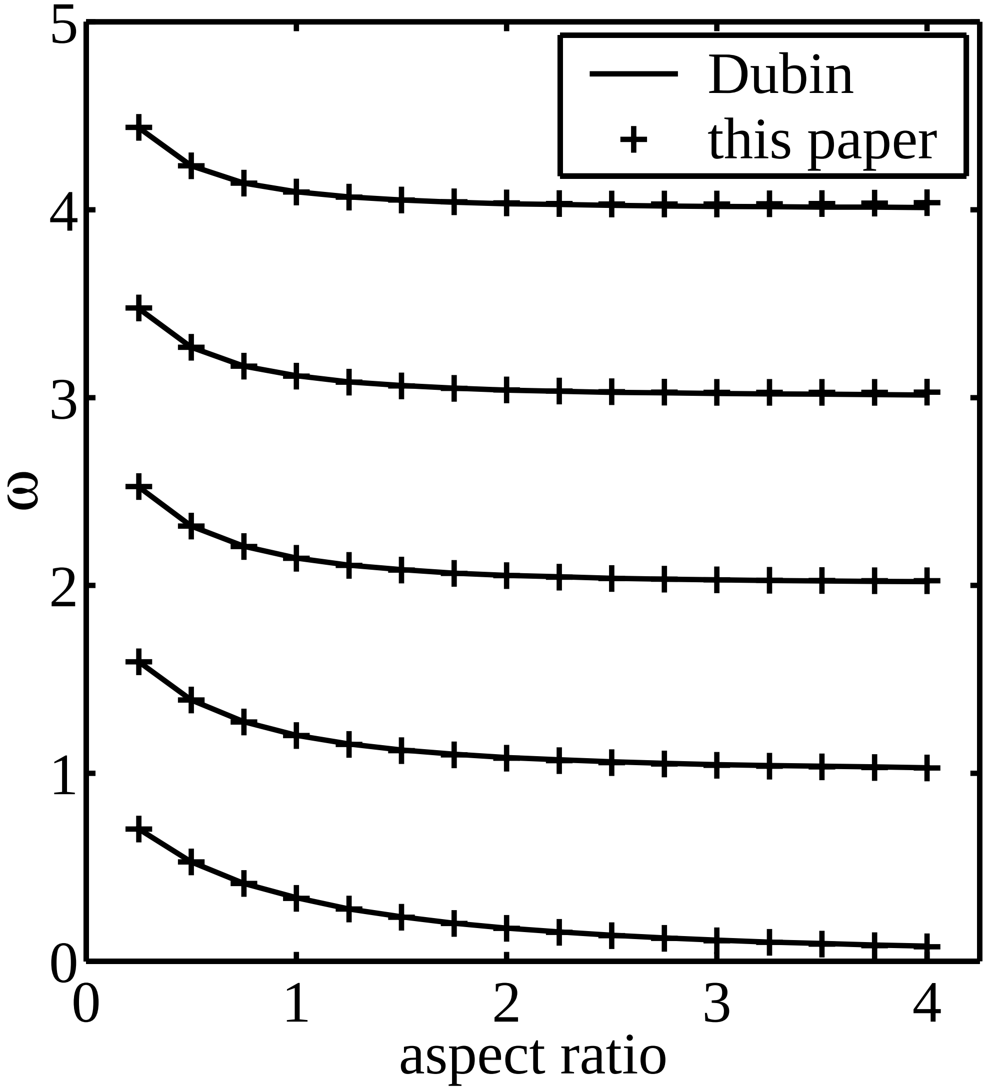

Figure 2.5: Comparison to Dubin's analytic theory of small ($r_p = R/10$) spheroids. Mode frequencies are given for the first five azimuthal wave numbers and are normalized to the rotation frequency.

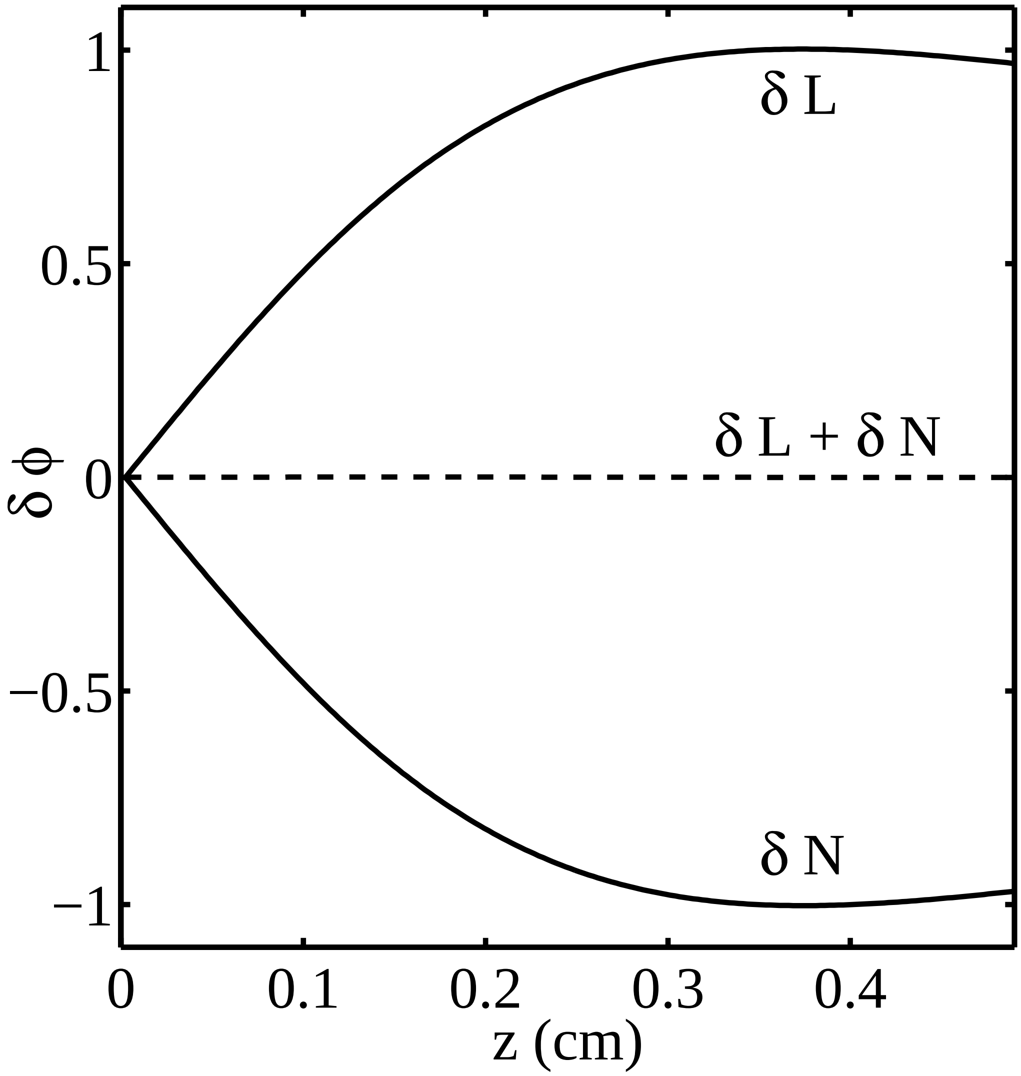

Figure 2.6: Mode potentials along axis ($r = r_p/6$) produced by δN and δL (note: their sum cancels as expected).

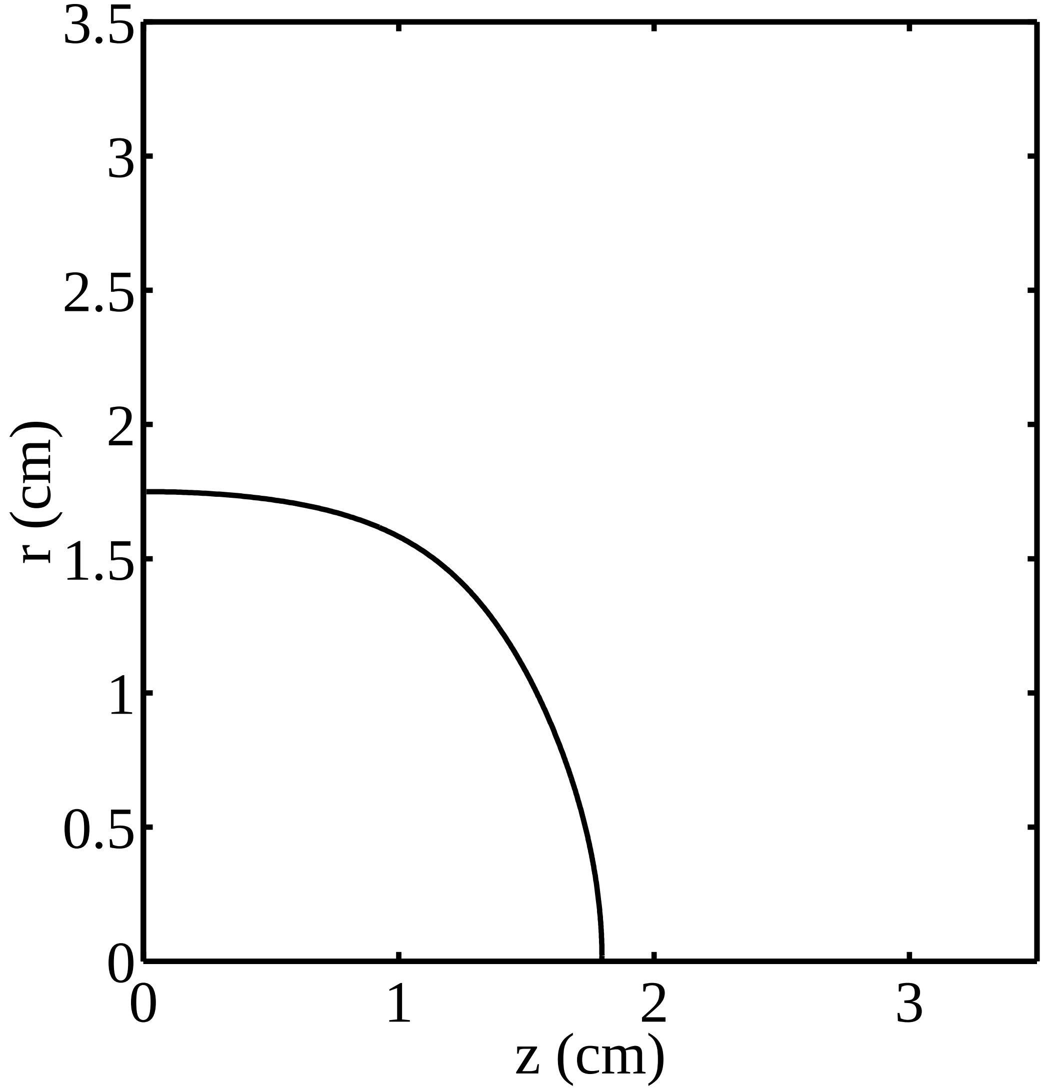

Figure 2.7: Equilibrium length function for a uniform density plasma. ($n_0 = 10^7$ cm^{-3}, $Z = R = 3.5$ cm, $V = 27$ Volts)

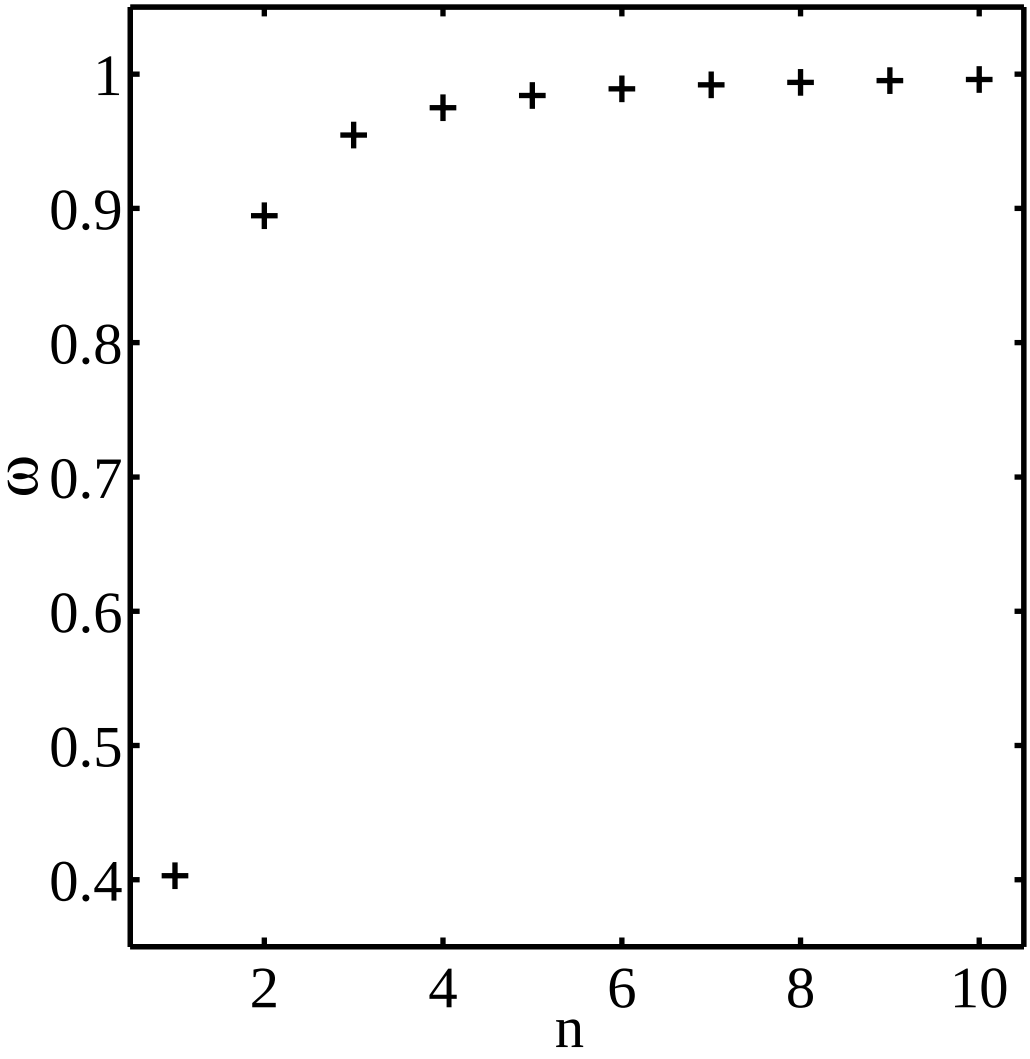

Figure 2.8: $\ell = 1$ eigenmode frequencies for plasma shown in Fig. 2.7 (indexed by a radial wave number n_r).

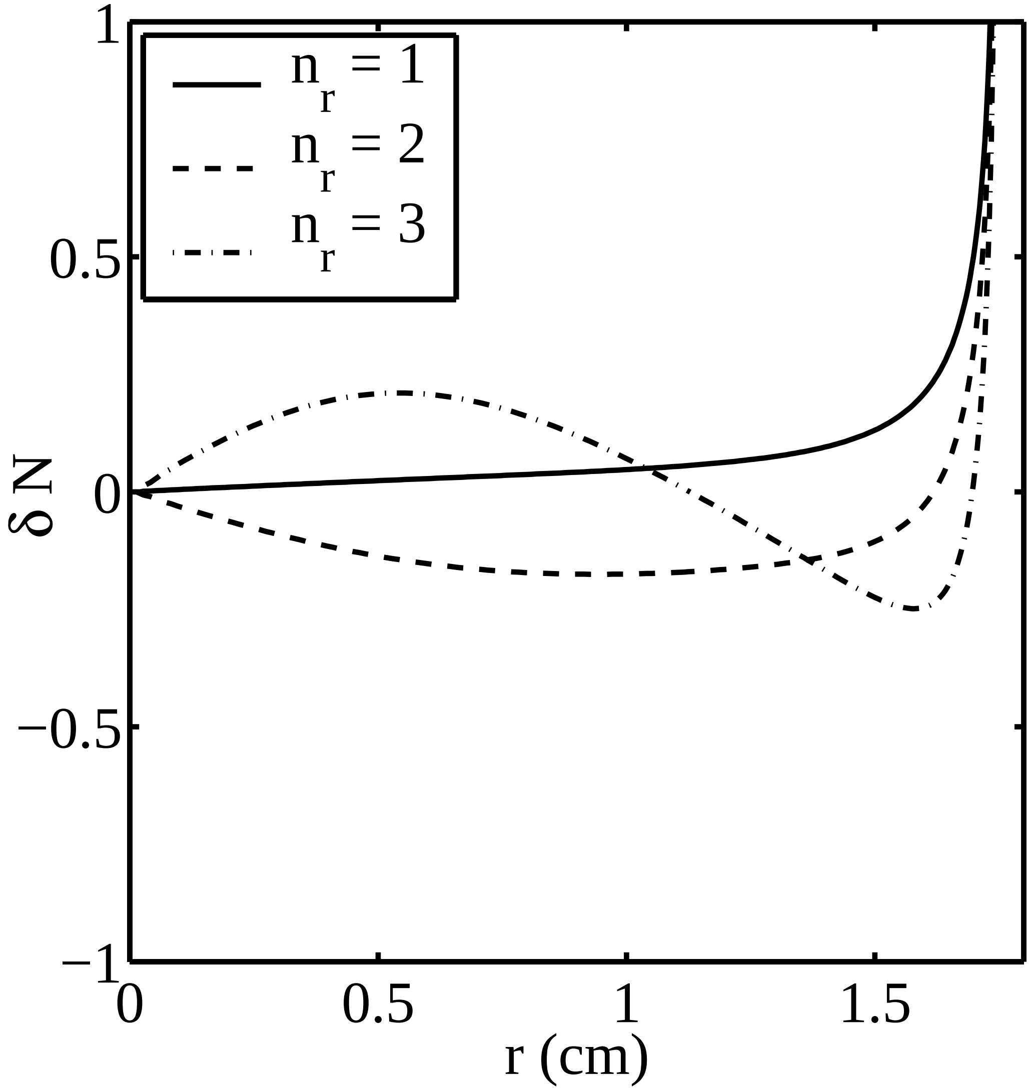

Figure 2.9: Z-integrated density perturbations of the first three radial eigenmodes in Fig. 2.8.

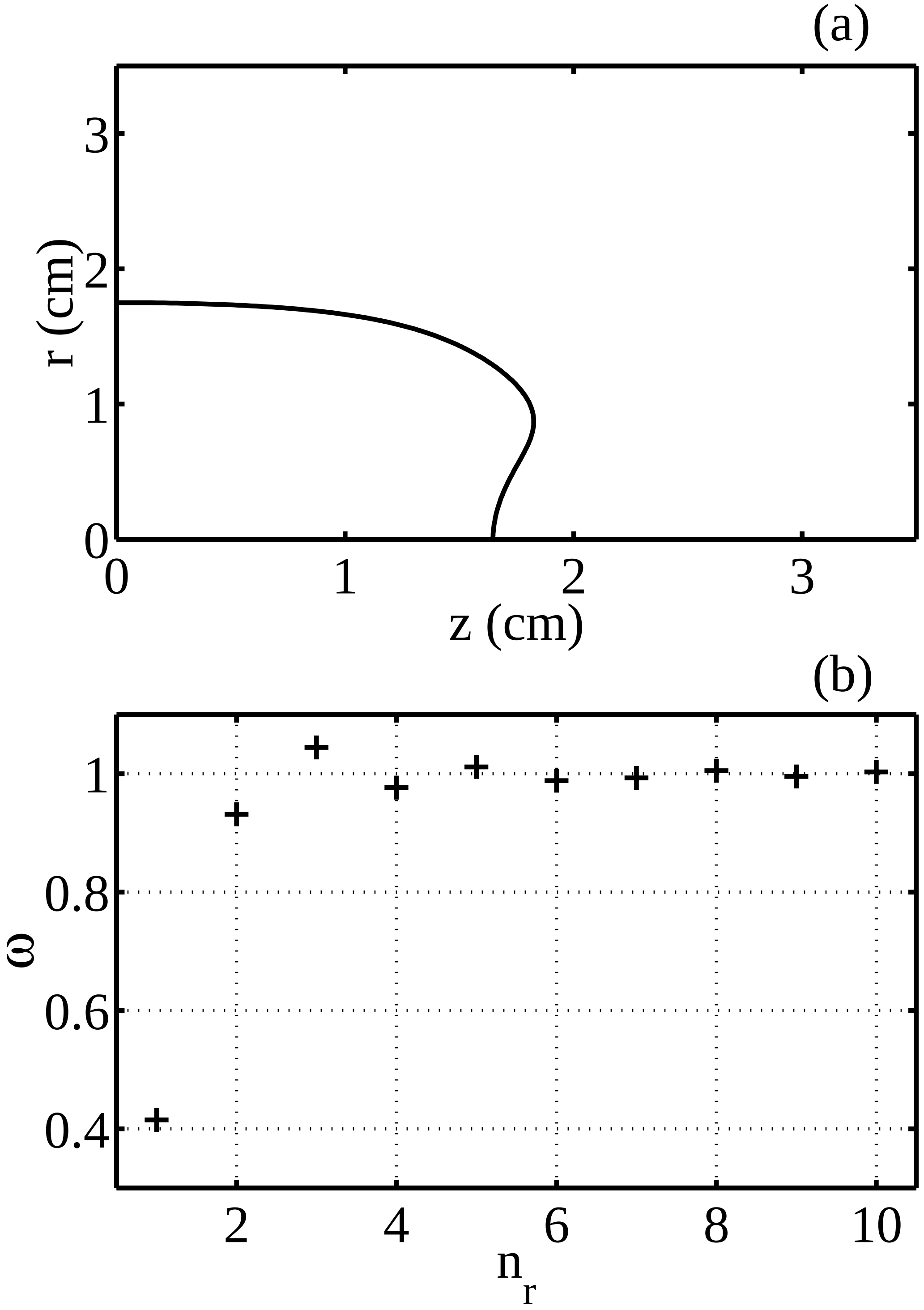

Figure 2.10: (a) Hollow equilibrium length function ($R = Z = 3.5$ cm, $V = 27$ Volts). (b) Eigenfrequencies for hollow end shape column.

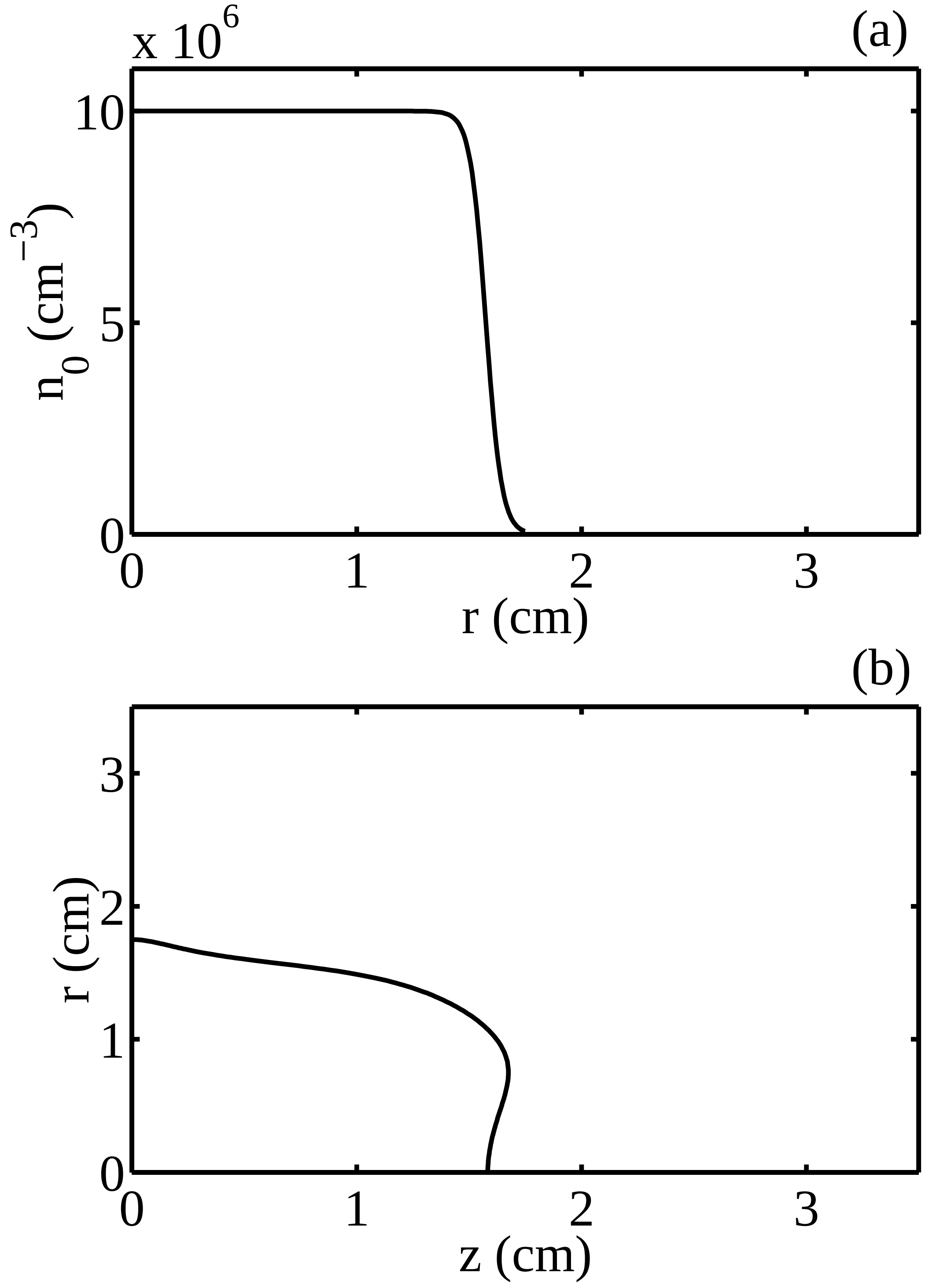

Figure 2.11: Smoothed local density profile and hollow equilibrium length function ($R = Z = 3.5$ cm, $V = 21$ Volts).

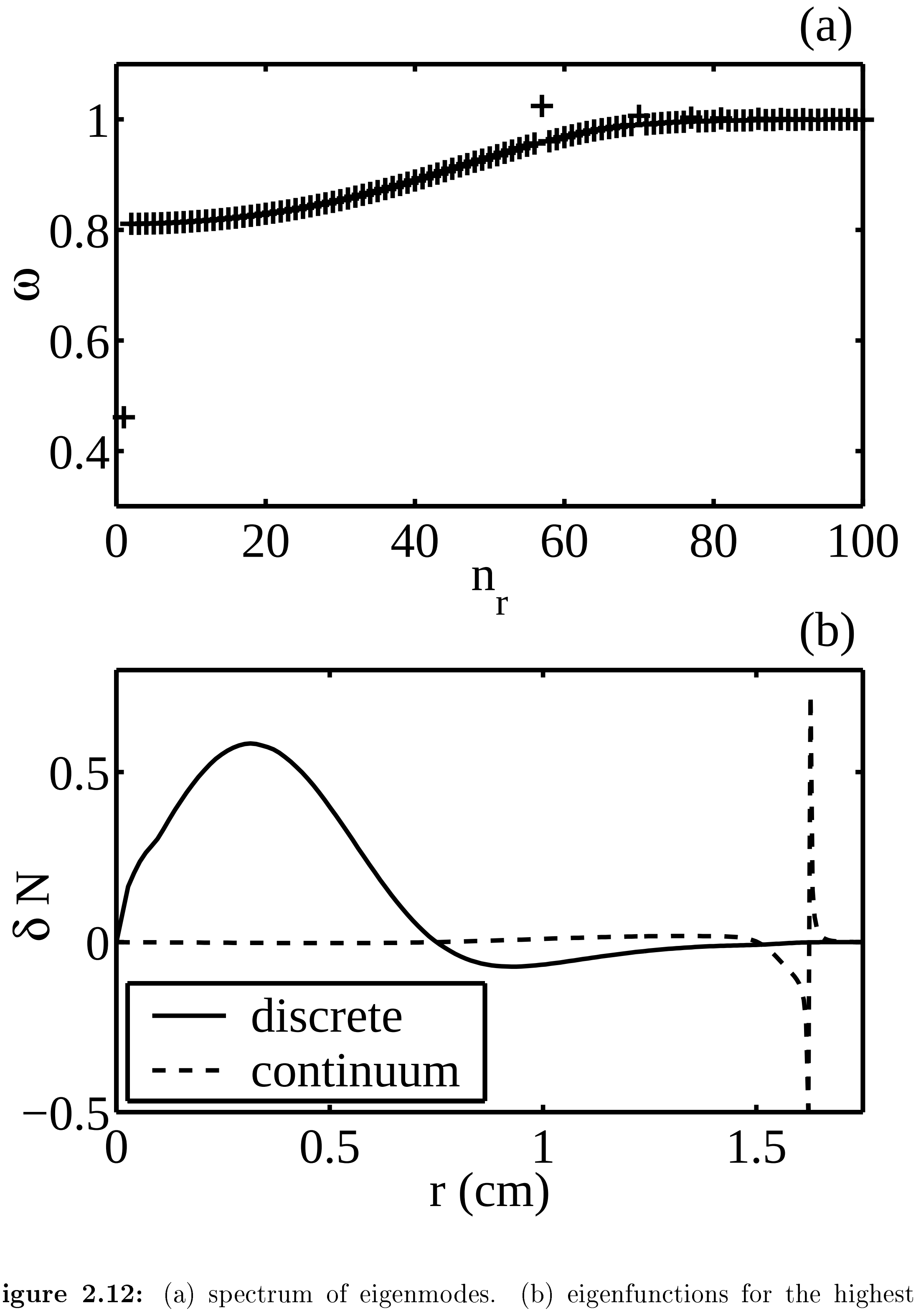

Figure 2.12: (a) spectrum of eigenmodes. (b) eigenfunctions for the highest frequency mode and a continuum mode.

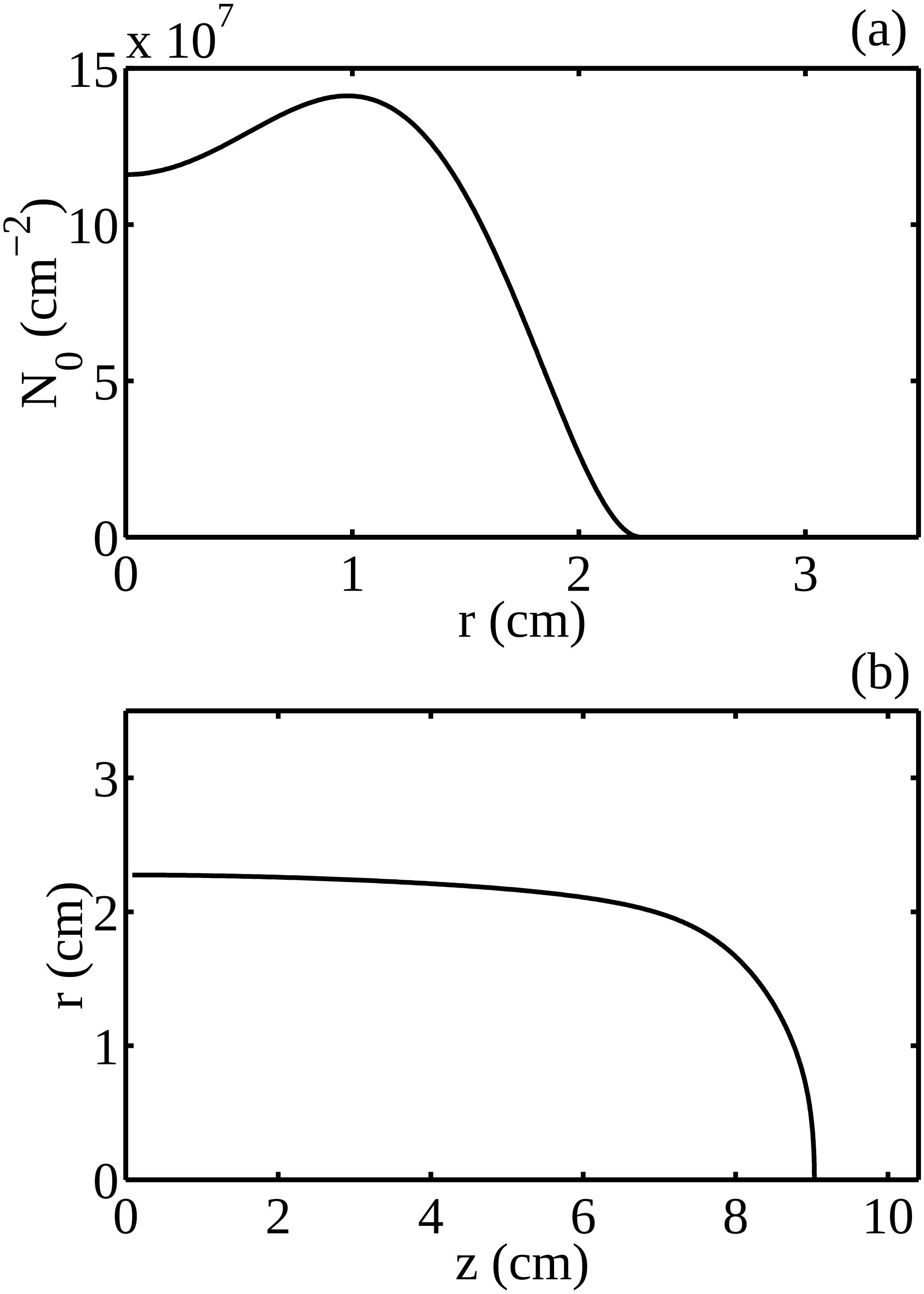

Figure 2.13: Hollow z-integrated density profile and calculated equilibrium length function ($R = 3.5$ cm, $Z = 10.4$ cm, $V = 60$ Volts).

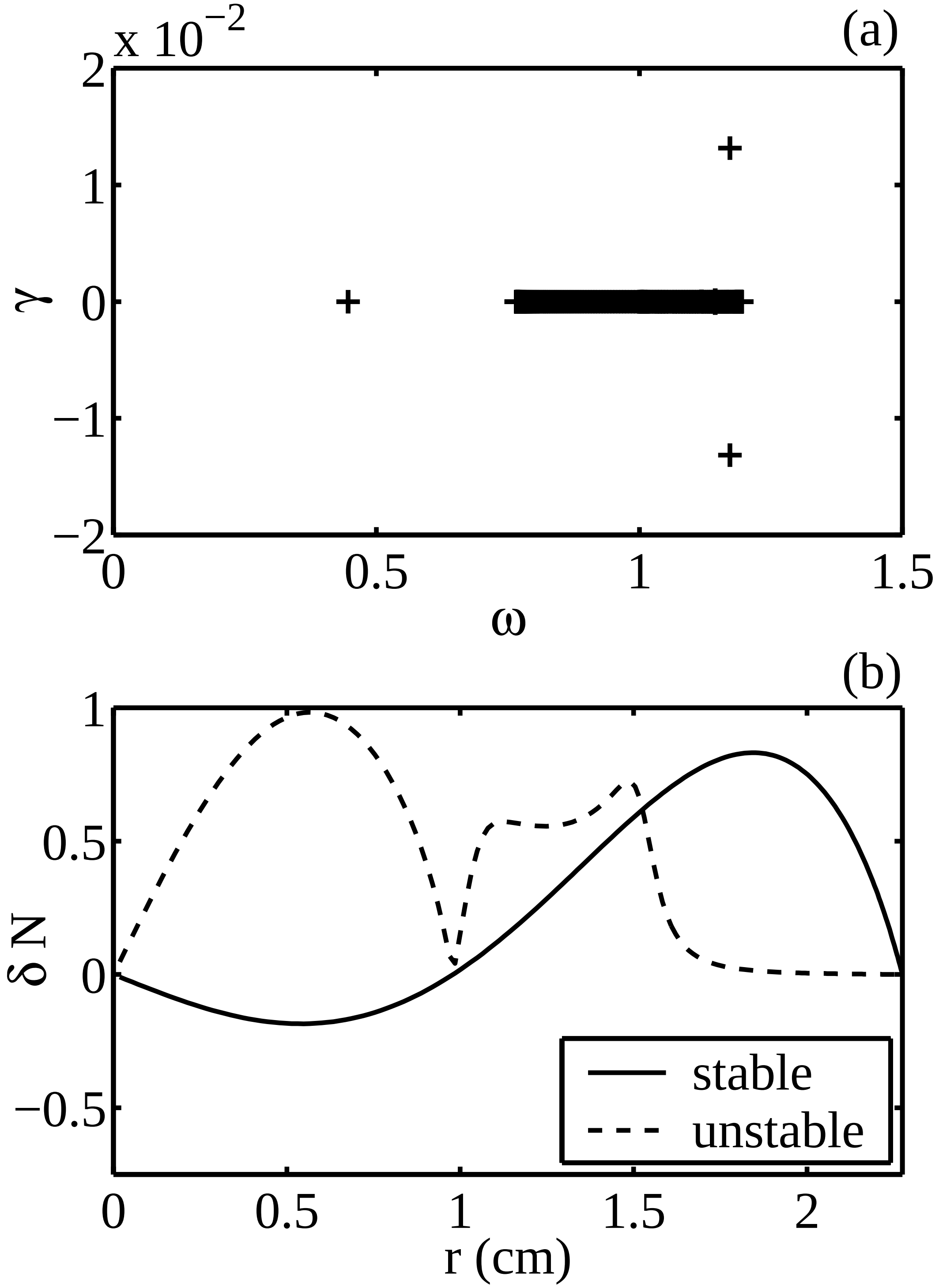

Figure 2.14: Spectrum of eigenmodes and eigenfunctions for stable and unstable modes (note: unstable mode eigenfunction shown is $|\delta N|$).

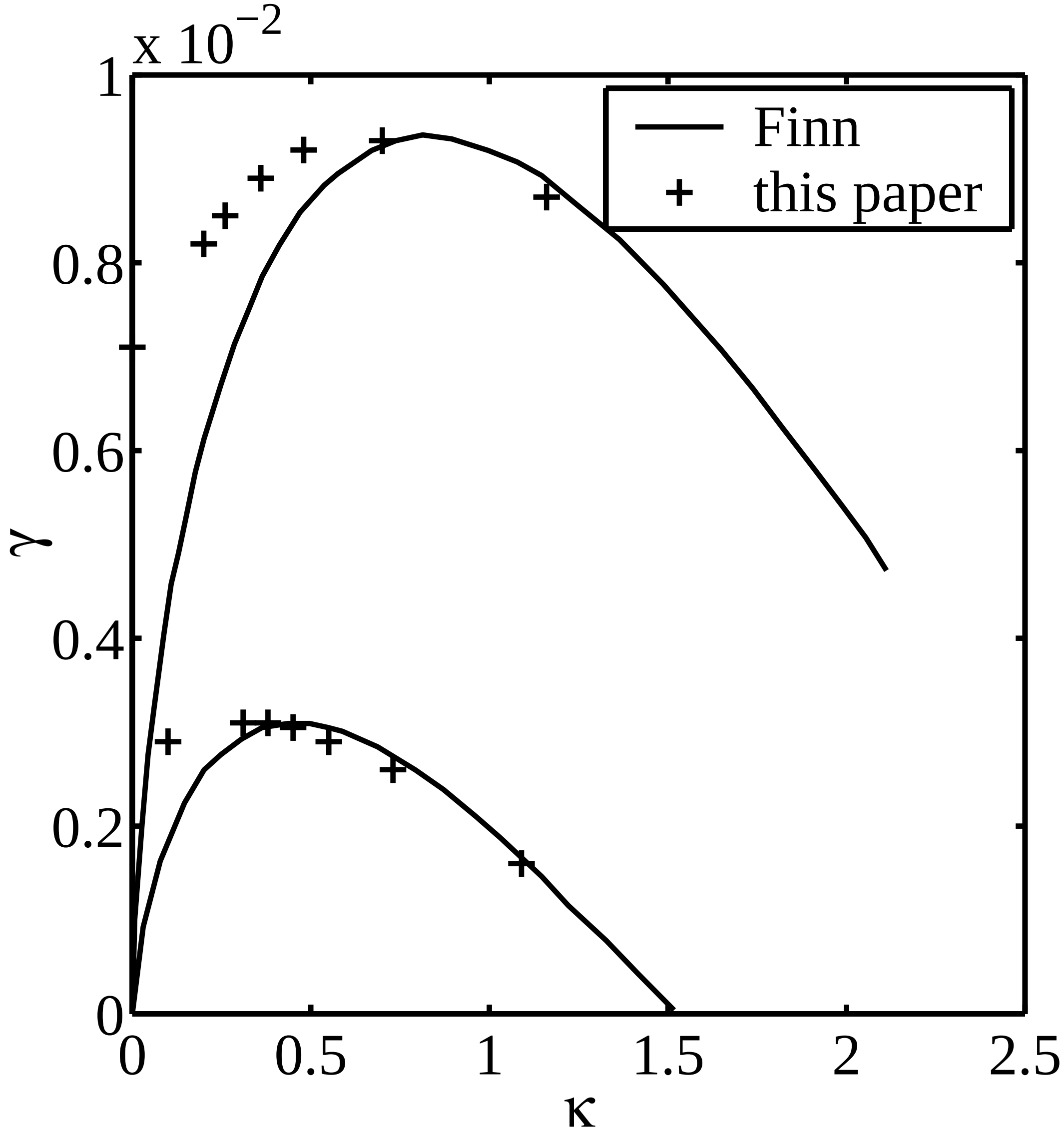

Figure 2.15: Growth rate vs. curvature comparison to the theory of Finn *et al.*[8]

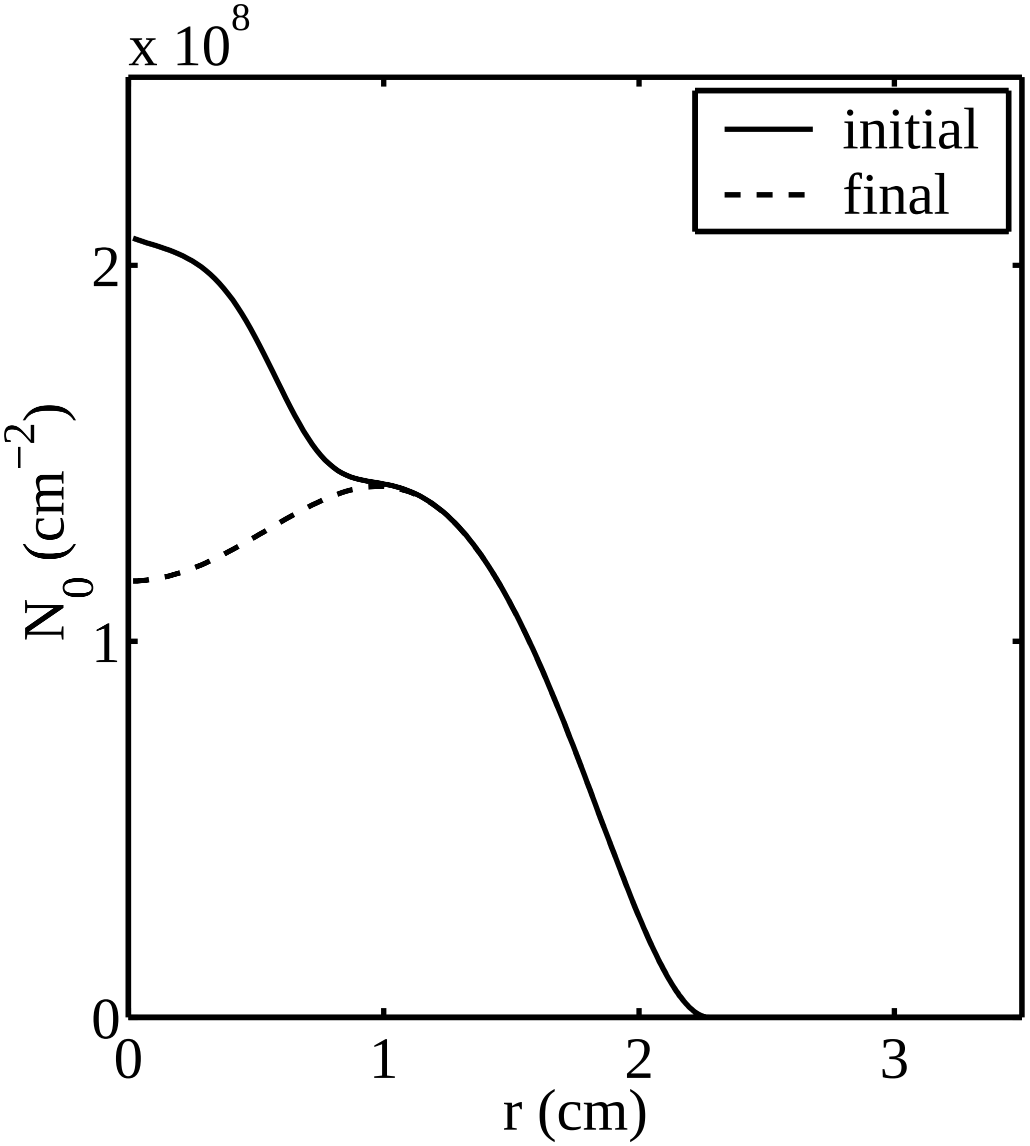

Figure 2.16: An initial z-integrated density profile and the hollow profile obtained after ejection.

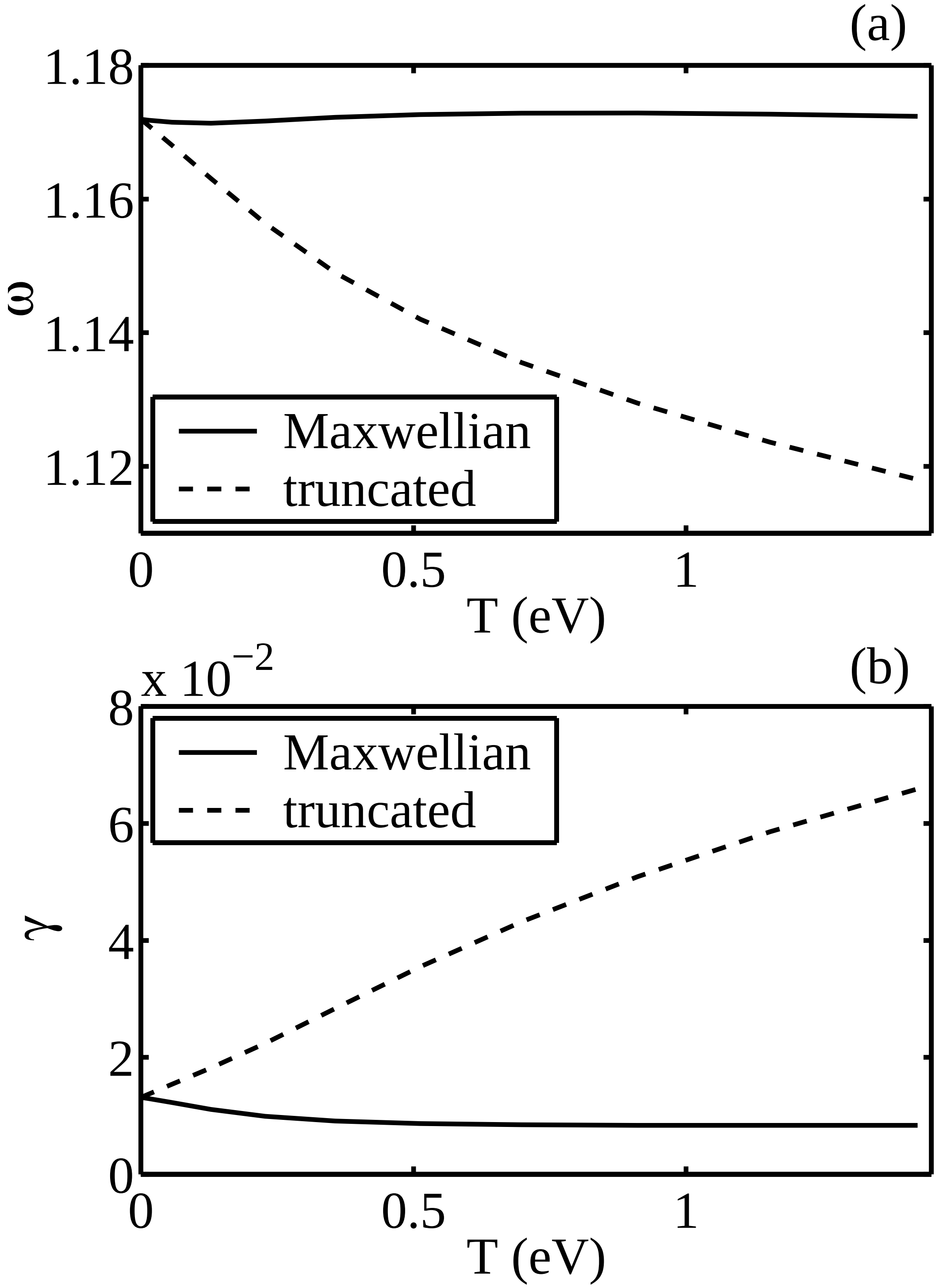

Figure 2.17: Effects of finite temperature on the $\ell = 1$ hollow profile instability [(a) real frequency, (b) growth rate] for a Maxwellian velocity distribution and the truncated distribution obtained from the profiles of Fig. 2.16.

Chapter 3

Trapped-Particle Diocotron Modes

3.1 Abstract

Recent experiments have characterized trapped-particle modes on a nonneutral plasma column[17], and this paper presents a theoretical model of the modes. Theoretical predictions for the mode frequency, damping rate, and eigenmode structure are compared to experimental observation. The modes are excited on a nonneutral plasma column in which classes of trapped and passing particles have been created by the application of a potential barrier. The column resides in a Malmberg-Penning trap, and the barrier is created by applying a voltage to an azimuthally symmetric section of the wall near the axial mid-point of the column. Low energy particles near the edge of the column (where the barrier is strong) are trapped in one end or the other, while high energy particles near the center of the column transit the entire length. The modes have azimuthal variation $\ell = 1, 2, ...$ and odd z-symmetry. The trapped particles on either side of the barrier execute $\mathbf{E} \times \mathbf{B}$ drift oscillations producing density perturbations that are 180° out of phase with each other, while passing particles run back and forth along the field lines attempting to Debye shield the perturbed charge density. The mode is

damped by collisional scattering across the separatrix between trapped and passing particles. The damping rate is calculated using a boundary layer analysis of the Fokker-Planck equation. It is also shown that the damping is associated with radial transport of plasma particles.

3.2 Introduction

Electric and magnetic field inhomogeneities in plasma containment devices cause a fraction of the particles to remain localized in certain regions. This condition gives rise to a class of low frequency electrostatic oscillations known as trapped-particle modes[36]. In these modes, trapped particles remain isolated from the global mode structure and experience $\mathbf{E} \times \mathbf{B}$ drift oscillations locally, while passing particles stream along the field lines Debye shielding the trapped-particle charge density perturbations. In this sense, trapped-particle modes resemble drift waves wherein the trapped particles play the role of ions and passing particles the role of electrons. Trapped-particle modes were originally investigated for toroidal geometry, but have been predicted for and observed in other geometries, such as the Columbia Linear Machine[26].

Recent experiments with magnetically confined nonneutral plasma columns have characterized a new trapped-particle mode: the trapped-particle diocotron mode[17]. This paper provides a theoretical description of the mode, and compares theoretical prediction to experimental measurement for the frequency, damping rate, and eigenmode structure. The agreement is good (for example, 10% percent for frequency and 50% percent for damping rate) over a substantial range of experimental parameters.

The modes are excited on a nonneutral (pure electron) plasma column to which an azimuthally symmetric potential barrier has been applied creating classes of trapped and passing particles. This electrostatic barrier, the squeeze voltage, is typically applied near the axial mid-point of the column. Particles with low axial velocity are then trapped in either end, while high axial velocity particles pass back and forth over the full length of the column.

The mode dynamics is easy to understand. Trapped particles in the two ends of the column undergo low frequency $\mathbf{E} \times \mathbf{B}$ drift oscillations that are 180° out of phase with each other, while passing particles move back and forth along the magnetic field lines Debye shielding the charge perturbation of the trapped particles.

The mode damping is due to collisional scattering of marginally trapped particles. Following the analysis of Rosenbluth, Ross, and Kostomarov[31] for the dissipative trapped-ion mode, we solve the Fokker-Planck equation in a thin boundary layer near the separatrix between trapped and passing particles, and find that the relative damping scales like $\sqrt{\nu/\omega}$, rather than ν/ω. Here, ν is the collision frequency, ω is the mode frequency, and the square root is important because ν/ω is small.

To understand why collisions have an enhanced effect near the separatrix, first note that the trapped and passing particles experience very different dynamics. In the absence of collisions, the perturbed velocity distributions for the trapped and passing particles would be discontinuous (in value and slope) at the separatrix. Small angle scattering, described by the Fokker-Planck collision operator, is essential in smoothing the discontinuity. Steep gradients in a narrow boundary layer enhance the effective collision frequency to the point where an order unity correction (the smoothing) is made to the perturbed velocity distribution.

Significantly, the correction contains a component that is in phase with the mode electric field, so the mode can exchange energy with the scattered particles.

The dominant energy exchange occurs because the mode transports the scattered particles radially outward. The liberated electrostatic energy increases the mode energy, and would cause growth of a positive energy mode. However, the observed trapped-particle diocotron mode has negative energy, so the mode damps.

A direct experimental test was made to verify that scattering of marginally trapped particles causes the damping. The scattering rate was enhanced artificially by applying a potential that oscillates in resonance with the axial bounce motion of marginally trapped particles. The damping rate was observed to increase an order of magnitude coincident with the application of this oscillation potential.

The remainder of the paper is organized as follows. Section 3.3 describes the confinement geometry and plasma equilibrium. Section 3.4 discusses the basic equations for the mode dynamics. Section 3.5 solves for the mode frequency and eigenmode structure in the absence of collisions. An analytic solution is possible in an idealized limit, but numerical solution is necessary for realistic density profile and potential barrier profile. In Section 3.6, the effect of collisions is included, and the damping rate is calculated. Section 3.7 discusses Landau resonances and argues that Landau (and bounce resonant) damping are typically small for these modes.

3.3 Confinement Geometry and Equilibrium

The pure electron plasma column is confined in a Malmberg-Penning trap configuration as shown schematically in Fig. 3.1. The confinement region is bounded radially by a series of conducting cylinders of radius R_w. The end cylinders are held at negative potential to provide axial confinement of the electron plasma, while radial confinement is provided by a large axial magnetic field $\mathbf{B} = B\hat{z}$. Here, (r, θ, z) is a cylindrical coordinate system with the z-axis coincident with the axis of the cylindrical wall. Because the column is unneutralized, there is a radial space charge electric field and consequent $\mathbf{E} \times \mathbf{B}$ drift rotation of the column.

A static, θ-symmetric barrier is created by applying a negative voltage (the "squeeze" potential) to a short cylindrical section of the bounding wall. The resulting barrier potential is an increasing function of radius, with more particles trapped near the radial edge of the plasma than near the trap axis. At any given radius, the squeeze potential presents an insurmountable barrier to low axial velocity particles, trapping them in the end regions. Particles with high axial velocity pass over the squeeze potential and sample the entire length of the column.

In the experiments, the plasma has time to come into thermal equilibrium along each field line before the mode is launched. Thus, the equilibrium distribution function is given by

$$f_0(r, z, v) = \frac{N(r)\exp\{-\frac{1}{T}[mv^2/2 - e\phi_0(r,z)]\}}{\int dz \int dv \exp\{-\frac{1}{T}[mv^2/2 - e\phi_0(r,z)]\}}, \tag{3.1}$$

where v is the z-component of the velocity. The transverse velocity components have been integrated out, anticipating that drift dynamics will be used in the description of the mode. The z-integrated density $N(r)$ and the temperature on axis [i.e., $T(r = 0)$] are known from measurement. The temperature is assumed to be independent of r for simplicity and for want of better knowledge. The possibility of introducing error here will be discussed later (see Section 3.6). The self-consistent equilibrium potential $\phi_0(r, z)$ is obtained by substituting the charge density $-en_0(r, z) = -e\int dv f_0(r, z, v)$ into Poisson's equation and numerically solving subject to the known boundary conditions for the potential on the trap wall.

In Fig. 3.2, equilibrium density and potential contours are shown for a typical case. The z-integrated density profile, $N(r)$, is monotonically decreasing with a peak of 8.2 10^8 cm^{-2} on axis. The plasma temperature in this example is 1 eV and the end ring potentials are 100 Volts. A 20 Volt squeeze potential is applied over a central conducting ring of length 7 cm. The radial wall of the trap is located at 3.5 cm. The equilibrium solution in Fig. 3.2 demonstrates the effectiveness of the Debye shielding in forcing the potential and density to be z-independent, except in the squeeze region and near the ends of the column. This condition holds generally for the plasmas under consideration in this paper.

Fig. 3.3 shows phase space orbits executed by particles moving along a particular magnetic field line (at $r = 0.5$ cm) in the equilibrium of Fig. 3.2. All of the particles are reflected by the large confinement fields at the ends. Particles whose maximum axial velocity is less than the separatrix velocity ($0.68\bar{v}$ for this field line) are reflected by the squeeze barrier and are trapped in the ends. Orbits for the trapped particles are shown as dashed curves. Particles with high axial energy pass through the squeeze region and sample the entire length of the column during a bounce orbit. The passing particle orbits are shown as the solid curves in Fig. 3.3.

The separatrix velocity is determined indirectly from the experimental measurements. The electric potential inside the trap is obtained using the Poisson-Boltzmann solution described above. Debye shielding produces a potential that is axially uniform inside the plasma on either side of the squeeze region. In the squeeze region, the potential varies smoothly and reaches a maximum at $z = 0$. The energy barrier seen by a particle bouncing at a radius r is determined by the difference in potential between the region of smooth potential (say, $z = \pm 15$ cm) and the center of the squeeze region ($z = 0$ cm). Particles with a maximum kinetic energy that matches this potential energy barrier are moving at the separatrix velocity

$$v_s(r) = \left\{ \frac{2e}{m} \left[\phi_0(r, 15) - \phi_0(r, 0) \right] \right\}^{\frac{1}{2}} . \tag{3.2}$$

Because the barrier potential is strongest nearest the trap wall, the separatrix velocity is an increasing function of radius.

The density profiles of trapped and passing particles at any given radius can be determined from the total particle density profile $n_0(r)$ and the separatrix velocity $v_s(r)$. The density of particles trapped by the squeeze barrier at a particular radius is

$$n_t(r) = \int_{-v_s(r)}^{v_s(r)} dv f_0(r,v) = n_0(r)\ \mathrm{erf}\left[\frac{v_s(r)}{\sqrt{2}\bar{v}}\right], \tag{3.3}$$

and the passing density is $n_p(r) = n_0(r) - n_t(r)$. Figure 3.4 shows the trapped, passing and total density profiles for the equilibrium of Fig. 3.2, and clearly demonstrates the radial dependence of the fraction of trapped particles.

The Debye shielding of the squeeze potential results in a barrier that is a strong function of radius. Most particles near the edge of the plasma are trapped and most particles near the trap axis are passing. Radial localization of trapping is a general feature of externally applied electrostatic squeeze potentials.

3.4 Dynamical Equations

Because the cyclotron frequency is the largest of the relevant dynamical frequencies and the cyclotron radius is the smallest of the length scales, the mode dynamics can be described by the drift kinetic equation

$$\left(\frac{\partial}{\partial t} + v\frac{\partial}{\partial z} - \frac{c}{Br}\frac{\partial \phi}{\partial \theta}\frac{\partial}{\partial r} + \frac{c}{Br}\frac{\partial \phi}{\partial r}\frac{\partial}{\partial \theta} + \frac{e}{m}\frac{\partial \phi}{\partial z}\frac{\partial}{\partial v}\right) f = C(f), \tag{3.4}$$

where $f = f(r,\theta,z,v,t)$ is the distribution of guiding centers and $\phi(r,\theta,z,t)$ is the electric potential. Of course, $\phi(r,\theta,z,t)$ is determined by $f(r,\theta,z,v,t)$ through Poisson's equation and the known boundary conditions for ϕ on the wall. On the right hand side, $C(f)$ is the Fokker-Planck collision operator integrated over the velocity components transverse to $\mathbf{B} = B\hat{z}$[30].

Although equilibrium distribution (3.1) was written down using thermal equilibrium considerations, not surprisingly it is a time independent solution of Eq. (3.4). This follows from the fact that $C(f_0) = 0$, $\partial\phi_0/\partial\theta = \partial f_0/\partial\theta = 0$, and $v\partial f_0/\partial z + (e/m)(\partial\phi_0/\partial z)(\partial f_0/\partial z) = 0$.

We take the mode perturbation to be small and linearize Eq. (3.4) in $\delta f = f - f_0$ and $\delta\phi = \phi - \phi_0$. The result is

$$\left(\frac{\partial}{\partial t} + v\frac{\partial}{\partial z} + \omega_E\frac{\partial}{\partial\theta} + \frac{e}{m}\frac{\partial\phi_0}{\partial z}\frac{\partial}{\partial v} - C\right)\delta f = -\frac{e}{m}\frac{\partial f_0}{\partial v}\frac{\partial\delta\phi}{\partial z} + \frac{c}{Br}\frac{\partial f_0}{\partial r}\frac{\partial\delta\phi}{\partial\theta}, \quad (3.5)$$

where $\omega_E = (c/Br)(\partial\phi_0/\partial r)$ is the $\mathbf{E} \times \mathbf{B}$ drift rotation frequency for the equilibrium. Since f_0 and ϕ_0 are independent of θ and t, we consider perturbations of the form

$$(\delta f, \delta\phi) = (\delta f_\ell, \delta\phi_\ell)\exp(i\ell\theta - i\omega t), \quad (3.6)$$

Eq. (3.5) then reduces to the form

$$\left(-i\omega + i\ell\omega_E + v\frac{\partial}{\partial z} + \frac{e}{m}\frac{\partial\phi_0}{\partial z}\frac{\partial}{\partial v} - C\right)\delta f_\ell = -\frac{e}{m}\frac{\partial\delta\phi_\ell}{\partial z}\frac{\partial f_0}{\partial v} + \frac{ic\ell}{Br}\frac{\partial f_0}{\partial r}\delta\phi_\ell. \quad (3.7)$$

The left hand side of Eq. (3.7) includes the term $C(\delta f_\ell)$, which is the linearization of the Fokker-Planck collision operator with respect to the perturbation δf_ℓ. The linearization includes four terms

$$C(\delta f_\ell) = \frac{\partial}{\partial v}\left[D(v)\frac{\partial\delta f_\ell}{\partial v} + F(v)\delta f_\ell\right] + \frac{\partial}{\partial v}\left[\delta D(v)\frac{\partial f_0}{\partial v} + \delta F(v) f_0\right], \quad (3.8)$$

where $D(v)$ and $F(v)$ are the parallel diffusion and drag coefficients evaluated for the equilibrium distribution f_0, and $\delta D(v)$ and $\delta F(v)$ are the diffusion and drag coefficients evaluated for the perturbed distribution δf_ℓ. For future reference, note that any perturbation of the form $\delta h_\ell = g(r,z)f_0$ is such that $C(\delta h_\ell) = 0$. Also, note that near the separatrix, where derivatives of δf_ℓ are very large, only the highest derivative term in $C(\delta f_\ell)$ need be retained. In the separatrix boundary layer, Eq. (3.8) may be approximated by

$$C(\delta f_\ell) \simeq D(v_s)\frac{\partial^2 \delta f_\ell}{\partial v^2}. \tag{3.9}$$

The parallel diffusion coefficient is of order $D \sim \nu\bar{v}^2$, but more accurately is given by

$$D(v_s) = \boxed{16}\rightarrow\frac{\cancel{8}\sqrt{\pi}e^4 nT\Lambda}{m^3 v_s^3}\int_0^{\frac{mv_s^2}{2T}} \sqrt{t}\, e^{-t}dt, \tag{3.10}$$

where $\Lambda = \ln(r_c/b)$ is the Coulomb logarithm for the case where $e^2/T \equiv b \ll r_c \ll \lambda_D$[25].

The justification of the linearization is subtle and requires some discussion. As mentioned, we will find that the mode damping is dominated by particles in a thin boundary layer near the separatrix. However, a nonlinear effect of the mode potential shifts the velocity of the separatrix up and down by an amount $\delta v_{nl} \sim e\delta\phi/mv_s$ every cycle. Particles in this band undergo a complicated sequence of trapping and detrapping transitions that is missed by the linearized equation (3.7). Why then is the linearization valid, and what is the criterion for validity?

The essential point is that small angle scattering, which is included in Eq. (3.7), causes rapid trapping and detrapping transitions over a broader velocity band than δv_{nl}. The effective collision frequency for scattering over the velocity interval δv_s is $\nu_{eff} = D(v_s)/(\delta v_s)^2$, where $D(v_s)$ is the parallel diffusion coefficient discussed above. One can understand this relation as the statement that velocity diffusion extends over the range δv_s during the time ν_{eff}^{-1} [i.e., $(\delta v_s)^2 = D\ \nu_{eff}^{-1}$]. For the scattering transitions across the separatrix to be at least as fast as the nonlinearity induced transitions we set $\nu_{eff} = \omega' \equiv |\omega - \ell\omega_E|$, the Doppler shifted mode frequency as seen by a particle. This yields the collision dominated width $\delta v_s = \sqrt{D/\omega'} \simeq \bar{v}\sqrt{\nu/\omega'}$, where the approximation $D \simeq \nu\bar{v}^2$ has been used. In section 3.6, we will find that this is the width of the boundary layer that dominates mode damping. Thus, the criterion for validity of the linearization is the inequality $\delta v_s \gg \delta v_{nl}$, which can be written as $\sqrt{\nu/\omega'} \gg e\delta\phi/T$, where we have set $v_s \simeq \sqrt{T/m}$.

3.5 Frequency and Eigenmode

In this section, we solve for the mode frequency and eigenmode structure. Both are described adequately by collisionless theory. The effect of weak collisions will be included in the next section, which discusses the mode damping.

The solution relies on the frequency ordering $\omega_b \gg \omega_E, \omega$, where $\omega_b = \pi\bar{v}/L$ is the characteristic axial bounce frequency for electrons and $L = L_1 + \Delta + L_2$ is the overall column length (see Fig. 3.1). Since ω and ω_E both scale like $1/B$, an expansion in the small parameter $\omega/\omega_b \sim \omega_E/\omega_b \ll 1$ is equivalently an expansion in $1/B$.

In zero order, Eq. (3.7) reduces to

$$\left(v\frac{\partial}{\partial z} + \frac{e}{m}\frac{\partial\phi_0}{\partial z}\frac{\partial}{\partial v}\right)\delta f_\ell = \frac{e}{T}v\frac{\partial\delta\phi_\ell}{\partial z}f_0 \tag{3.11}$$

where $C(\delta f_\ell)$ has been neglected and use has been made of $\partial f_0/\partial v = -(mv/T)f_0$ on the right hand side. Eq. (3.11) can be rewritten as

$$\left(v\frac{\partial}{\partial z} + \frac{e}{m}\frac{\partial\phi_0}{\partial z}\frac{\partial}{\partial v}\right)\left(\delta f_\ell - \frac{e\delta\phi_\ell}{T}f_0\right) = 0, \tag{3.12}$$

which is a statement that the quantity $[\delta f_\ell - (e\delta\phi_\ell/T)f_0]$ is constant along a bounce orbit. Thus, we may equate the value of this quantity to its bounce-average value, obtaining the result

$$\delta f_\ell = \langle\delta f_\ell\rangle + \frac{e}{T}[\delta\phi_\ell - \langle\delta\phi_\ell\rangle]f_0. \tag{3.13}$$

Here, the bracket indicates a bounce-average,

$$\langle g\rangle(r,\theta,\epsilon) = \frac{\oint \frac{dz}{v(z,\epsilon)} g[r,\theta,z,v(z,\epsilon)]}{\oint \frac{dz}{v(z,\epsilon)}}, \tag{3.14}$$

where $mv^2/2 - e\phi_0(r,z) = \epsilon$ specifies the orbit. In writing Eq. (3.13), use was made of the fact that f_0 is constant along an orbit.

To obtain an equation for $\langle \delta f_\ell \rangle$, we bounce-average Eq. (3.7) projecting out the zero order terms. The remaining (first order) terms describe cross magnetic field drift motion

$$-i\omega\langle \delta f_\ell \rangle + i\ell\langle \omega_E \delta f_\ell \rangle = \frac{ic\ell}{Br}\langle \delta\phi_\ell \frac{\partial f_0}{\partial r}\rangle. \tag{3.15}$$

The second term on the right hand side of Eq. (3.13) specifies the distribution of electrons along a bounce orbit. This type of response, called an adiabatic response, gives rise to Debye shielding. Thus, we anticipate here, and verify a posteriori (see Section 3.7), that Debye shielding forces the mode potential to be z-independent, except in the region of the squeeze potential and near the ends of the column.

As a simple model that captures the essential physics, we use a step function approximation for the mode potential

$$\delta\phi_\ell(r,z) = \begin{cases} \delta\phi_{\ell 1}(r) & 0 < z < L_1 \\ \delta\phi_{\ell 2}(r) & L_2 < z < 0 \end{cases}, \tag{3.16}$$

where L_1 and L_2 are the lengths of the two trapped-particle regions (see Fig. 3.1). Likewise, we neglect the small but finite axial extent of the squeeze region and ends when evaluating the bounce averages. The model assumes that the trapped-particle regions are long compared to the squeeze region and ends. The advantage of the model is that a partial differential eigenmode equation for $\delta\phi_\ell(r,z)$ is reduced to two coupled ordinary differential equations for $\delta\phi_{\ell 1}$ and $\delta\phi_{\ell 2}$. We will see that a simple physically motivated guess as to the ratio $\delta\phi_{\ell 1}/\delta\phi_{\ell 2}$ decouples these equations leaving a single ODE eigenmode equation.

The step function model simplifies the evaluation of bounce-averages. For trapped particles on side j ($j = 1$ or 2), the bounce-average mode potential is given by $\langle\delta\phi_\ell\rangle = \delta\phi_{\ell j}$, and for passing particles it is given by

$$\langle\delta\phi_\ell\rangle = \frac{L_1\delta\phi_{\ell 1} + L_2\delta\phi_{\ell 2}}{L_1 + L_2}. \tag{3.17}$$

Since the squeeze region and ends are neglected, the bounce-average products in Eq. (3.15) simplify: $\langle\omega_E\delta f_\ell\rangle = \omega_E\langle\delta f_\ell\rangle$ and $\langle\delta\phi_\ell\partial f_0/\partial r\rangle = \langle\delta\phi_\ell\rangle\partial f_0/\partial r$.

Eqs. (3.13) and (3.15) then imply that the perturbed distribution for trapped particles on the side j is given by

$$\delta f_{\ell j}^{(t)} = \frac{c\ell}{Br}\frac{\delta\phi_{\ell j}}{\omega'}\frac{\partial f_0}{\partial r}, \tag{3.18}$$

where $\omega'(r) \equiv \ell\omega_E(r) - \omega$. Likewise, the perturbed distribution for passing particles on side j is given by

$$\delta f_{\ell j}^{(p)} = \frac{c\ell}{Br}\frac{\langle\delta\phi_\ell\rangle}{\omega'}\frac{\partial f_0}{\partial r} + \frac{e}{T}[\delta\phi_{\ell j} - \langle\delta\phi_\ell\rangle]f_0, \tag{3.19}$$

where $\langle\delta\phi_\ell\rangle$ is given by Eq. (3.17).

The next step is to determine the density perturbations associated with trapped and with passing particles. Because the separatrix velocity is a function of radius [i.e, $v_s = v_s(r)$], one must be careful not to miscount particles. First consider the trapped particles. Eq. (3.18) can be understood as implying that each trapped particle undergoes a radial step $\delta r_{\ell j} = -c\ell\delta\phi_{\ell j}/Br\omega'$, so that

$$\delta f_{\ell j}^{(t)}(r,v) = f^{(t)}(r - \delta r_{\ell j}, v) - f^{(t)}(r,v) = \frac{c\ell\delta\phi_{\ell j}}{Br\omega'}\frac{\partial f^{(t)}}{\partial r}. \tag{3.20}$$

Thus, the perturbation in the trapped-particle charge density is given by

$$\delta n_{\ell j}^{(t)}(r,v) = \int_{-v_s(r-\delta r_{\ell j})}^{-v_s(r-\delta r_{\ell j})} dv\, f^{(t)}(r - \delta r_{\ell j}, v) - \int_{-v_s(r)}^{-v_s(r)} dv\, f^{(t)}(r,v), \tag{3.21}$$

which for small $\delta r_{\ell j}$ takes the form

$$\delta n_{\ell j}^{(t)}(r,v) = \int_{-v_s(r)}^{-v_s(r)} dv\, \delta f_{\ell j}^{(t)}(r,v) + 2\frac{\partial v_s}{\partial r}\delta r_{\ell j} f^{(t)}(r,v). \tag{3.22}$$

Omission of the second term would miscount the number of trapped particles. Combining the two terms in Eq. (3.22) yields the result

$$\delta n_{\ell j}^{(t)} = \frac{c\ell}{Br}\frac{\delta\phi_{\ell j}}{\omega'}\frac{\partial n_t}{\partial r}, \tag{3.23}$$

where $n_t(r)$ is defined in Eq. (3.3). Of course, this result can be obtained more directly using a fluid theory for the trapped particles. Similar arguments for the passing particles yield the perturbed density

$$\delta n_{\ell j}^{(p)} = \frac{c\ell}{Br}\frac{\langle\delta\phi_\ell\rangle}{\omega'}\frac{\partial n_p}{\partial r} + \frac{e}{T}\left[\delta\phi_{\ell j} - \langle\delta\phi_\ell\rangle\right] n_p, \tag{3.24}$$

where $n_p(r) = 2\int_{v_s(r)}^{\infty} dv f_0(r,v)$.

Substituting density perturbations (3.23) and (3.24) into Poisson's equation yields two coupled differential equations,

$$\frac{1}{r}\frac{\partial}{\partial r}\left(r\frac{\partial}{\partial r}\delta\phi_{\ell j}\right) - \frac{\ell^2}{r^2}\delta\phi_{\ell j} = \frac{4\pi ec\ell}{Br}\frac{\delta\phi_{\ell j}}{\omega'}\frac{\partial n_t}{\partial r} + \frac{4\pi ec\ell}{Br}\frac{\langle\delta\phi_\ell\rangle}{\omega'}\frac{\partial n_p}{\partial r} + \frac{4\pi e^2 n_p}{T}\left[\delta\phi_{\ell j} - \langle\delta\phi_\ell\rangle\right]. \tag{3.25}$$

for $\delta\phi_{\ell j}$ ($j = 1$ and 2). Two ratios of $\delta\phi_{\ell 1}(r)/\delta\phi_{\ell 2}(r)$ for which the equations decouple are easy to guess. For the choice $\delta\phi_{\ell 1}(r) = \delta\phi_{\ell 2}(r) = \langle\delta\phi\rangle$, the two equations each reduce to the usual eigenmode equation for a diocotron mode

$$\frac{1}{r}\frac{\partial}{\partial r}\left(r\frac{\partial}{\partial r}\delta\phi_{\ell j}\right) - \frac{\ell^2}{r^2}\delta\phi_{\ell j} = \frac{4\pi ec\ell}{Br}\frac{\delta\phi_{\ell j}}{\omega'}\frac{\partial n_0}{\partial r}, \tag{3.26}$$

where $n_0(r) = n_t(r) + n_p(r)$. In this case, two in-phase diocotron modes exist on the two sides of the barrier.

For the choice $L_1\delta\phi_{\ell 1} = -L_2\delta\phi_{\ell 2}$, Eq. (3.17) implies that $\langle\delta\phi_\ell\rangle = 0$ so the two equations each reduce to the form

$$\frac{1}{r}\frac{\partial}{\partial r}\left(r\frac{\partial}{\partial r}\delta\phi_{\ell j}\right) - \frac{\ell^2}{r^2}\delta\phi_{\ell j} = \frac{4\pi ec\ell}{Br}\frac{\delta\phi_{\ell j}}{\omega'}\frac{\partial n_t}{\partial r} + \frac{4\pi e^2 n_p}{T}\delta\phi_{\ell j}. \tag{3.27}$$

This is the eigenmode equation for the trapped-particle diocotron mode (or more precisely, modes). From the right hand side, one can see that trapped particles undergo $\mathbf{E} \times \mathbf{B}$ drift motion locally and passing particles stream along field lines attempting to Debye shield the perturbed charge density of the trapped particles. The condition $L_1\delta\phi_{\ell 1} = -L_2\delta\phi_{\ell 2}$ guarantees that the passing particle charge needed for shielding on one side of the barrier is exactly liberated on the other side. The equations must be solved subject to the boundary conditions $\delta\phi_{\ell j}(0) = \delta\phi_{\ell j}(R_w) = 0$.

An analytic solution of Eq. (3.27) can be obtained in a particularly simple case. For very small Debye lengths, shielding of the squeeze potential effectively separates the trapped and passing particles radially. In this regime, the plasma may be described by a simplified model in which trapped and passing particles are divided by a separatrix radius, R_s. The trapped and passing particle densities can be written as $n_t(r) = n_0(r)\Theta(r - R_s)$ and $n_p(r) = n_0(r)\Theta(R_s - r)$, where $\Theta(x)$ is the Heaviside step function. For a top hat density profile, $n_0(r) = n_0\Theta(R_p - r)$, an analytic solution of Eq. (3.27) is possible.

The potential perturbation is composed of separate solutions in three regions. In region I ($r < R_s$), the mode potential satisfies the Debye shielding equation

$$\frac{1}{r}\frac{\partial}{\partial r}\left(r\frac{\partial}{\partial r}\delta\phi_\ell^I\right) - \frac{\ell^2}{r^2}\delta\phi_\ell^I - \frac{1}{\lambda_D^2}\delta\phi_\ell^I = 0, \tag{3.28}$$

where $\lambda_D^2 = T/4\pi e^2 n_0$. Since the potential cannot diverge at the origin, we obtain $\delta\phi_\ell^I(r) = I_\ell(r/\lambda_D)$, where I_ℓ is a modified Bessel function of the first kind. In regions II ($R_s < r < R_p$) and III ($r > R_p$), the mode potential satisfies the Laplace equation

$$\frac{1}{r}\frac{\partial}{\partial r}\left(r\frac{\partial}{\partial r}\delta\phi_\ell\right) - \frac{\ell^2}{r^2}\delta\phi_\ell = 0, \tag{3.29}$$

so we find $\delta\phi_\ell^{II}(r) = A_\ell r^\ell + B_\ell r^{-\ell}$ and $\delta\phi_\ell^{III}(r) = C_\ell(r^\ell - R_w^{2\ell}/r^\ell)$, where use has been made of the boundary condition $\delta\phi_\ell^{III}(R_w) = 0$. Eq. (3.27) also must be satisfied at the interfaces $r = R_s$ and $r = R_p$, where $\partial n_t/\partial r$ gives delta function contributions. This requires that the potential be continuous at the interfaces,

$\delta\phi^{I}_{\ell}(R_s) = \delta\phi^{II}_{\ell}(R_s)$ and $\delta\phi^{II}_{\ell}(R_p) = \delta\phi^{III}_{\ell}(R_p)$, and that the derivatives satisfy the jump conditions

$$r\frac{\partial}{\partial r}\delta\phi_\ell|^{R_s^+}_{R_s^-} = \frac{2\ell}{\omega^*}\delta\phi_\ell(R_s) \tag{3.30}$$

and

$$r\frac{\partial}{\partial r}\delta\phi_\ell|^{R_p^+}_{R_p^-} = -\frac{2\ell}{\omega^*}\delta\phi_\ell(R_p), \tag{3.31}$$

where $\omega^* = \ell - \omega/\omega_E$[5]. Eliminating the unknown coefficients A, B, C yields the dispersion relation

$$\begin{aligned}&\left(\frac{R_p}{R_s}\right)^\ell \left(\frac{I_\ell}{\omega^*} + \frac{R_s I_{\ell-1}}{2\ell\lambda_D}\right)\left(\frac{R_w^{2\ell}}{R_p^{2\ell} - R_w^{2\ell}} + \frac{1}{\omega^*}\right)\\ &-\left(\frac{R_s}{R_p}\right)^\ell \left(\frac{I_\ell}{\omega^*} + \frac{R_s I_{\ell+1}}{2\ell\lambda_D}\right)\left(\frac{R_p^{2\ell}}{R_p^{2\ell} - R_w^{2\ell}} + \frac{1}{\omega^*}\right) = 0,\end{aligned} \tag{3.32}$$

where $I_\ell \equiv I_\ell(R_s/\lambda_D)$.

There are two roots for Eq. (3.32) with one above and one below the rotation frequency. The fast mode has a frequency very near to the rotation frequency of the column and has not yet been observed in the experiments. For appreciable squeeze voltage, the lower root lies well below the column rotation frequency and corresponds to the experimentally observed mode. The existence of two modes is due to the positive and negative slope of the trapped density profile. This situation is analogous to the inner and outer diocotron modes that exist for hollow profiles[5]. In the trapped-particle case, the inner (faster) mode is not unstable, since the rotation frequency is monotonically decreasing.

As $\lambda_D \to 0$, the dispersion relation reduces to

$$\omega^* = \frac{R_w^{2\ell} - R_p^{2\ell}}{R_w^{2\ell} - R_s^{2\ell}}\frac{R_p^{2\ell} - R_s^{2\ell}}{R_p^{2\ell}}. \tag{3.33}$$

This is the low frequency mode. The high frequency mode has vanished. In this limit, the passing particles behave like a conducting cylinder of radius R_s. This suggests that trapped-particle diocotron modes may exist in a trap with a central conducting cylinder containing two plasma columns that are completely separated axially by a strong squeeze. In that case, the damping mechanism discussed in section 3.6 would be absent. Eq. (3.33) provides some quick insight into the qualitative behavior of the low frequency trapped-particle diocotron mode. For low squeeze potentials, R_s approaches the plasma radius and the azimuthal phase velocity of the wave approaches the rotation frequency of the column. At the opposite extreme, the separatrix radius approaches zero and the frequency becomes that of the usual diocotron mode

$$\omega = \omega_E \left[\ell - 1 + \left(\frac{R_p}{R_w} \right)^{2\ell} \right]. \tag{3.34}$$

This result is expected since the column has been completely divided and the two halves are effectively decoupled in our reduced description that ignores space charge interactions of the two columns. As we will see, this frequency dependence on squeeze voltage is observed experimentally.

For a careful comparison to experiment, we use the shooting method to obtain a numerical solution of Eq. (3.27) for realistic density profiles. Input to the theory are the magnetic field strength, voltages on the end rings and barrier electrode, z-integrated density $N(r)$, and temperature $T \equiv T(r=0)$. From these quantities, the equilibrium trapped particle density $n_t(r)$, and separatrix velocity $v_s(r)$ are determined, as discussed in section 3.3, and Eq. (3.27) is then solved to find ω. Fig. 3.5 shows a comparison of the numerically measured frequency as a function of squeeze voltage for the temperature $T(r=0) = 0.5$ eV and magnetic field $B = 10$ kG. The azimuthal mode number is $\ell = 1$. The agreement is very good (10%), with both curves following the trend expected from the analytic solution. From Eq. (3.27), one can see trivially that the mode frequency is predicted to scale with magnetic field strength as $\omega \propto 1/B$. This scaling is observed experimentally to an accuracy of 2% over the range 300 G to 10 kG[16]. Although the temperature enters Eq. (3.27) explicitly and implicitly [e.g., through $n_t(r)$, $n_p(r)$ and $v_s(r)$] the solutions for ω exhibit only a weak dependence on temperature, changing less than 5% as the temperature is varied by an order of magnitude. Measurements also show only a weak dependence; ω varies by 5% as T varies over $0.5 - 5.0$ eV.

The density perturbation of the trapped-particle mode vanishes at a specific radius. Inside this radius, the majority of particles involved in the oscillation are passing and move adiabatically along field lines. Outside this radius, the particles are mostly trapped and experience drift motion. Eigenfunctions at low and high squeeze voltages are shown in Fig. 3.6. The zero crossing (π phase change) of the density perturbation decreases as the squeeze voltage is increased. This is expected since the stronger barrier traps more particles.

There is qualitative agreement but small systematic discrepancy in the measured and observed eigenfunctions. At low squeeze voltage, the theoretical model predicts a smaller passing particle perturbation than is observed in the experiment. At high squeeze voltage, the model predicts a larger perturbation in the passing particles than is observed. The origin of this discrepancy remains unclear. The discrepancy in δn for $r > 1.5$ cm is due to a truncation of the density profile. The experimentally measured density profiles exhibit a small tail out at large radii. It is unknown whether this tail is real or some artifact of the measurement process. To avoid singularities in Eq. (3.27) caused by a wave-fluid resonance, we have smoothly truncated the experimentally measured density profile (at $r = 1.5$ cm) for use in the calculation.

The mode potentials for plasmas at various temperatures (0.1, 0.5, 1.0, 5.0 eV) are shown in Fig. 3.7. The Debye shielding phenomenon resulting from the adiabatic motion of the passing particles is readily observed. As the temperature is decreased, the potential created by the trapped particle density perturbation remains essentially unchanged. However, the passing particles shield this potential from the interior of the column at very low temperatures.

As mentioned earlier, Eq. (3.32) predicts the existence of another trapped-particle mode that has an azimuthal phase velocity above the column rotation frequency. With this in mind, we return to the full kinetic model and look for numerical solutions of Eq. (3.27) for $\omega > \ell\omega_E(0)$. In fact, we have found several eigenmodes in this high frequency range. Figure 3.8 shows plots of eigenmode potentials for three such trapped-particle modes. In this case, the plasma was characterized by the density profiles in Fig. 3.4, a magnetic field of 10 kG, and a temperature of 1 eV. The potential perturbations are indexed by the number of radial nodes, n_r. As the radial nodes increase the azimuthal phase velocity of the waves asymptotes to the rotation frequency at the axis $[\omega_E(r = 0)]$. For $n_r = 0$, the phase velocity is 10% above the peak plasma rotation frequency and the electric field at the trap wall is 0.44% that of the lower branch mode. A small radial electric field at the wall is a feature common to all of the high frequency modes. This makes them extremely difficult to observe experimentally. Typically, diocotron modes are launched and detected by applying time varying voltages to the wall sectors. The coupling of these self-shielded modes to the wall sectors is very weak. However, if the modes are excited by some other means, the density eigenfunctions can be observed by dumping the plasma.

In Fig. 3.9, the trapped and passing density perturbations are shown for the low frequency and $n_r = 1$ high frequency modes. For the low frequency mode, the main perturbation of trapped particles occurs at outer radii, and the passing perturbation is at inner radii. In this situation, the potential is effectively shielded from the column interior. In the high frequency oscillation, the main trapped and passing particle perturbations occur at inner radii. However, the trapped-particle perturbation is larger and a substantial mode potential exists at inner radii (see Fig. 3.8).

3.6 Collisions

In this section, we return to the discussion of the low frequency trapped-particle diocotron mode and investigate the effects of collisions between particles. Because the trapped particles and the passing particles experience different dynamics, the mode perturbation in the velocity distribution is discontinuous in collisionless theory. Setting $\langle \delta\phi_\ell \rangle = 0$ in Eqs. (3.18) and (3.19) yields

$$\delta f_{\ell j}(r,v) = \begin{cases} \frac{e\delta\phi_{\ell j}}{T} f_0(r,v) & |v| > v_s(r) \\ \frac{c\ell}{Br}\frac{\delta\phi_{\ell j}}{\omega'}\frac{\partial f_0(r,v)}{\partial r} & |v| < v_s(r) \end{cases}, \tag{3.35}$$

where we have used $f^{(t)}(r,v) = f_0(r,v)$ for $|v| < v_s(r)$ and $f^{(p)}(r,v) = f_0(r,v)$ for $|v| > v_s(r)$. This expression for $\delta f_\ell(r,v)$ is discontinuous in value and slope at $v = v_s(r)$. When collisions are added to the theory, the Fokker-Planck collision operator contains velocity derivatives that become arbitrarily large at such a discontinuity, so the effect of collisions on δf_ℓ cannot be ignored even if ν is small. Small angle scattering provides an essential correction, smoothing the distribution in a boundary layer near the separatrix. In Fig. 3.10, the perturbed distribution function at a specific radius is plotted versus velocity. The solid line represents $\delta f_{\ell j}$ from collisionless theory and clearly depicts the discontinuity at the separatrix velocity. The dashed line is the real part of the collisional correction to $\delta f_{\ell j}$ which removes the discontinuity. We will derive this correction shortly. Significantly, the correction contains an imaginary component (dot-dashed line) that is in phase with the mode electric field, so the mode can exchange energy with the scattered particles and damp as a consequence. We will show that the velocity scattering and damping are intrinsically associated with a kind of neo-classical radial transport.

Including the effect of collisions, the trapped-particle perturbation satisfies the equation

$$\left\{ i\omega' - D_v(v_s)\frac{\partial^2}{\partial v^2} \right\} \delta f_\ell^{(t)} = \frac{ic\ell}{Br}\delta\phi_\ell \frac{\partial f_0}{\partial r}, \tag{3.36}$$

where only the second derivative term in the Fokker-Planck collision operator has been retained. In the separatrix boundary layer region, where derivatives are large, the second velocity derivative term suffices. Here, $D_v(v_s)$ is the coefficient of parallel velocity diffusion evaluated at the separatrix velocity $v_s = v_s(r)$ and is given by Eq. (3.10).

For $\ell > 0$, the solution to Eq. (3.36) is given by

$$\delta f_\ell^{(t)} = \frac{c\ell}{Br}\frac{\delta\phi_\ell}{\omega'}\frac{\partial f_0}{\partial r} + a \exp\left[\frac{1+i}{\sqrt{2}} \sqrt{\frac{\omega'}{D_v(v_s)}}(v - v_s) \right], \tag{3.37}$$

where a is an arbitrary constant and we have chosen the sign so that the exponential decays as $(v - v_s)$ becomes large and negative. The new term represents a collisional correction in a boundary layer of width $\delta v_s^{(t)} \sim \sqrt{D_v(v_s)/\omega'}$. To understand this width, note that the sign of the perturbation seen by the trapped particles changes on the time scale $1/\omega'$, and velocity diffusion can extend to the width $\delta v_s^{(t)}$ during this time [i.e., $(\delta v_s^{(t)})^2 \sim D_v(v_s)/\omega'$].

Similarly, the passing-particle perturbation satisfies the equation

$$\left\{ v\frac{\partial}{\partial z} + \frac{e}{m}\frac{\partial \phi_0}{\partial z}\frac{\partial}{\partial v} - D_v(v_s)\frac{\partial^2}{\partial v^2} \right\} \left(\delta f_\ell^{(p)} - \frac{e\delta\phi_\ell}{T} f_0 \right) = 0, \tag{3.38}$$

where we have used $C(f_0) = 0$. The solution of Eq. (3.38) requires some information concerning the z-dependence of the mode quantities, but we can obtain an order of magnitude estimate to the collisional correction to $\delta f_\ell^{(p)}$ by noting that the operator

$$v\frac{\partial}{\partial z} + \frac{e}{m}\frac{\partial \phi_0}{\partial z}\frac{\partial}{\partial v} \approx i\omega_b, \tag{3.39}$$

is a derivative along a bounce orbit, which can be taken of order ω_b since passing particles see the mode quantities change by order unity during a bounce orbit. Substituting Eq. (3.39) into Eq. (3.38) and solving the resulting equation yields

$$\delta f_\ell^{(p)} = \frac{e\delta\phi_\ell}{T} f_0 + b \exp\left[\frac{-(1+i)}{\sqrt{2}}\sqrt{\frac{\omega_b}{D_v(v_s)}}(v - v_s)\right]. \tag{3.40}$$

In this case, the correction is of width $\delta v_s^{(p)} \sim \sqrt{D_v(v_s)/\omega_b}$, since the passing particles see a sign change on the bounce time scale $1/\omega_b$.

There is a disparity between the width of the boundary layer for trapped and passing particles: $\delta v_s^{(p)} \ll \delta v_s^{(t)}$ since $\omega_b \gg \omega'$. The consequence of this disparity is that only the trapped-particle correction contributes significantly to the damping. Choosing a and b so that the value and slope of the distribution are continuous at $v = v_s$ yields

$$a = \delta\phi_\ell \left[\frac{ef_0}{T} - \frac{c\ell}{Br\omega'}\frac{\partial f_0}{\partial r}\right]_{v=v_s} \left(\frac{\sqrt{\omega_b}}{\sqrt{\omega_b} + \sqrt{\omega'}} - \frac{\sqrt{2}}{1+i}\frac{\sqrt{D_v}}{\sqrt{\omega_b} + \sqrt{\omega'}}\frac{mv_s}{T}\right) \tag{3.41}$$

and

$$b = -\delta\phi_\ell \left[\frac{ef_0}{T} - \frac{c\ell}{Br\omega'}\frac{\partial f_0}{\partial r}\right]_{v=v_s} \left(\frac{\sqrt{\omega'}}{\sqrt{\omega_b} + \sqrt{\omega'}} + \frac{\sqrt{2}}{1+i}\frac{\sqrt{D_v}}{\sqrt{\omega_b} + \sqrt{\omega'}}\frac{mv_s}{T}\right). \tag{3.42}$$

Dropping terms of order $\sqrt{\omega'/\omega_b}$ gives $a = \delta\phi_\ell[ef_0/T - (c\ell/Br\omega')(\partial f_0/\partial r)]_{v=v_s}$ and $b \simeq 0$. Substituting into Poisson's equation then yields an eigenvalue equation for the mode potential

$$\nabla_\perp^2 \delta\phi_\ell = 4\pi e \left\{\frac{en_p}{T} + \frac{c\ell}{Br}\frac{\partial n_t}{\partial r}\frac{1}{\omega'} + \frac{2\sqrt{2}}{1+i}\sqrt{\frac{D_v(v_s)}{\omega'}}\left[\frac{ef_0}{T} - \frac{c\ell}{Br}\frac{\partial f_0}{\partial r}\frac{1}{\omega'}\right]_{v=v_s}\right\}\delta\phi_\ell, \tag{3.43}$$

which is subject to the boundary conditions $\delta\phi_\ell(0) = \delta\phi_\ell(R_w) = 0$. Multiplying both sides of Eq. (3.43) by $\delta\phi_\ell^*$, integrating over rdr, setting $\omega = \omega_r + i\gamma$, and taking the imaginary part of both sides yields an expression for the growth or damping rate

$$\boxed{\text{C}}\longrightarrow \gamma = \frac{\frac{B}{\ell}\int_0^{R_w} rdr|\delta\phi_\ell|^2\sqrt{\frac{2D_v(v_s)}{\ell\omega_E-\omega_r}}\left[\frac{ef_0}{T}-\frac{c\ell}{Br}\frac{\partial f_0}{\partial r}\frac{1}{\ell\omega_E-\omega_r}\right]_{v=v_s}}{\int_0^{R_w} dr\frac{|\delta\phi_\ell|^2}{(\ell\omega_E-\omega_r)^2}\frac{\partial n_t}{\partial r}}. \tag{3.44}$$

For the plasmas considered here, the numerator in Eq. (3.44) is positive and the denominator is negative so that the mode is damped. To lowest order in the small parameters γ/ω_r and $\sqrt{\nu/(\ell\omega_E-\omega_r)}$, the eigenmode $|\delta\phi_\ell|$ may be approximated by the eigenmode for $\nu = 0$. Indeed, the γ values predicted in this way by Eq. (3.44) agree closely with those obtained by direct numerical solution of Eq. (3.43) using a shooting method.

To understand the energy budget for the damping, we rewrite Eq. (3.44) as

$$0 = 2\gamma W + \int_0^{R_w} rdr\int_0^{2\pi} d\theta 2e\delta\phi(r,\theta,t)\frac{d}{dt}[L\delta n_c(r,\theta,t)] \tag{3.45}$$

$$+\int_0^{R_w} rdr\int_0^{2\pi} d\theta\left[-e\frac{\partial\phi_0}{\partial r}\right][\delta v_r(r,\theta,t)\delta n_c(r,\theta,t)2L],$$

where

$$W = \frac{2Lec\omega\ell}{B}\int_0^{R_w} 2\pi dr\frac{|\delta\phi_\ell|^2}{(\ell\omega_E-\omega_r)^2}\frac{\partial n_t}{\partial r} \tag{3.46}$$

is the mode energy, which turns out to be negative. The first term in Eq. (3.45) is the rate of change of mode energy, which is positive during damping since both W and γ are negative. In the second term, the quantity $\delta n_c(r,\theta,t)$ is the collisional correction to the trapped electron perturbation, and the convective derivative $d(L\delta n_c)/dt = (\partial/\partial t + \omega_E\partial/\partial\theta)(\delta n_c L)$ is the flux of scattered electrons to the side where the mode potential is $+\delta\phi(r,\theta,t)$. As an electron moves along the magnetic field lines from the side where the potential is $-\delta\phi$ to the side where it is $+\delta\phi$, the mode does work $2e\delta\phi$ on the electron. The second term is the rate of such work, which turns out to be positive. In the third term, the quantity

$\delta v_r(r,\theta,t) = -(c/Br)(\partial\delta\phi/\partial\theta)$ is the radial drift velocity imparted by the mode potential, so the product $(\delta v_r \delta n_c)$ is the radial flux of scattered particles. Thus, the third term is the rate at which the mode does work in moving the scattered particles through the potential gradient $\partial\phi_0/\partial r$. There is a net outward radial flux of scattered particles, so the third term is negative, balancing the other two terms. In summary, the mode potential increases the kinetic energy of the scattered particles by acceleration along the magnetic field and decreases the electrostatic energy of the particles by radial transport outward, the latter effect being dominant. When the liberated energy is added to the negative energy mode, the mode damps.

To understand the sign of the second term, first recall that in the absence of collisions, $\delta f_p(v_s) > 0$ and $\delta f_t(v_s) < 0$ on the side where $\delta\phi > 0$. On this side, the smoothing action of collisions must produce a velocity-space flux from passing to trapped. The situation is reversed on the other side where $\delta\phi < 0$. Thus, the net effect is a spatial flux of trapped particles from the side where $\delta\phi < 0$ to the side where $\delta\phi > 0$. Physically, this is reasonable, since we expect collisions to produce a flux of trapped particles from the high potential energy side $(-e\delta\phi > 0)$ to the low potential energy side $(-e\delta\phi < 0)$. Equivalently, we expect collisions to produce heating, and the second term is the heating rate.

The θ-average radial flux is given by

$$\frac{1}{2\pi}\int_0^{2\pi} d\theta \delta v_r \delta n_c = D_r(r)\left[-\frac{\partial n_0}{\partial r} + \frac{e}{T}\frac{\partial \phi_0'}{\partial r} n_0\right], \tag{3.47}$$

where $D_r(r) = \epsilon(\Delta r)^2\omega'$ is a neo-classical like diffusion coefficient. To understand this coefficient, note first that $\epsilon = 2\sqrt{2D_v(v_s)/\omega'}\exp\left[-v_s^2/2\bar{v}^2\right]/\sqrt{2\pi\bar{v}^2}$ is the fraction of particles in the boundary layer at radius r, where $v_s = v_s(r)$. In the absence of the mode, the $\mathbf{E}\times\mathbf{B}$ drift orbits are circular for all of the particles. In the presence of the mode, the orbits for the trapped particles are distorted from circularity by an amount $\Delta r = c\ell|\delta\phi_\ell|/Br\omega'$, and the distortions on the two ends are 180° out of phase. When a trapped particle is scattered and changes trapped-particle class (and drift orbit), the particle effectively makes a radial step Δr. For the particles in the boundary layer, the class changes at the rate ω'.

Eq. (3.47) is the usual form for the transport flux in the presence of a density gradient and an external force with the diffusion and mobility coefficients related by an Einstein relation[20] (i.e., $\mu = (e/T)D$). The radial electric field $-\partial\phi_0'/\partial r = -\partial\phi_0/\partial r + (r\omega_\ell/\ell)(B/c)$ is the effective field in the rotating frame of the wave. This is the frame where the mode perturbation is static and the Einstein relation is valid. One can easily understand that diffusion in a negative density gradient ($\partial n_0/\partial r < 0$) produces an outward radial flux. However, the origin of the mobility term is more subtle. In $\mathbf{E} \times \mathbf{B}$ drift motion, electrons can move radially only due to an azimuthal electric field. Why then is there a preference for transport in the direction of the radial electric force?

In fact, this radial mobility preference is intimately connected with the net axial flux of scattered particles from the high potential energy side ($-e\delta\phi > 0$) to the low potential energy side ($-e\delta\phi < 0$). The preference for outward radial transport when $e\partial\phi_0'/\partial r > 0$ is illustrated by the schematic diagram in Fig. 3.11. For the case $\ell = 1$, the solid curves represent potential energy contours [i.e., $-e\phi_0'(r) - e\delta\phi(r, \theta) = \text{const.}$] on one side of the barrier, and the dashed curves the contours on the other side. The difference between the two arises from the fact that $\delta\phi$ has opposite signs in the two ends. If we work in the rotating frame of the wave, the pattern is stationary (except for the slow damping). A particle that is initially trapped in one end at point A will $\mathbf{E} \times \mathbf{B}$ drift along the contours until it comes to the point B where the contour is furthest from the center; that is, where $-e\delta\phi(r, \theta)$ takes its maximum value. Statistically, this is the point where the particle is most likely to be detrapped and move rapidly to the other end, where this particle or an equivalent particle is scattered and trapped. The particle will then $\mathbf{E} \times \mathbf{B}$ drift along the dashed contour, continuing its motion outward to point C. Repeating the process then takes the particle to points D and E.

If the sign of $e\partial\phi_0'/\partial r$ changes to negative, the dashed curves change into solid curves and vice versa, but this relabeling is not significant. The important change is that the particle now $\mathbf{E} \times \mathbf{B}$ drifts azimuthally in the opposite sense, and so spirals radially inward (E $\rightarrow$ D $\rightarrow$ C $\rightarrow$ B $\rightarrow$ A). The jumps from one side to the other now happen when the contour is closest to the center.

The sign of $e\partial\phi_0'/\partial r$ changes to negative if the angular velocity of the rotating frame exceeds the plasma rotation velocity. This implies that rapidly rotating asymmetric potentials can be used to compress the plasma radially. This technique has been known for some time and is generally known as the "rotating wall" effect[13]. We suggest that trapped-particle transport is the microscopic mechanism of the "rotating wall" in some circumstances.

Another frame in which $e\partial\phi_0'/\partial r$ is negative is one that co-rotates with a high frequency trapped-particle mode. An analysis similar to that given above for the low frequency mode reveals that the high frequency modes are also damped by the same collisional scattering process. The high frequency modes are self-shielded with the potential perturbation being largest at inner radii where $\partial n_t/\partial r$ is positive. As a result, the wave energy given by integral (3.46) is positive for the high frequency modes. Again, energy conservation requires that the third term of Eq. (3.45) cancel the first two terms. The second term represents the work done by the wave as particles move axially and remains $2e\delta\phi$. Since the first two terms now have opposite signs, the third term could be either positive or negative. However, for the high frequency modes $(\omega_r - \ell\omega_E)^2$ is usually quite small and the first term is large and positive. This requires the third term to be negative. Therefore, the damping of the high frequency modes is associated with a net inward radial flux. Flux can be inward because $\partial\phi_0'/\partial r$ is negative for high frequency modes.

Finally, we compare the measured and predicted and damping rates for the lower frequency mode using realistic density profiles in the theory. Figures 3.12, 3.13 and 3.14 show a comparison of the predicted and measured rates versus squeeze voltage, magnetic field strength, and temperature, respectively. The agreement is to within 50 % over the expected range of validity for the theory. To understand the scaling trends we turn to Eq. (3.44). Since the denominator increases with the number of trapped particles, which increases with the squeeze voltage, the damping rate is expected to be a decreasing function of the squeeze voltage, and this trend is apparent in Fig. 3.12. Since ω_r and ω_E are proportional to $1/B$, Eq. (3.44) implies that γ scales as $1/\sqrt{B}$. This scaling is observed for large field strength ($B \simeq 2 - 10$ kG), where the theory assumption $\omega_b \gg \omega_E, \omega_r$ is well satisfied, but $\gamma \propto 1/B$ scaling is observed at lower field strength. This latter scaling is not understood theoretically.

Figure 3.14 shows that the measured and calculated damping rates are decreasing functions of temperature over the range of measurements ($T = 0.5 - 6$ eV), with the experiments showing a somewhat stronger temperature dependence. The discrepancy may be due to a radial dependence in the plasma temperature. There are some experimental indications that heating from radial transport caused by ambient field errors raises the temperature more at large r, where the damping mechanism acts, than at $r = 0$, where the temperature is measured. Moreover, the temperature inhomogeneity is more pronounced at higher temperatures where the cross-field heat conduction is lower. Including such a correction to the plasma temperature changes the slope of the measured values toward agreement with the theory.

Recent experiments have demonstrated a correspondence between the damping of trapped-particle diocotron modes and asymmetry-induced transport[15]. In these experiments, trapped particles are created in the usual manner with an applied "squeeze" voltage. Static field errors (such as magnetic tilt) are introduced in the trap and produce perturbed drift orbits that are quantitatively similar to drift orbits associated with trapped-particle modes. The rate of radial expansion of the plasma column is found to be proportional to the damping rate of the trapped-particle diocotron mode over a wide range of plasma parameters. This correspondence strongly suggest velocity space diffusion of marginally trapped particles as the microscopic mechanism responsible for asymmetry-induced transport.

3.7 Landau Resonances

Wave-particle resonances are possible for this mode, but the associated Landau damping is small compared to the collisional damping provided $\bar{\omega}_b \gg |\ell\omega_E(r) - \omega_r|$. Here, $\bar{\omega}_b$ is the axial bounce frequency for a thermal particle. In Appendix A, we neglect collisional damping and obtain the following expression for the Landau damping rate

$$\gamma_{LD} = -\frac{\pi \int_0^{R_w} r dr \int_0^\infty dI \sum_{n\neq 0} \left[\ell \frac{\partial f_0}{\partial p_\theta} - n\omega_b \frac{f_0}{T}\right] |\delta H_{\ell,n}|^2 \delta[n\omega_b + \ell\omega_E - \omega_r]}{\int_0^{R_w} r dr \int_0^\infty dI \frac{\ell \frac{\partial f_0}{\partial p_\theta} |\delta H_{\ell,0}|^2}{(\ell\omega_E - \omega_r)^2}}, \tag{3.48}$$

where $|\ell\omega_E - \omega_r|/\bar{\omega}_b$ and $\gamma_{LD}/|\ell\omega_E - \omega_r|$ are assumed to be small. Eq. (3.48) employs the canonical variables $(\theta, p_\theta, I, \psi)$, where $p_\theta = -eBr^2/2c$ is the canonical angular momentum conjugate to θ, and (I, ψ) are action-angle variables defined for the equilibrium Hamiltonian

$$H_0 = \frac{p_z^2}{2m} - e\phi_0(p_\theta, z). \tag{3.49}$$

The action is defined in the usual manner

$$I(p_\theta, H_0) = \frac{1}{2\pi} \oint dz' p_z[z', H_0, p_\theta], \tag{3.50}$$

and the Hamiltonian $H_0 = H_0(I, p_\theta)$ is obtained by inversion. The rotation and bounce frequencies are then given by

$$\omega_E(I, p_\theta) = \frac{\partial H_0}{\partial p_\theta} \qquad , \qquad \omega_b(I, p_\theta) = \frac{\partial H_0}{\partial I}. \tag{3.51}$$

The angle variable is given by

$$\psi = \sqrt{\frac{m}{2}} \int^z \frac{dz' \frac{\partial H_0}{\partial I}}{\sqrt{H_0(I, p_\theta) + e\phi_0(p_\theta, z')}}, \tag{3.52}$$

and the bounce harmonic of the mode potential by

$$\delta H_{\ell,n} = \frac{1}{2\pi} \int_0^{2\pi} d\psi \, e^{-in\psi} (-e) \delta\phi_\ell[z(\psi, p_\theta, I), p_\theta]. \tag{3.53}$$

With these definitions and expression (3.48), one can understand the issue that determines whether or not Landau damping is negligible. By hypothesis, the bounce frequency for a thermal particle, $\bar{\omega}_b = \omega_b(\bar{I}, p_\theta)$, is large compared to the Doppler shifted mode frequency $|\ell\omega_E - \omega|$.

Consequently, the argument of the delta function in Eq. (3.48) can vanish only for two special classes of particles. The first class consists of particles that are very close to the separatrix; the bounce frequency for these particles can be much smaller that $\bar{\omega}_b$. However, direct calculation shows that these particles lie well within the collision dominated boundary layer, provided $\bar{\omega}_b \gg |\ell\omega_E - \omega_r|$, so rapid collisional trapping and de-trapping destroys the Landau resonance. The second class consists of very slow particles (i.e., $I \ll \bar{I}$) that are deeply trapped on one side of the barrier or the other. These particles can provide significant Landau damping only if $\delta H_{\ell,n}(I, p_\theta)$ is substantial for the low values of I required for frequency resonance.

Recall that Debye shielding forces $\delta\phi_\ell(z,r)$ to be nearly z-independent in the trapped particle regions well away from the squeeze barrier. If $\delta\phi_\ell(z,p_\theta)$ were exactly z-independent over the region of z accessible to the deeply trapped particles, then Eq. (3.53) would imply that $\delta H_{\ell,n}=0$, and there would be no Landau damping. Thus, the strength of the Landau damping depends on the degree of z-dependence for $\delta\phi_\ell(z,r)$ in the accessible region.

In Appendix B, we obtain approximate numerical solutions for the z-dependence of the mode potential. As an example of the results, Fig. 3.15 shows the potential contours for the specific case of the density profiles in Fig. 3.4: a 20 Volt squeeze voltage, and a temperature of 1 eV. Using this solution for $\delta\phi_1(r,z)$, we evaluate expression (3.48) and obtain the Landau damping rate. Fig. 3.16 shows a comparison of the Landau and collisional damping rates at several values of magnetic field strength. For $B>2$ kG, the Landau damping rate is predicted to be negligible and collisions dominate the damping. In this high magnetic field regime the mode frequency is small compared to the bounce frequency. Therefore,only very deeply trapped particles bounce resonant with the wave and the wave-particle energy exchange is small. As the magnetic field strength is reduced, the mode frequency increases while the axial bounce frequency of the particles remains fixed. For low enough values of B, weakly trapped and even passing particles come into bounce resonance with the wave and the wave-particle energy exchange is larger. Near $B=1$ kG, the Landau damping rate is predicted to exceed the collisional rate. However, in this low magnetic field regime $\bar{\omega}_b \simeq |\omega_E-\omega_r|$, so a basic assumption of our theory is violated.

3.8 Conclusion

We have developed a quasi-3D model for the newly discovered trapped-particle diocotron mode. The mode consists of two diocotron oscillations that are excited 180° out of phase on either side of an applied squeeze barrier. The mode dynamics consists of trapped particles executing $\mathbf{E} \times \mathbf{B}$ drift motion, while passing particles stream along field lines in a Debye shielding action. The model developed here accurately predicts the frequency and eigenmode structure of the experimentally observed mode over a range of plasma parameters. Furthermore, the model predicts the existence of additional trapped-particle modes that have azimuthal phase velocities above the maximum column rotation frequency.

We have also identified the damping mechanism of the trapped-particle diocotron modes as velocity diffusion in a boundary layer near the trapped-passing separatrix. An analysis based on Fokker-Planck collisions yields a damping rate for the mode that agrees with observations to within 50% and predicts the essential scaling with plasma parameters. The damping of the negative energy modes is associated with a net outward radial flux of particles, and the damping of the positive energy modes is associated with a net inward radial flux of particles. Recent experiments suggest that the mechanism responsible for transport in the trapped-particle modes may be responsible as well for transport observed when static field asymmetries are applied to the plasma[15]. Finally, the full 3D mode potential was calculated and used to show that Landau damping of the trapped-particle modes is negligible in the high magnetic field limits, but may become the dominant damping process for low fields.

3.9 Acknowledgments

The authors enjoyed useful discussions with A. A. Kabantsev, C. F. Driscoll, J. H. Yu, D. H. E. Dubin, R. Spencer, and G. Mason.

This work was supported by National Science Foundation Grant No. PHY-9876999 and Office of Naval Research Grant No. N00014-96-1-0239.

APPENDIX A: DERIVATION OF LANDAU DAMPING EXPRESSION

Here, we derive an expression for rate of change in the trapped-particle wave amplitude due to interactions with bounce-resonant electrons. Since the trap is axisymmetric and the wall voltages are static, the total energy and canonical angular momentum are conserved quantities. Therefore, the unperturbed Hamiltonian is integrable and it is possible to obtain a canonical transformation to action-angle variables $(\theta, p_\theta, \psi, I)$. This transformation is carried out formally in Ref. [12]. In the new coordinates Eq. (3.5) becomes

$$\left(\frac{\partial}{\partial t} + \frac{\partial H_0}{\partial I}\frac{\partial}{\partial \psi} + \frac{\partial H_0}{\partial p_\theta}\frac{\partial}{\partial \theta}\right)\delta f = \left(\frac{\partial f_0}{\partial I}\frac{\partial}{\partial \psi} + \frac{\partial f_0}{\partial p_\theta}\frac{\partial}{\partial \theta}\right)\delta H, \tag{A-1}$$

where $C = 0$ in the present collisionless analysis. Here $p_\theta = -eBr^2/2c$ is the radial coordinate, $I = \oint p_z(z, p_\theta, H_0)dz$ is the bounce action and $\delta H = -e\delta\phi$ is the perturbed Hamiltonian. θ and ψ are the variables canonically conjugate to p_θ and I, respectively. We assume that the equilibrium satisfies the Boltzmann condition so that $\partial f_0/\partial H_0 = -f_0/T$. Solving Eq. (A-1) for perturbations that vary as $\exp[i(n\psi + \ell\omega_E - \omega t)]$ we obtain

$$\delta f_{\ell,n} = \left[\frac{\ell\frac{\partial f_0}{\partial p_\theta} - n\omega_b\frac{f_0}{T}}{n\omega_b + \ell\omega_E - \omega}\right]\delta H_{\ell,n}, \tag{A-2}$$

where $\omega_b = \partial H_0/\partial I$ is the bounce frequency and $\omega_E = \partial H_0/\partial p_\theta$ is the bounce averaged rotation frequency.

Substituting into the Poisson equation gives

$$\left[\frac{1}{r}\frac{\partial}{\partial r}\left(r\frac{\partial}{\partial r}\right) - \frac{\ell^2}{r^2} + \frac{\partial^2}{\partial z^2}\right]\delta\phi_\ell = -4\pi e\int_{-\infty}^{+\infty} dv \sum_{n=-\infty}^{+\infty} e^{in\psi}\left[\frac{\ell\frac{\partial f_0}{\partial p_\theta} - n\omega_b\frac{f_0}{T}}{n\omega_b + \ell\omega_E - \omega}\right]\delta H_{\ell,n}. \tag{A-3}$$

Multiplying the term on the left and side of Eq. (A-3) by $\delta\phi_\ell^*$ and integrating over the volume of trap yields a real quantity. Therefore, it must also be true that

$$0 = \mathrm{Im}\left\{\int_0^{R_w} 2\pi r dr\int_{-\infty}^{+\infty} dz\int_{-\infty}^{+\infty} dv\sum_{n,n'=-\infty}^{+\infty} e^{i(n-n')\psi}\left[\frac{\ell\frac{\partial f_0}{\partial p_\theta} - n\omega_b\frac{f_0}{T}}{n\omega_b + \ell\omega_E - \omega}\right]\delta H_{\ell,n'}^*\delta H_{\ell,n}\right\}. \tag{A-4}$$

Since phase space volume is conserved in Hamiltonian systems, $mdvdz = dId\psi$, we can rewrite Eq. (A-4) as

$$0 = \mathrm{Im}\left\{\int_0^{R_w} rdr\int_0^{\infty} dI\int_0^{2\pi} d\psi\sum_{n,n'=-\infty}^{+\infty} e^{i(n-n')\psi}\left[\frac{\ell\frac{\partial f_0}{\partial p_\theta} - n\omega_b\frac{f_0}{T}}{n\omega_b + \ell\omega_E - \omega}\right]\delta H_{\ell,n'}^*\delta H_{\ell,n}\right\}. \tag{A-5}$$

The ψ-integral gives the Kroenecker delta function $\delta_{nn'}$ and we have

$$0 = \mathrm{Im}\left\{\int_0^{R_w} rdr\int_0^{\infty} dI\sum_{n=-\infty}^{+\infty}\left[\frac{\ell\frac{\partial f_0}{\partial p_\theta} - n\omega_b\frac{f_0}{T}}{n\omega_b + \ell\omega_E - \omega}\right]|\delta H_{\ell,n}|^2\right\}. \tag{A-6}$$

Setting $\omega = \omega_r + i\gamma_{LD}$ and expanding in the small quantity γ_{LD}/ω_r we obtain

$$0 = \gamma_{LD}\int_0^{R_w} rdr\int_0^{\infty} dI\sum_{n=-\infty}^{+\infty}\left[\frac{\ell\frac{\partial f_0}{\partial p_\theta} - n\omega_b\frac{f_0}{T}}{(n\omega_b + \ell\omega_E - \omega_r)^2 + \gamma_{LD}^2}\right]|\delta H_{\ell,n}|^2. \tag{A-7}$$

For $\gamma_{LD} < 0$, the I-integral must be deformed into a contour that passes below the pole in accordance with Landau's initial value treatment. This procedure can be effected by replacing γ_{LD} with $|\gamma_{LD}|$ in the neighborhood of the pole. Integral (A-7) can be divided into resonant and non-resonant contributions. For $\omega_b \gg \omega_E - \omega_r$, the non-resonant contribution will be dominated by the $n = 0$ term

$$0 = \gamma_{LD} \int_0^{R_w} r dr \int_0^\infty dI \frac{\ell \frac{\partial f_0}{\partial p_\theta}}{(\ell\omega_E - \omega_r)^2} |\delta H_{\ell,0}|^2$$

$$+ |\gamma_{LD}| \int_0^{R_w} r dr \int_0^\infty dI \sum_{n \neq 0} \left[\frac{\ell \frac{\partial f_0}{\partial p_\theta} - n\omega_b \frac{f_0}{T}}{(n\omega_b + \ell\omega_E - \omega_r)^2 + \gamma_{LD}^2} \right] |\delta H_{\ell,n}|^2, \quad \text{(A-8)}$$

where the second integral is evaluated in the neighborhood of the resonant points. We are considering a situation in which $\omega_r \neq \omega_E(r)$ anywhere inside the plasma, so that the first term is a proper integral. In the limit of small γ_{LD}, the second term in Eq. (A-8) can be simplified using the following form of the Dirac delta function

$$\lim_{\epsilon \to 0^+} \frac{\epsilon}{(x-y)^2 + \epsilon^2} = \pi\, \delta(x-y) \quad \text{(A-9)}$$

and we find that

$$\gamma_{LD} = -\frac{\pi \int_0^{R_w} r dr \int_0^\infty dI \sum_{n \neq 0} \left[\ell \frac{\partial f_0}{\partial p_\theta} - n\omega_b \frac{f_0}{T} \right] |\delta H_{\ell,n}|^2 \delta[n\omega_b + \ell\omega_E - \omega_r]}{\int_0^{R_w} r dr \int_0^\infty dI \frac{\ell \frac{\partial f_0}{\partial p_\theta} |\delta H_{\ell,0}|^2}{(\ell\omega_E - \omega_r)^2}}, \quad \text{(A-10)}$$

which is Eq. (3.48).]

APPENDIX B: AXIAL DEPENDENCE OF MODE POTENTIAL

A direct solution of the complete 3D eigenvalue problem is a challenging numerical problem. Therefore, an iterative approach will be used to find an approximation of $\delta\phi_\ell(r,z)$ in the high bounce frequency limit ($\omega_b \gg \ell\omega_E - \omega$). Including axial dependence, the Poisson equation for the perturbations is

$$\left[\frac{1}{r} \frac{\partial}{\partial r} \left(r \frac{\partial}{\partial r} \right) - \frac{\ell^2}{r^2} + \frac{\partial^2}{\partial z^2} \right] \delta\phi_\ell(r,z) = 4\pi e \delta n_\ell(r,z). \quad \text{(B-1)}$$

To get the density perturbation $\delta n_\ell(r,z)$, we note that there is a drift and an adiabatic contribution. From Eq. (3.13), the adiabatic contribution is given by

$$\delta n_\ell^{(a)} = \int_{-\infty}^{+\infty} dv \frac{e f_0(r,z,v)}{T} \delta\phi_\ell(r,z) - \int_{-v_s(r)}^{v_s(r)} dv \frac{e f_0(r,z,v)}{T} \langle \delta\phi_\ell(r,z) \rangle, \quad \text{(B-2)}$$

where we have used $\langle \delta\phi_\ell \rangle = 0$ for passing particles. The first integral on the right hand side of Eq. (B-2) is straightforward. However, the second integral cannot be evaluated without first obtaining $\delta\phi_\ell(r,z)$ which is not yet known. In order to simplify the calculation, we recall that the squeeze and end regions are small compared to the overall column length. To a good approximation we can use the infinitesimal squeeze region solutions found in section 3.5 for the bounce average potential, that is, $\langle \delta\phi_\ell(r,z) \rangle \approx \delta\phi_\ell(r)$, where $\delta\phi_\ell(r)$ is a solution to Eq. (3.27). Thus, the adiabatic density perturbation is

$$\delta n_\ell^{(a)} = \frac{en_0(r,z)}{T}\delta\phi_\ell(r,z) - \frac{en_t(r,z)}{T}\delta\phi_\ell(r), \tag{B-3}$$

The drift perturbation can be found by considering the change in the number of trapped particles on a field line due to the presence of the mode. Again, we make the approximation $\langle \delta\phi_\ell(r,z) \rangle \approx \delta\phi_\ell(r)$ and obtain the radial displacement of the trapped particles $\Delta r = -c\ell\delta\phi_\ell(r)/Br\omega'(r)$. The associated density perturbation due to drift motion is

$$\delta n_\ell^{(d)} = n_t(r-\Delta r, z) - n_t(r,z) = \frac{c\ell}{Br}\frac{\partial n_t(r,z)}{\partial r}\frac{\delta\phi_\ell(r)}{\omega'(r)}, \tag{B-4}$$

where $\omega'(r) = \ell\omega_E(r) - \omega$ and ω is given in the solution of Eq. (3.27). Of course, the passing particles have no bounce average drift perturbation.

Substituting the total density perturbation into Poisson's equation yields the equation

$$\left\{\frac{1}{r}\frac{\partial}{\partial r}\left(r\frac{\partial}{\partial r}\right) - \frac{\ell^2}{r^2} + \frac{\partial^2}{\partial z^2}\right\}\delta\phi_\ell(r,z) - \frac{4\pi e^2 n_0(r,z)}{T}\delta\phi_\ell(r,z)$$

$$= \left[\frac{4\pi ec\ell}{Br\omega'(r)}\frac{\partial n_t(r,z)}{\partial r} - \frac{4\pi e^2 n_t(r,z)}{T}\right]\delta\phi_\ell(r). \tag{B-5}$$

For consistency, we verify that $\delta\phi_\ell(r,z) = \delta\phi_\ell(r)$ inside the main column by setting them equal in Eq. (B-5) and noting that Eq. (3.27) is recovered. The radial boundary conditions on Eq. (B-5) are $\delta\phi_\ell(0,z) = \delta\phi_\ell(R_w,z) = 0$. Further, $\delta\phi_\ell(r,0) = 0$

because the mode is odd about $z = 0$. At large z, the mode potential decays exponentially and we impose the condition $\delta\phi_\ell(r, L_\infty) = 0$, where L_∞ is suitably larger than L. Eq. (B-5) is discretized and solved directly by matrix inversion.

This chapter has been submitted to Physics of Plasmas: "Trapped-Particle Diocotron Modes", T. J. Hilsabeck and T. M. O'Neil, (2003). T. J. Hilsabeck was the primary investigator and author of this paper.

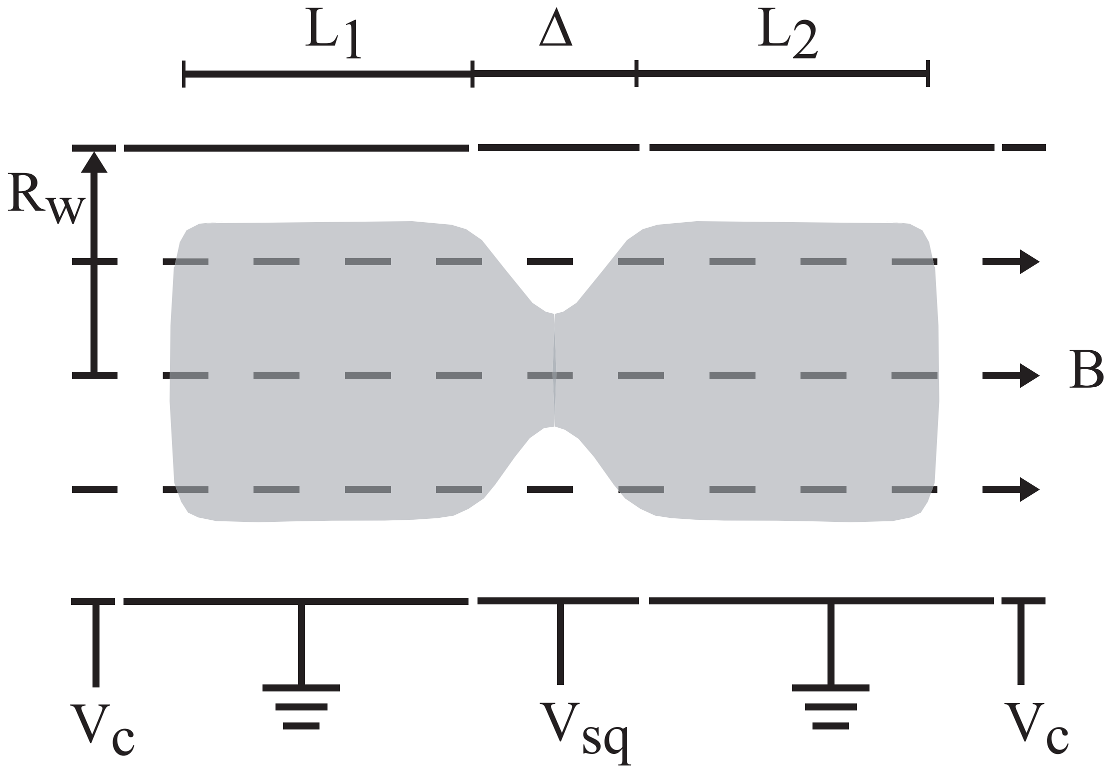

Figure 3.1: A nonneutral plasma column confined in a Malmberg-Penning trap that has been partially divided by the application of an external squeeze voltage, V_{sq}.

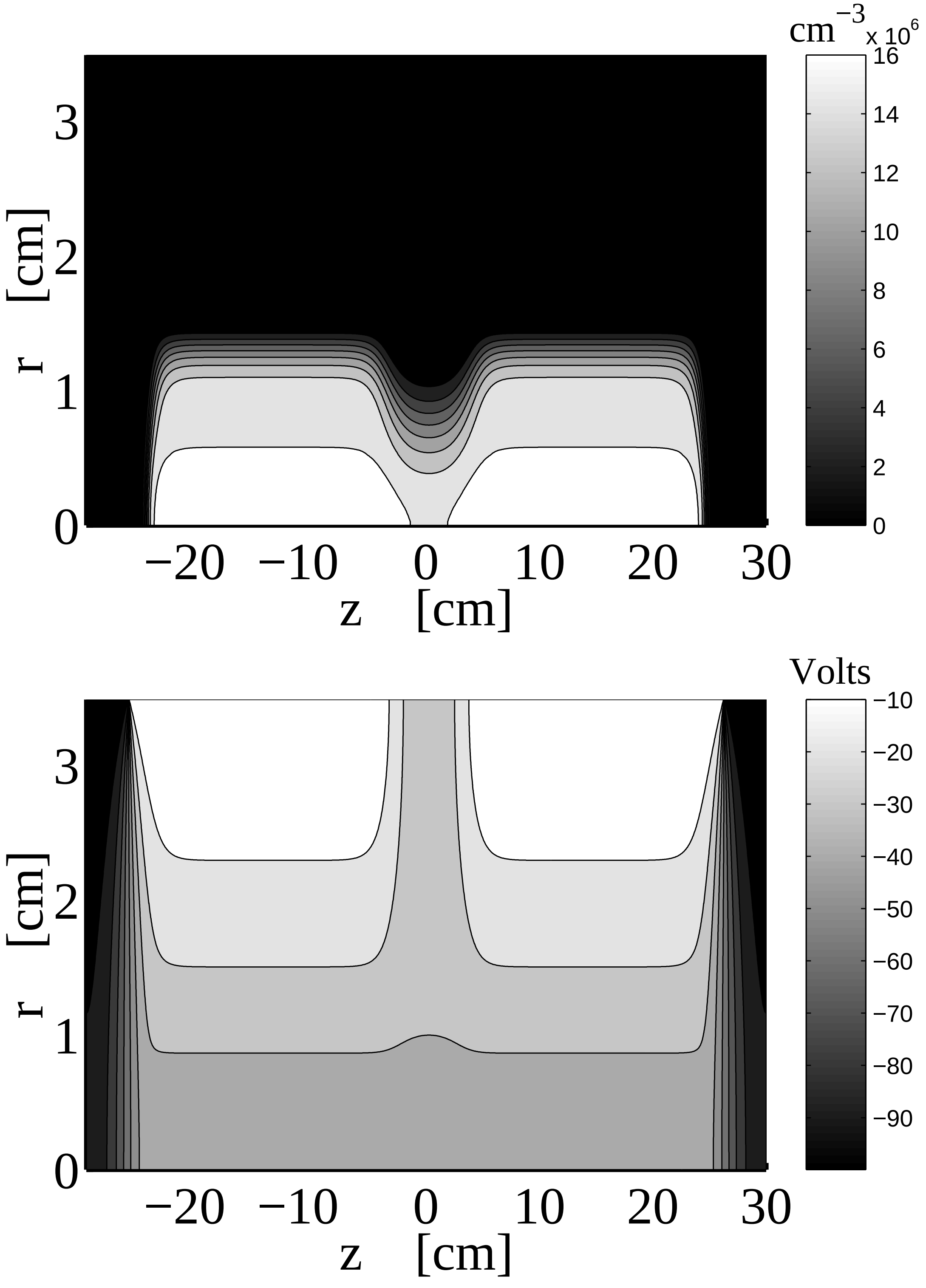

Figure 3.2: Density and potential contours for a squeezed column equilibrium.

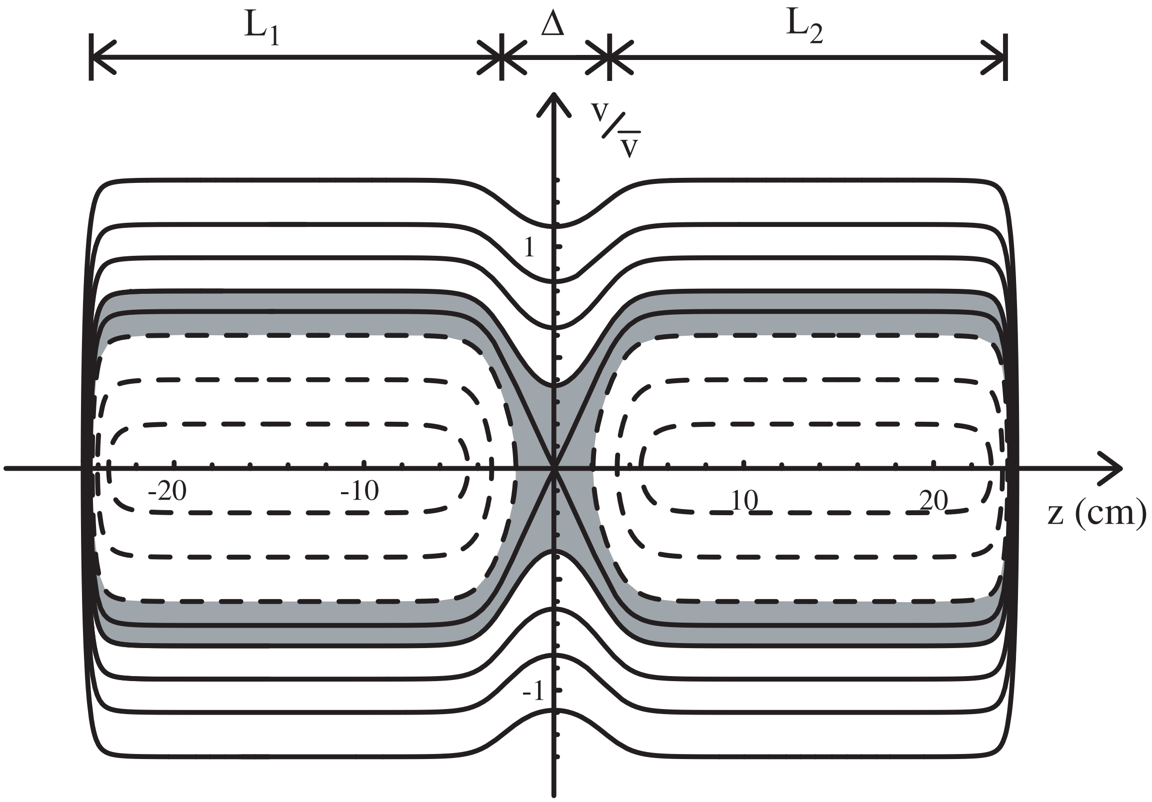

Figure 3.3: Phase-space orbits at $r = 0.5$ cm with an applied squeeze potential $V_{sq} \sim \phi_0(0,0)/2$. The shaded region represents the boundary layer (not to scale) where velocity space diffusion occurs and causes mode damping.

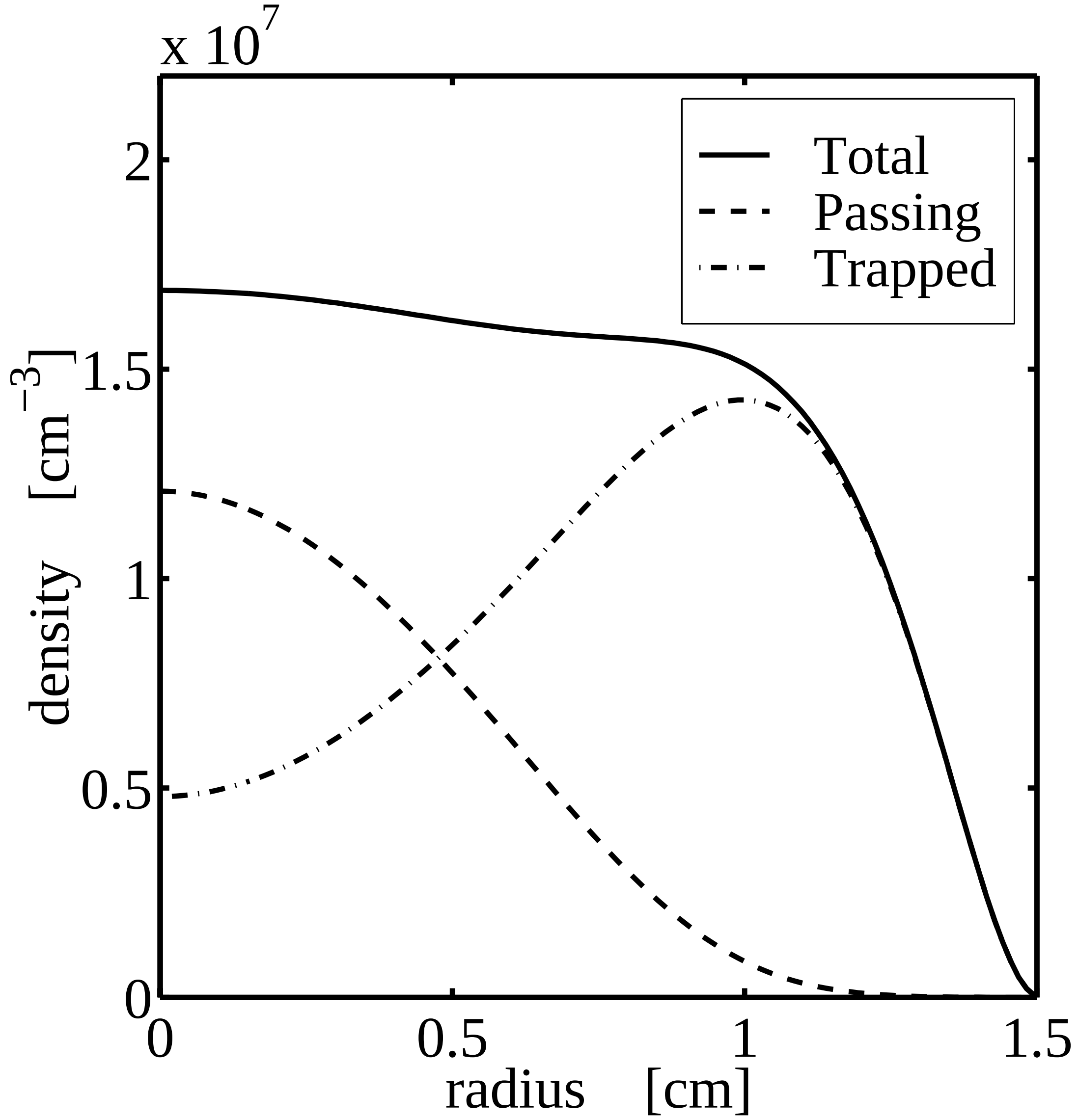

Figure 3.4: Trapped, passing and total particle density profiles.

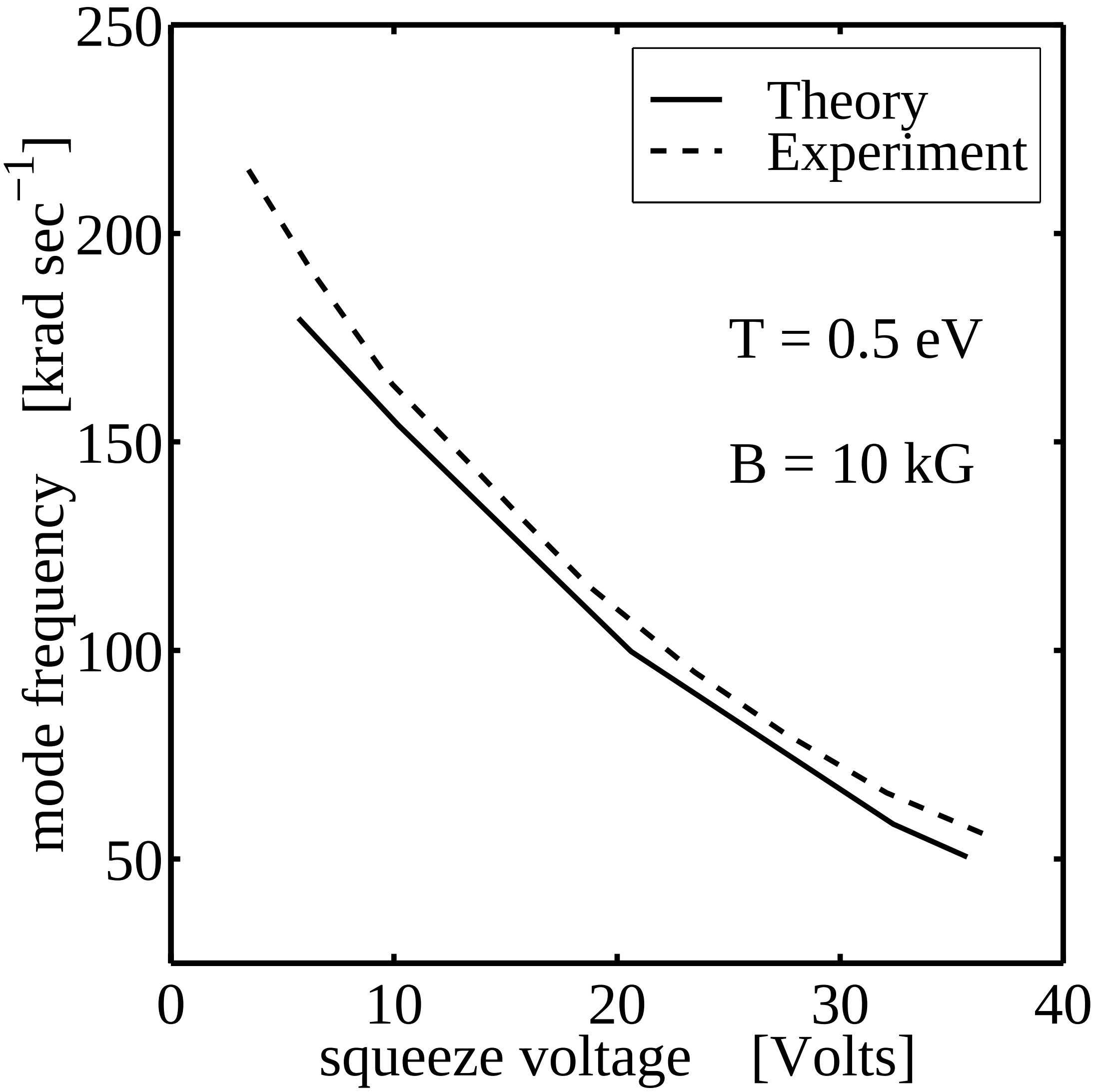

Figure 3.5: Mode frequency versus applied squeeze voltage for the low frequency trapped-particle mode. The value varies smoothly between the rotation frequency at the radial edge of the plasma and the diocotron mode frequency.

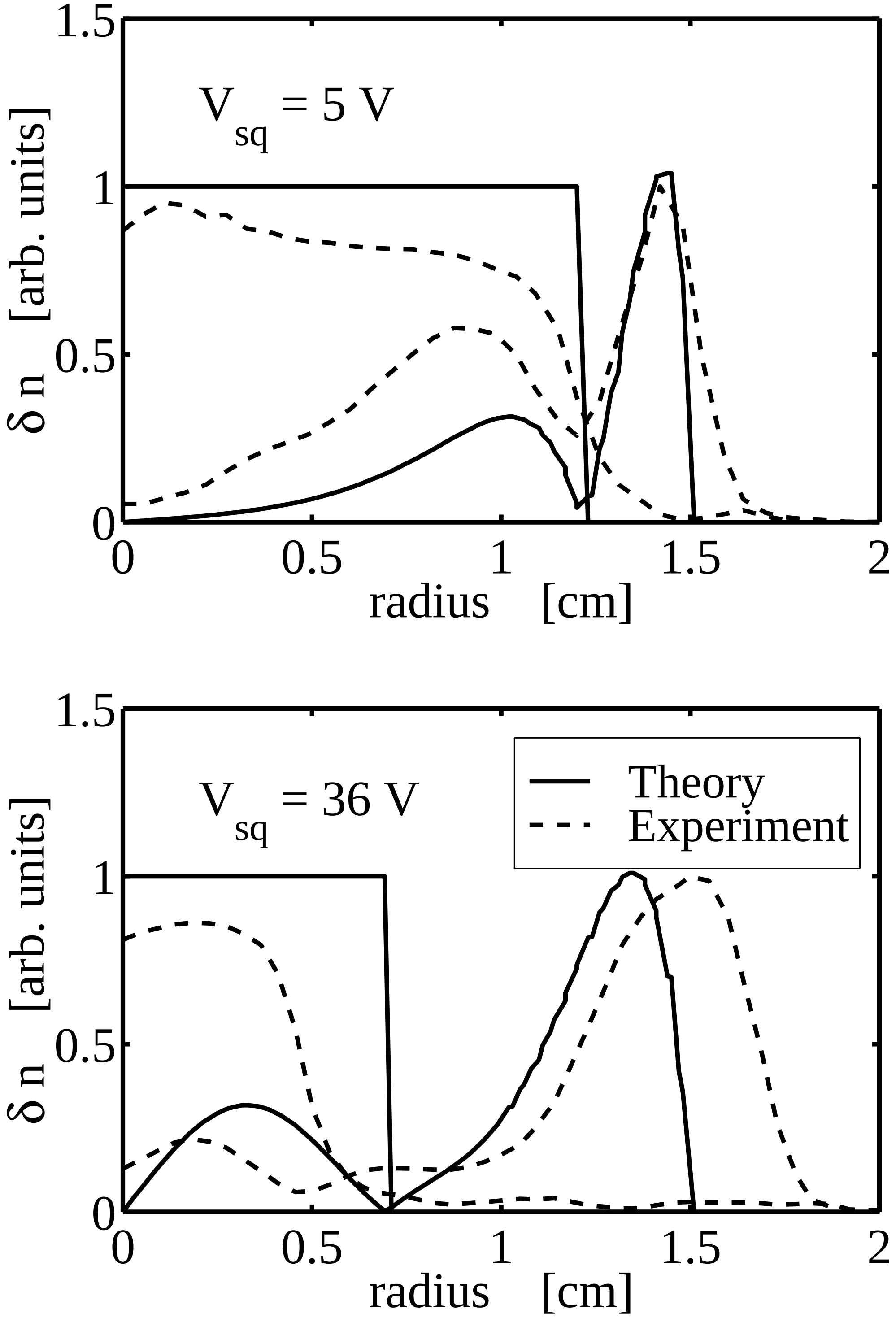

Figure 3.6: Density eigenfunctions for the low frequency trapped-particle mode at 5 and 36 Volt squeeze. The theoretical calculation used a density profile that was truncated at 1.5 cm. The curves which approach zero at $r = 0$ are $|\delta n|$. The curves which are finite at $r = 0$ represent the phase of δn normalized to π.

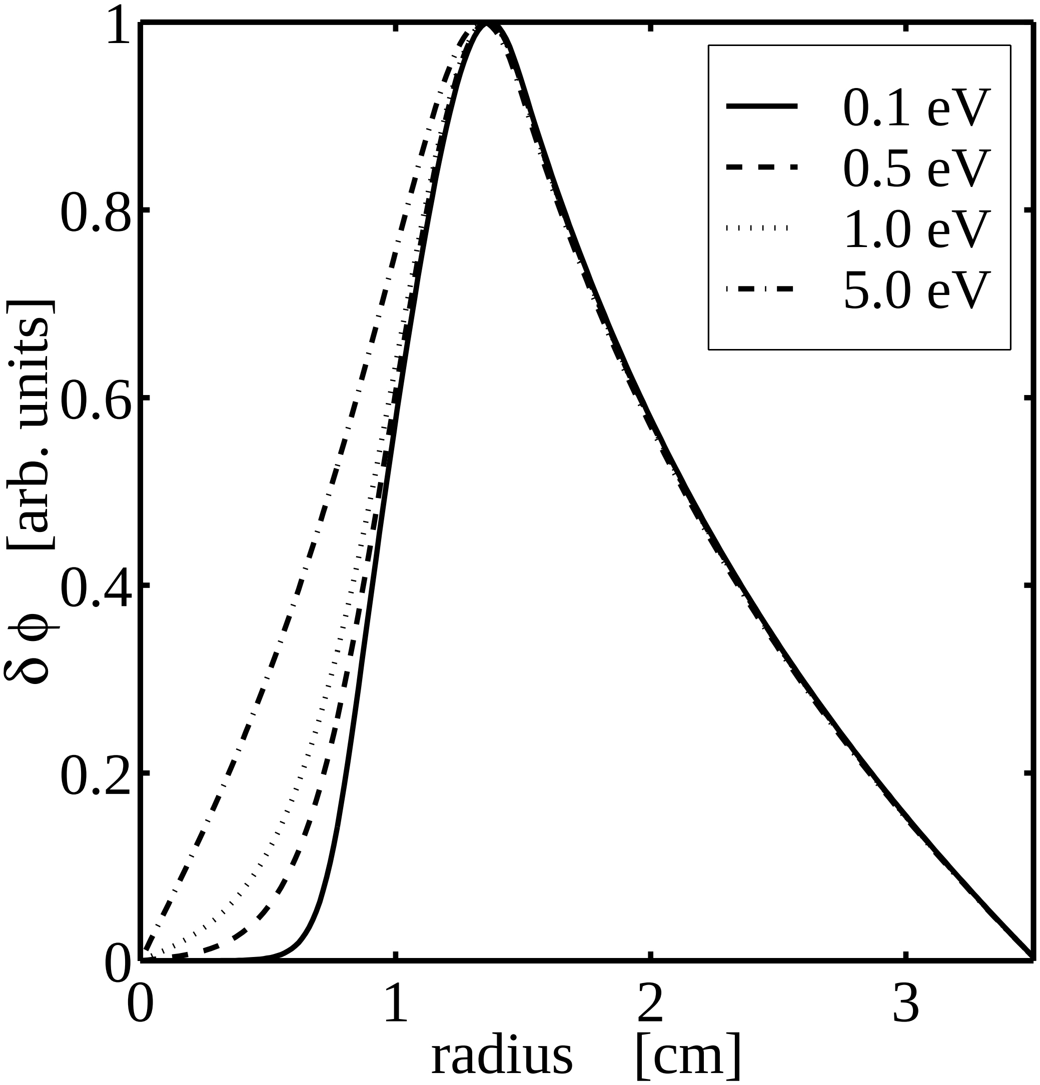

Figure 3.7: Mode potentials at various temperatures. At low temperatures the potential is shielded from inner radii by the passing particles.

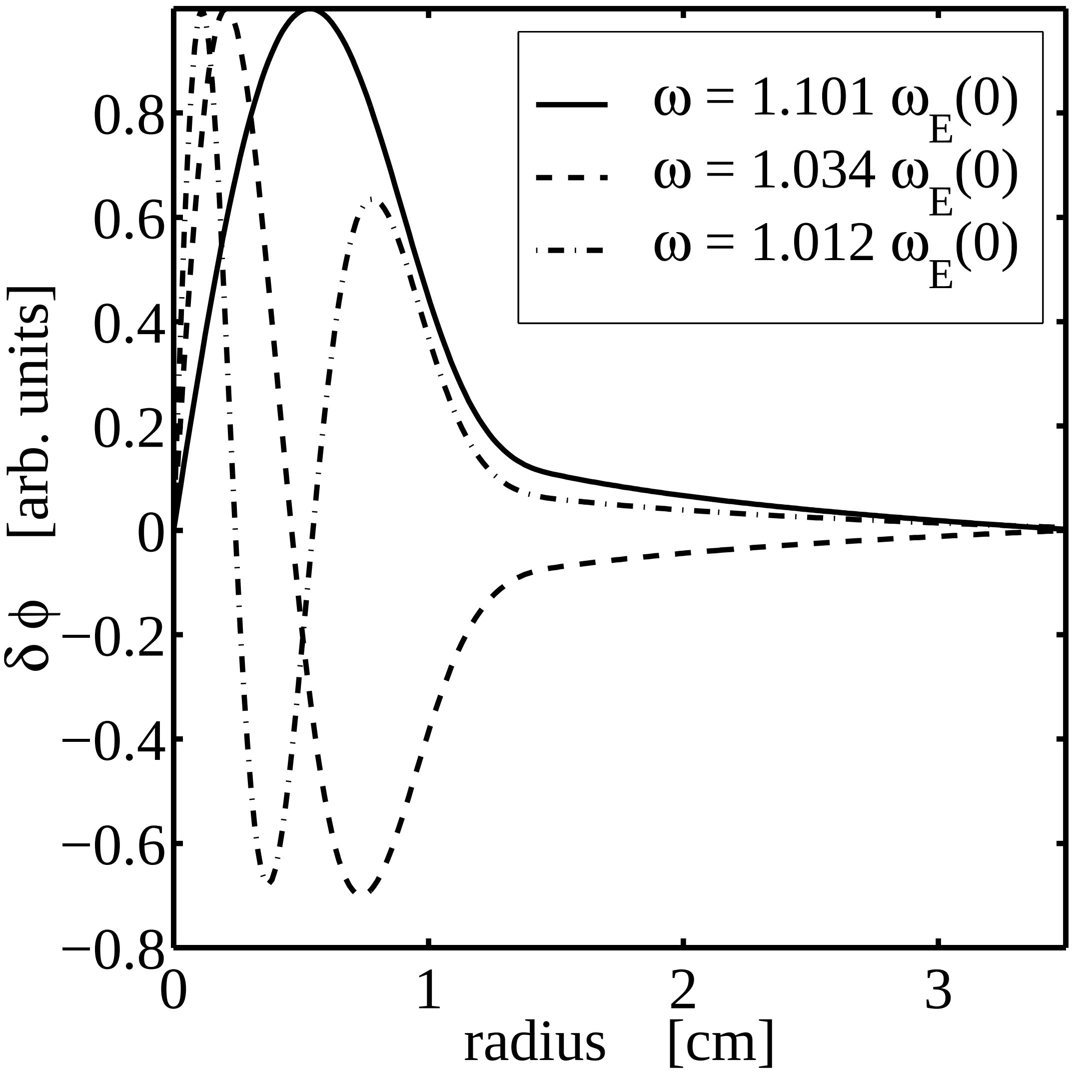

Figure 3.8: Upper branch mode potentials. As the radial nodes increase, the wave phase velocity approaches the rotation frequency on center.

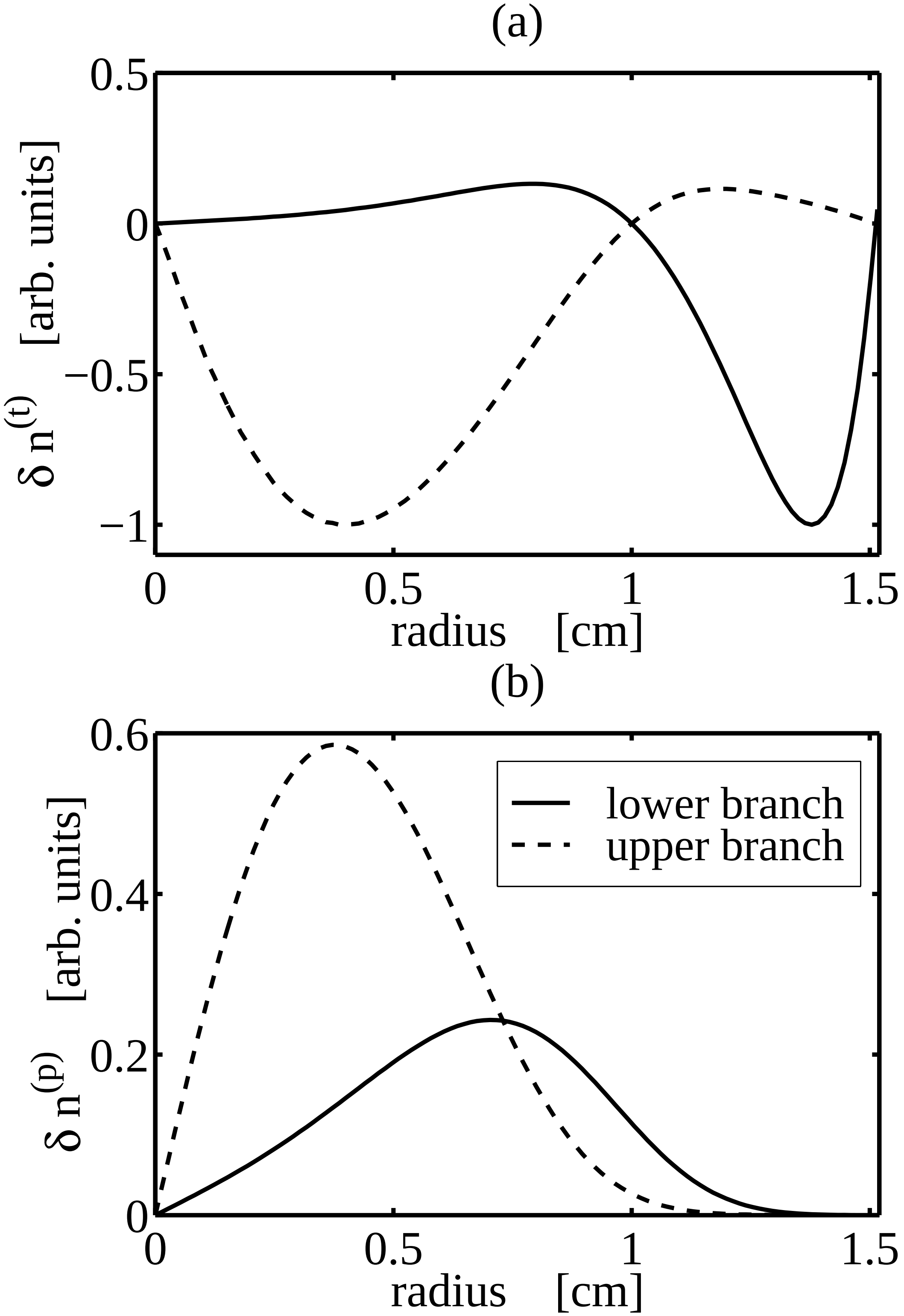

Figure 3.9: Trapped (a) and passing (b) density perturbations for the low frequency and first high frequency modes.

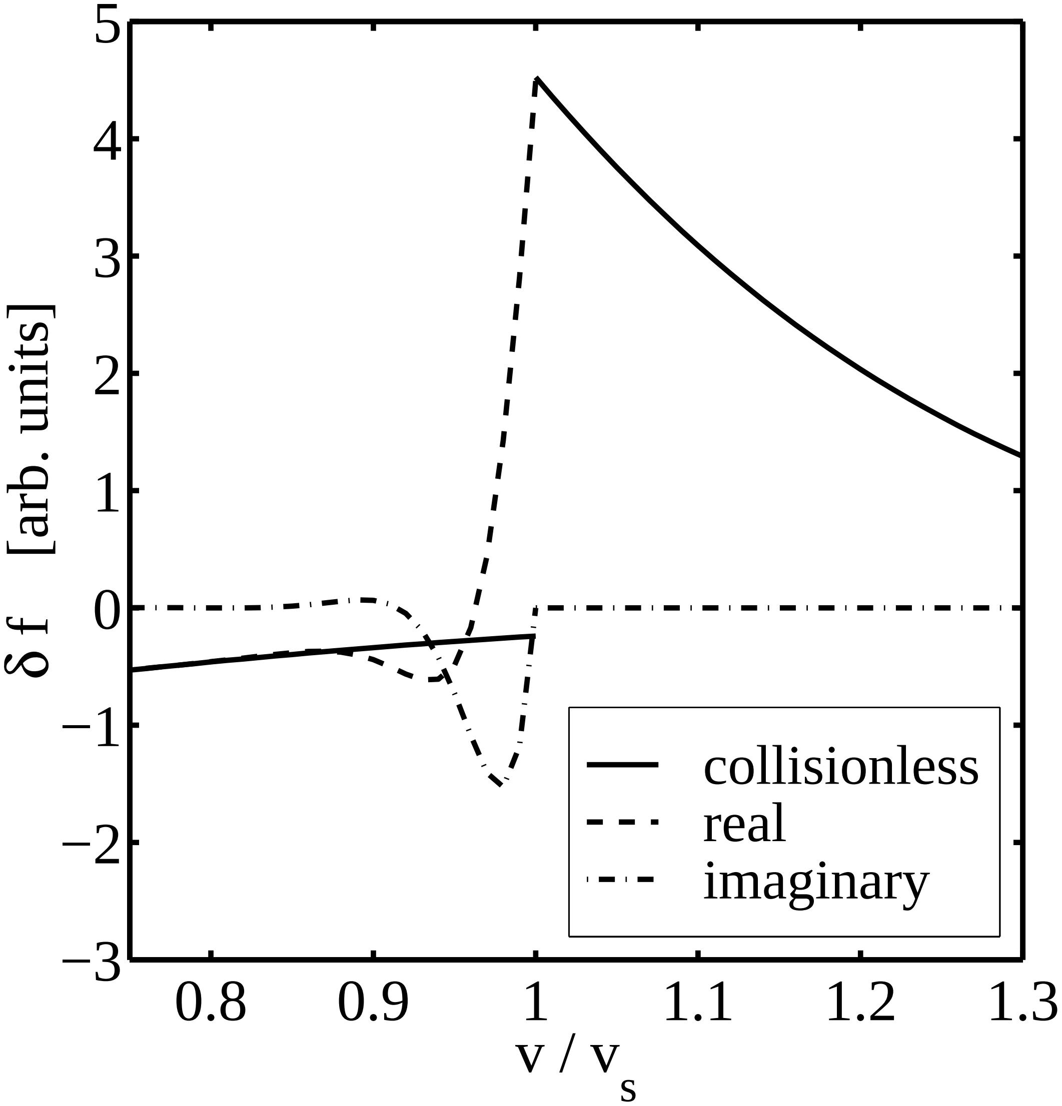

Figure 3.10: Perturbed distribution function at r = 1 cm. Solid line is the collisionless theory and exhibits a discontinuity at the separatrix radius. Dashed line is the collisional correction to the real part of δf. Dot-dashed line is the imaginary part of the collisional correction to δf.

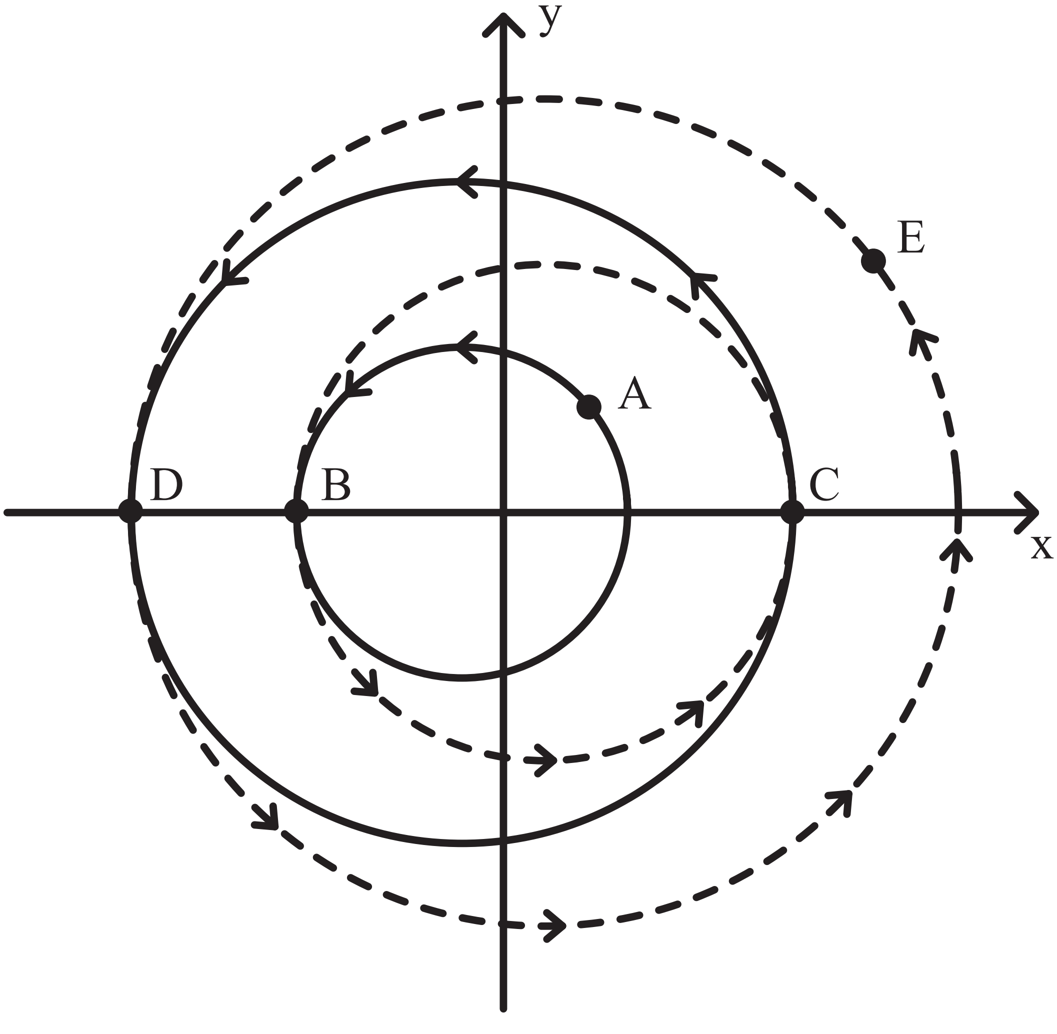

Figure 3.11: Potential energy contours in the frame of an $\ell = 1$ wave (solid $z > 0$, dashed $z < 0$). A particle initially at point A is transported to point E through orbits along potential contours and detrapping/retrapping collisions at points B, C and D.

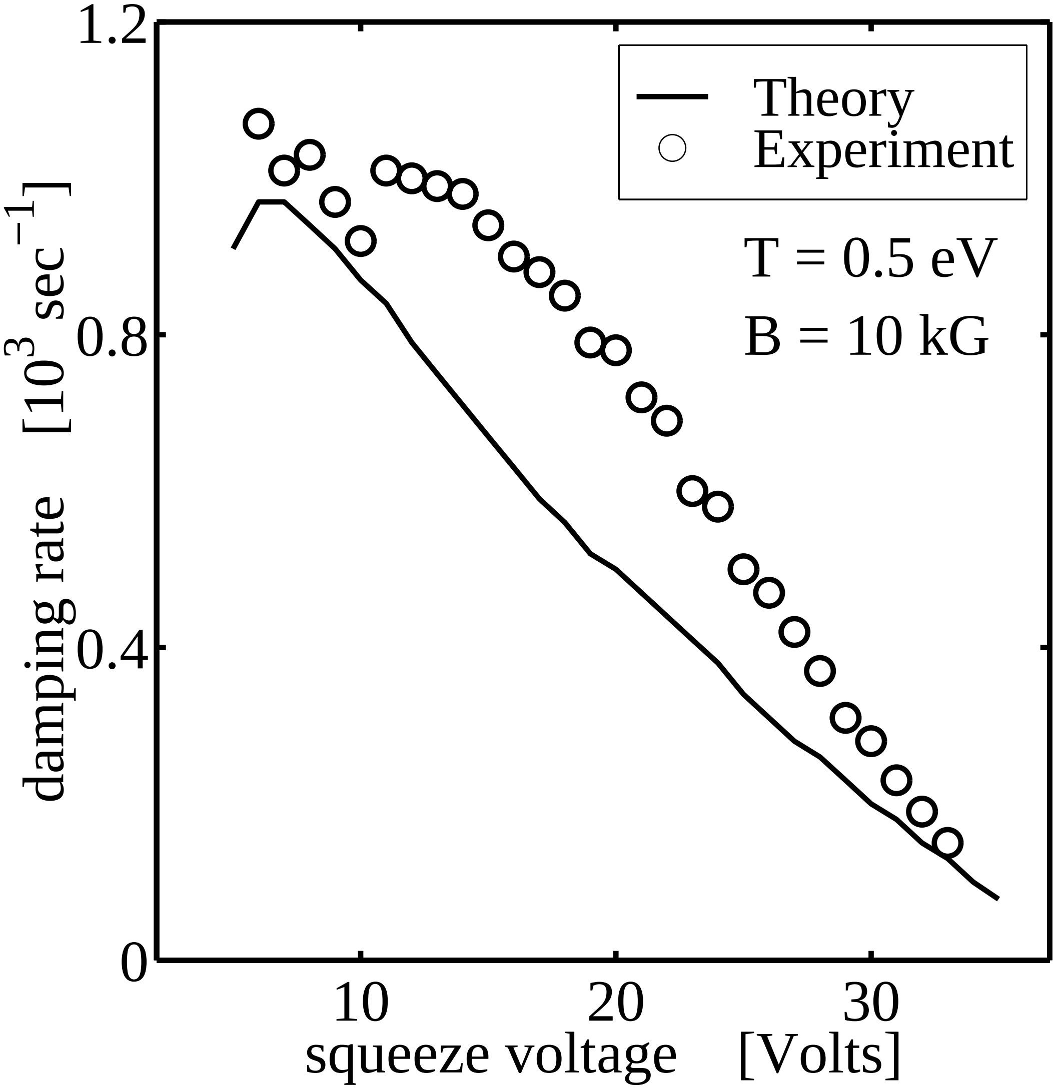

Figure 3.12: Mode damping rate vs. applied squeeze voltage from theory [Eq. (3.44)] and experiments.

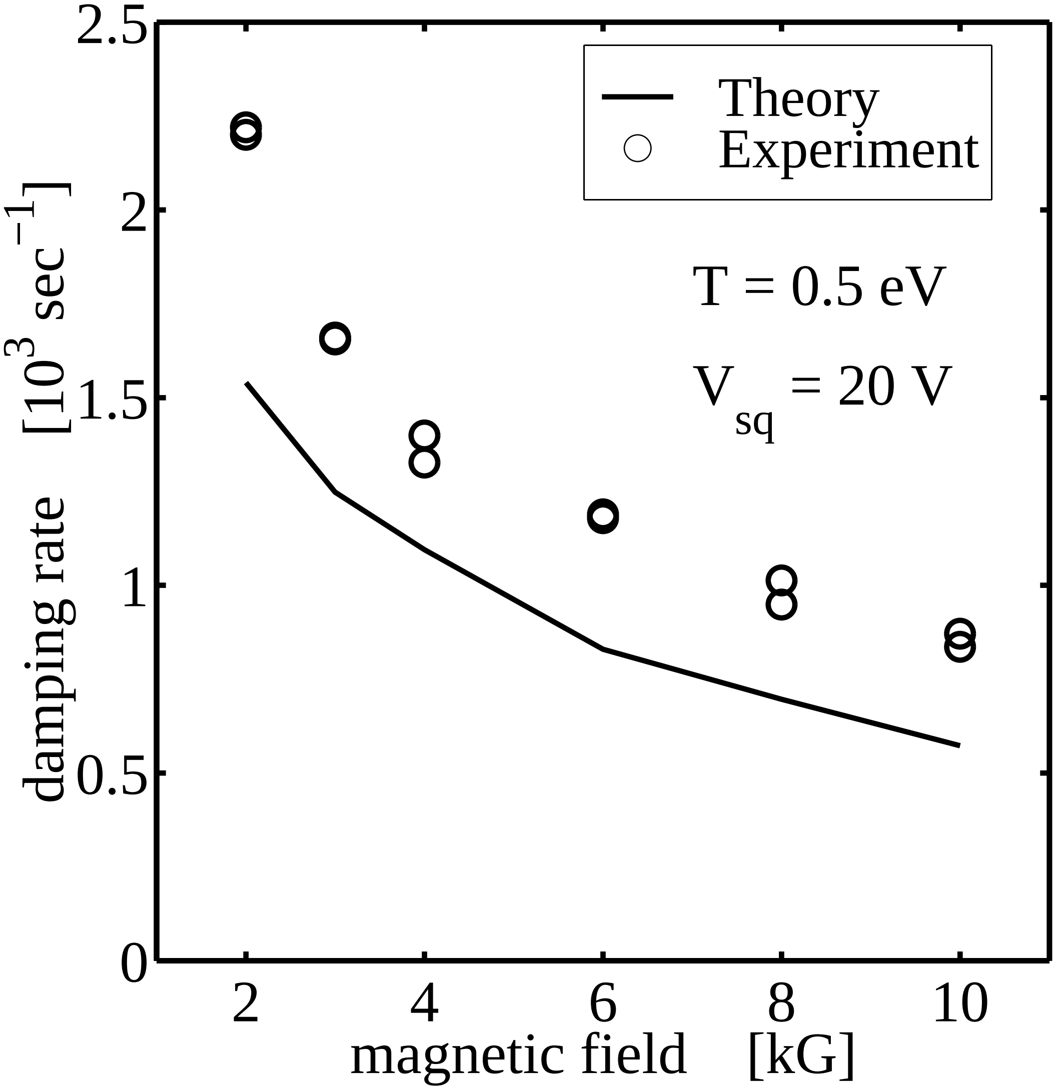

Figure 3.13: Mode damping rate vs. magnetic field. The theory correctly predicts the $B^{-1/2}$ at high magnetic fields. At low field, the fast bounce assumption is violated and the theory breaks down.

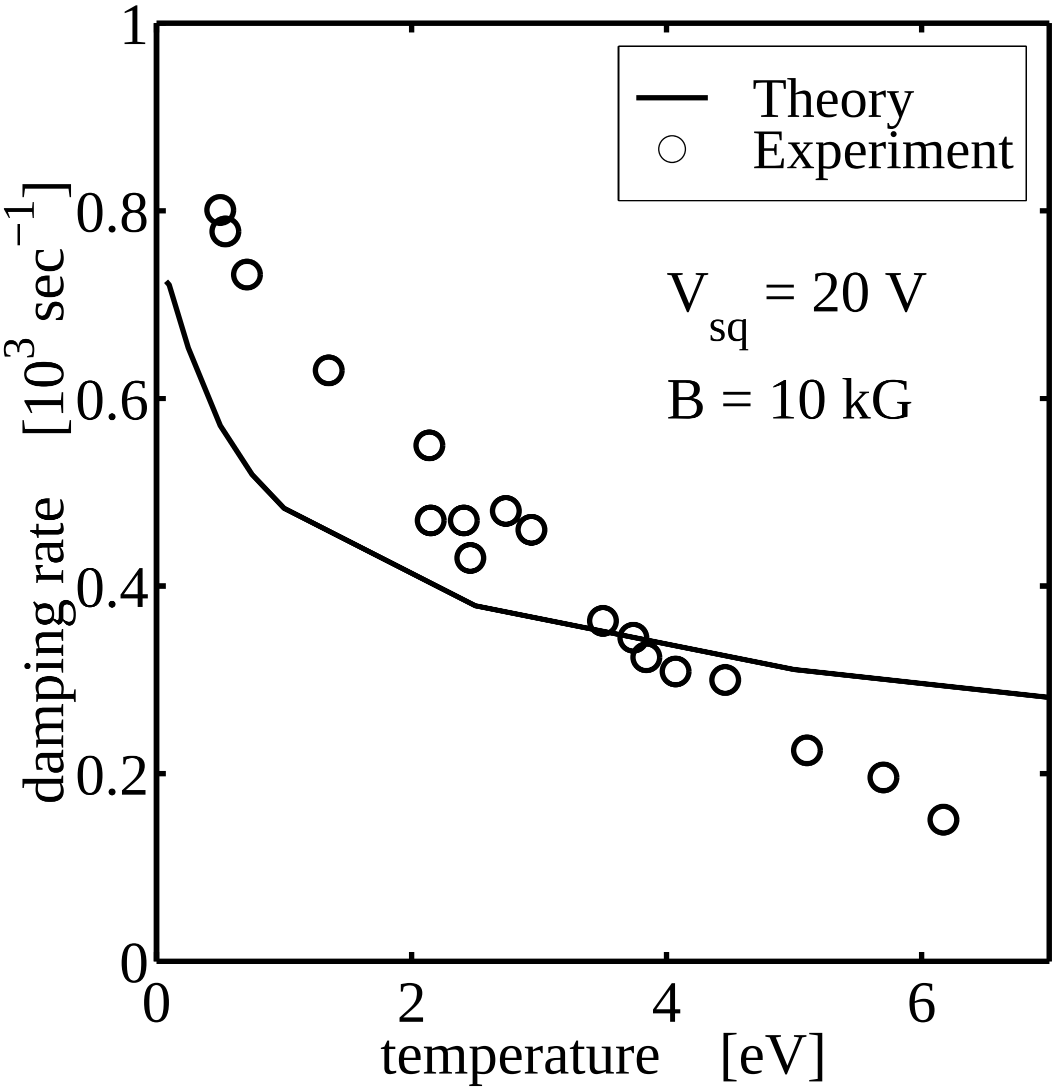

Figure 3.14: Mode damping rate vs. temperature.

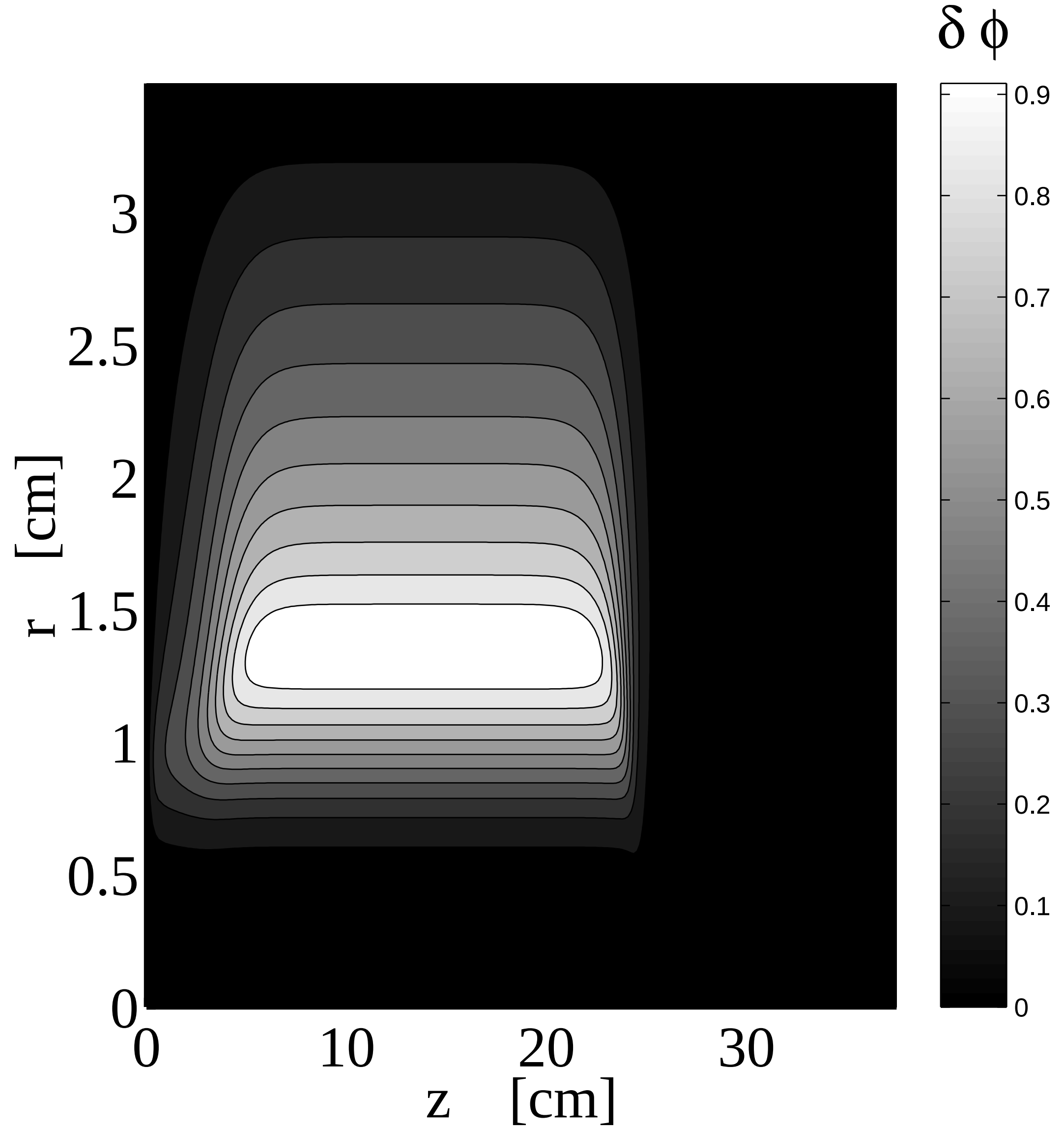

Figure 3.15: Contour plot of mode potential showing axial dependence in the squeeze region and near column end.

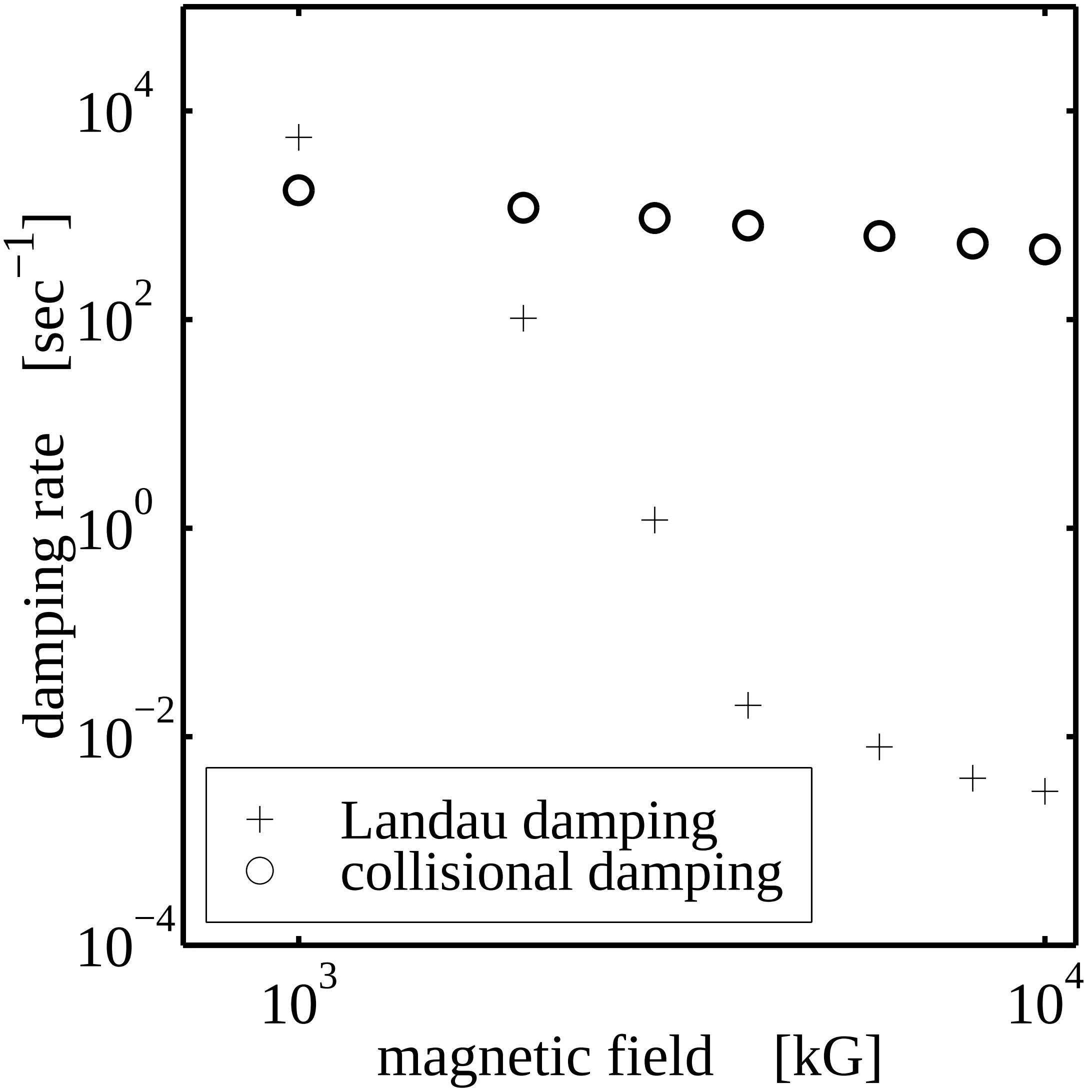

Figure 3.16: Mode damping rate due to Landau resonance and collisions versus magnetic field.

References

[1] R. J. Briggs, J. D. Daugherty, and R. H. Levy. *Phys. Fluids*, 13:421, 1970.

[2] K. M. Case. *Phys. Fluids*, 3:143, 1960.

[3] R. C. Davidson. *Theory of Nonneutral Plasmas.* Benjamin, Reading, MA, 1974.

[4] R. C. Davidson. *Physics of Nonneutral Plasmas.* Addison-Wesley, Redwood City, CA, 1990.

[5] C. F. Driscoll. *Phys. Rev. Lett.*, 64:645, 1990.

[6] D. H. E. Dubin. *Phys. Rev. Lett.*, 66:2076, 1991.

[7] D. H. E. Dubin and T. M. O'Neil. *Rev. Mod. Phys.*, 71:87, 1999.

[8] J. M. Finn, D. del Castillo-Negrete, and D. C. Barnes. *Phys. Plasmas*, 6:3744, 1999.

[9] H. Goldstein. *Classical Mechanics.* Addison-Wesley, Reading, MA, 1980.

[10] R. W. Gould. *J. Appl. Phys.*, 28:599, 1957.

[11] P. Guenard and H. Huber. *Ann. Radioelect.*, 7:252, 1952.

[12] T. J. Hilsabeck and T. M. O'Neil. *Phys. Plasmas*, 8:407, 2001.

[13] X. P. Huang, F. Anderegg, E. M. Hollmann, C. F. Driscoll, and T. M. O'Neil. *Phys. Rev. Lett.*, 78:875, 1997.

[14] J. D. Jackson. *Classical Electrodynamics.* Wiley, New York, 1975.

[15] A. A. Kabantsev. *Bull. Am. Phys. Soc.*, 47:250, 2002.

[16] A. A. Kabantsev. private communication, 2002.

[17] A. A. Kabantsev, C. F. Driscoll, T. J. Hilsabeck, T. M. O'Neil, and J. H. Yu. *Phys. Rev Lett.*, 87:5002, 2001.

[18] A.A. Kabantsev and C.F. Driscoll. End shape effects on the $m_\theta = 1$ docotron instability in hollow electron columns. In J.J. Bollinger, R.L. Spencer, and R.C. Davidson, editors, *Non-Neutral Plasmas III*, pages 208–213, New York, 1999. American Institute of Physics.

[19] W. Kelvin. *Nature*, 23:45, 1880.

[20] L. D. Landau and E. M. Lifshitz. *Fluid Mechanics.* Pergamon Press, Oxford, 1979.

[21] R. H. Levy. *Phys. Fluids*, 8:1288, 1965.

[22] R. H. Levy. *Phys. Fluids*, 11:920, 1968.

[23] G. G. MacFarlane and H. G. Hay. *Proc. Phys. Soc. (London)*, B63:409, 1950.

[24] G. W. Mason and R. L. Spencer. *Phys. Plasmas*, 9:3217, 2002.

[25] D. Montgomery, G. Joyce, and L. Turner. *Phys. Fluids*, 17:2201, 1974.

[26] G. A. Navratil, A. K. Sen, and J. Slough. *Phys. Fluids*, 26:1044, 1983.

[27] T. M. O'Neil. *Bull. Am. Phys. Soc.*, 40:1741, 1995.

[28] S. A. Prasad and T. M. O'Neil. *Phys. Fluids*, 22:278, 1979.

[29] J. W. S. Rayleigh. *Proc. London Math Soc.*, 11:57, 1880.

[30] M. Rosenbluth, W. M. MacDonald, and D. L. Judd. *Phys. Rev*, 107:1, 1957.

[31] M. N. Rosenbluth, D. W. Ross, and D. P. Kostomarov. *Nucl. Fusion*, 12:3, 1972.

[32] R. Salmon. *Lectures on Geophysical Fluid Dynamics.* Oxford University Press, New York, 1998.

[33] D. A. Schecter, D.H.E. Dubin, A.C. Cass, C.F. Driscoll, I.M. Lansky, and T.M. O'Neil. Inviscid damping of elliptical perturbations on a 2d vortex. In J.J. Bollinger, R.L. Spencer, and R.C. Davidson, editors, *Non-Neutral Plasmas III*, pages 115–122, New York, 1999. American Institute of Physics.

[34] R. A. Smith. *Phys. Fluids B*, 4:287, 1992.

[35] R. A. Smith and M. N. Rosenbluth. *Phys. Rev. Lett.*, 64:649, 1990.

[36] W. M. Tang. *Nucl. Fusion*, 18:1089, 1978.

[37] H. F. Webster. *J. Appl. Phys.*, 26:1386, 1955.